CHARACTERIZING INTRASEASONAL TRANSITIONS OF THE WINTERTIME

PACIFIC JET STREAM

By

Maria M. Madsen

A dissertation submitted in partial fulfillment of

the requirements for the degree of

Doctor of Philosophy

(Atmospheric and Oceanic Sciences)

at the

UNIVERSITY OF WISCONSIN – MADISON

2021

Acknowledgments

My path through graduate school was not how I imagined it would be. I pictured a straightforward route, a project with distinct boundaries, few obstacles, and a quick four-year path from entering graduate school to graduating with a PhD. Somehow, I was wrong on all counts. Despite the difficulties I encountered along the way, I still found myself continually thankful for the opportunity to pursue my passion and curiosities. Ultimately, I would not have accomplished this goal without my advisor, the AOS staff, students, and faculty, and my friends and family.

First, I'd like to thank my advisor, Jonathan Martin. He has been exceptionally supportive throughout my graduate career, providing me with the needed space to develop my research ideas and the guidance to carry them out. His continuous support helped me through multiple obstacles throughout graduate school. He has also been a role model for teaching and outreach. His passion and excitement for science is contagious, and being a TA for him over the years has helped me grow into a better teacher and communicator.

I also want to thank the other members of my PhD committee (Professors Michael Morgan, Stephanie Henderson, Christian Grams, and Daniel Vimont), all of whom provided valuable input and challenged me to think more critically about my research. Michael may have made me second-guess the spelling of every word in a PowerPoint introductory slide, but he was also an invaluable mentor throughout my graduate career. Additionally, Stephanie helped me both during weekly group meetings and beyond them. She always made time to help when I reached out and has been another strong scientific role model for me. Thank you to Christian for the collaborative opportunities and the countless zoom meetings discussing research. I look forward to working with

you in the future. Thank you to Dan for helping me with the statistical aspects of my work and giving me constructive feedback.

Also within the AOS community, I'd like to thank Pete Pokrandt. You have been a tremendous help during both my undergraduate and graduate studies. From simple programming issues to pandemic online teaching mishaps, you've always been there to save the day. Thank you to the rest of the AOS academic staff, past and present. This includes Sonja Johnson, Kathy Kruger, Debbie Weber, Chelsea Dahmen, Christi Levenson, Dee VanRuyven, and Sue Foldy. Thank you for helping me with travel, payroll, TA resources, paperwork, and so much more.

I'd also like to thank my AOS graduate student colleagues, including those I've worked with and those who have become close friends. There are so many of you that have had an impact on me. To my initial lab group members - Zak Handlos, Kyle Griffin, Melissa Breeden, Jessica Taheri, Simran Raju, and Conner Dacey – thank you for being such a supportive, fun, and stimulating research group. Thank you to the later lab group members Kate Abbott, Patrick Beaty, Poush Ghosh, and Ian Beckley as well. I know it was not easy moving to virtual lab group meetings during the pandemic, but I still looked forward to those interactions. Thank you to the AOS graduate students from other lab groups as well, including, but not limited to, Alex Goldstein, Luke Gloege, Juliet Pilewskie, Bailey Murphy, Zoë Brooke Zibton, Karimar Ledesma-Maldonado, Nuo Chen, Claire Pettersen, and Alexa Ross. I also want to say a special thanks to my fellow left-handed, middle child, LIM loving, margarita enthusiast, ASMR watching, dear friend Melissa Breeden. Thank you for your guidance throughout the years. You push me to become a better scientist.

Now onto my friends outside of AOS- there are so many of you to thank, and I feel so lucky to have such amazing, talented, funny, and supportive friends in my life. To Makenzi, Lizzy, Elaine, Osha, Lorna, Brian, Keegan, Sam, Jory, Dylan, Kristopher, Julia, and so many others - I have deeply cherished our pre-pandemic weekly trivia, pizza/pie/surprise parties, dinners, jazz outings, dance nights, low-key hangouts, and our countless bonfire nights. You have kept me going during some of the hardest moments of graduate school, and you have been there to help me celebrate some of the best.

Lastly, I want to thank my family. I have the most loving and supportive parents a person could ask for. They never hovered over me during school, trusting that I was doing my best and encouraging me in whatever goal I set. Thank you, mom and dad, for being my biggest supporters. Also thank you to the rest of my family- Ben, Nik, Emma, Jamey, Auggie, Grandma Maria, Grandpa, Aunt Peg and Uncle Kyle. I have a small family, but what it lacks in numbers it makes up for in utter delight. And to my partner Mike and our dog Odie- your support throughout my graduate school career has been unwavering, from small gestures like putting up with my loud typing as I work through the night, to bigger gestures like helping me through the most difficult times of grad school and supporting my career moves. To all of my family - I've always felt so supported and loved by you, and I can't imagine being where I am without you.

TABLE OF CONTENTS

LIST OF TABLES

LIST OF FIGURES

nodes. Positive (negative) 500 hPa geopotential height (m) anomalies are contoured in red (blue) every 25m starting at 25 (-25).

2.5   As in Fig. 5 but composite positive (negative) SLP anomalies (hPa) in solid (dashed) black lines contoured every 3 hPa starting at 3 hPa (-3 hPa) and 850 hPa temperature anomalies (°K) in red/yellow (blue/purple) contoured every 2 K starting at 2 K (-2 K).

2.6   State of the daily Pacific jet (maroon circles) in the 2D phase space of the leading 250-hPa zonal wind PCs for every day comprising each of the 12 SOM nodes within the 71 cold seasons (1948/49-2018/19). Black circles represent the 2 and 4 contours of magnitude in the EOF/PC phase space.

2.7   Percent frequency of occurrence for each SOM node during each month of the cold season.

2.8   Percent frequency of occurrence for each SOM node during each cold season.

2.9   Decadal mean of frequency of occurrence for each SOM node beginning with 1950.

2.10   Frequency of occurrence of each SOM node for days characterized by PNA events (a), AO events (b), and ENSO events (c).

2.11   Lagged relationships between the eight phases of the MJO and SOM nodes during ENSO neutral events. For each active MJO phase, (RMM >1), the anomalous FOC of SOM nodes is plotted as a function of lag from 1 to 16 days after the active MJO phase. A 100% anomalous FOC denotes a FOC twice that of the climatological FOC for the SOM node, whereas a -100% anomalous occurrence denotes a FOC of 0. Orange (green) shading denote statistically significant anomalous FOC as determined from a $\chi 2$ test and binomial test.

2.12   As in Fig. 2.11 but during positive ENSO events.

2.13   As in Fig. 2.11 but during negative ENSO events.

3.1   5-20-day anomalous transition probabilities for SOM Nodes 1-12 observed in the NCEP Reanalysis data. Within each subplot, columns 1-12 correspond to the SOM Node into which the transition is observed and rows 1-12 correspond to the node at the start of the transition. Red (blue) squares indicate enhanced (reduced) transition frequency at the 95% significance level.

3.2   Schematic of statistically significant preferred transitions identified in the probability tables at lags (a) 5, (b) 10, (c) 15, and (d) 20 (Fig. 3.1). Red boxes indicate a preferred tendency to remain in the initial node, and red arrows point towards a preferred transition from the initial node into the final node at the corresponding lag.

ABSTRACT

The north Pacific jet stream is an especially powerful feature of the Earth's general circulation during the boreal winter. It is characterized by omnipresent meridional fluctuations as it meanders over the north Pacific basin and interacts with a plethora of other atmospheric variables and processes. Consequently, the north Pacific jet stream exerts a substantial influence in the production of day-to-day sensible weather and regional climate. Previous research regarding the intraseasonal variability of the wintertime north Pacific jet has employed empirical orthogonal function (EOF)/principal component (PC) analysis to characterize two leading modes of variability: a zonal extension or retraction and a ~20° meridional shift of the jet exit region. These leading modes are intimately tied to the large-scale structure, sensible weather phenomena, and forecast skill in and around the vast north Pacific basin. Furthermore, rapid transitions from one Pacific jet EOF/PC mode to another are associated with sudden changes in the three-dimensional distribution of anomaly patterns as well as some extreme temperature and precipitation events in Hawaii and North America. Currently, however, transitions between these leading modes are poorly understood.

In this work, a self-organizing maps (SOM) analysis is applied to 71 Northern Hemisphere cold seasons of 250 hPa zonal winds from the NCEP/NCAR reanalysis data to identify 12 characteristic physical jet states and to explore the nature of intraseasonal transitions among such states of the north Pacific jet. Transition probability tables are calculated on timescales ranging from 5 days to three weeks to identify common and uncommon transitions among the 12 SOM jet states. Additionally, a Linear Inverse Model (LIM) is employed to assess the predictability of the SOM-identified common transitions. These analyses reveal that distinct, intraseasonal preferred

transitions of the Pacific jet are identifiable at a variety of timescales and that the hitherto more common EOF/PC analysis of jet variability obscures important subtleties of jet structure. These subtleties, revealed by the SOM analysis, bear on the underlying physical processes that the force transitions as well as the nature of their downstream impacts and predictability.

CHAPTER 1: INTRODUCTION TO THE JET STREAM AND PACIFIC JET VARIABILITY

1.1 Early Jet Stream Investigation

One of the most prevalent, powerful, and intriguing features of the Earth's general circulation are the narrow, high speed wind currents near the tropopause, known as jet streams or jets. These jet streams are characterized by omnipresent meridional fluctuations as they meander around the globe and interact with a plethora of other atmospheric variables and processes. Indeed the waviness of the jets is a first order forcing for the train of cyclones and anticyclones that characterize the flow of the mid-latitudes. Consequently, the jet streams exert a substantial influence in the production of day-to-day sensible weather and regional climate.

Over the past 80 years, observations, theoretical modeling, and statistical analysis have been employed to further understanding of the complex dynamics of the jet stream. The early 20th century was an especially revolutionary period for synoptic meteorology as observational networks expanded, and urgency to understand the dynamics of the atmosphere escalated. The term 'jet stream' may not have been coined until the 1940's by Carl Rossby (Reiter 1963, 1967), but the theoretical framework and observations by which this phenomenon was discovered has a longer pedigree.

Some of the earliest theoretical work contributing to jet stream discovery was developed in the 1870's when William Ferrel described a relationship between a horizontal temperature gradient and the shear of the geostrophic wind, now known as the thermal wind relationship (Kutzbach 1979). In a time that was void of upper-air observations, this relationship was the only way to estimate upper-level winds, requiring only low-level temperature and wind data. This was the most accurate method of estimation until a few decades later when kites and pilot balloons

provided observations of the upper-level winds (Lewis 2003). However, the discovery of a persistent, intense, upper-level westerly wind, or jet stream, was not made until 1926, when a scientist by the name of Wasaburo Ooishi used balloon-obtained upper-level wind observations over two years (1923-1925) to create a seasonal climatology of wind profiles over Tateno, Japan (Lewis 2003). These results, published in Esperanto, depicted a persistent westerly wind that was markedly stronger in the winter (Ooishi 1926, Fig. 1.1). Although now credited as one of the first to discover the jet stream, European and American researchers largely ignored Ooishi's findings until bombing raids during World War II in both the European and Pacific theaters motivated better understanding of upper-level winds.

One such motivating World War II mission occurred during a planned 1944 bombing raid on Tokyo (Bryson 1994). Scientists in the 20th Air Force Weather Central were entrusted to forecast winds near 10km for the raid. With only surface data and a sounding of temperature and humidity, they utilized the thermal wind relationship to forecast a westerly wind of 168 knots ($\sim$87.5 ms^{-1}) over Tokyo. The forecast was met with criticism from the general, as it seemed implausible that the winds could reach such high speeds despite Ooishi's earlier findings reporting an average upper-level wind speed of 70 ms^{-1} over Japan. Against the scientists' recommendation, the bombing raid commenced and subsequently failed when east-bound planes grappled with the strong westerly winds. An apologetic general reported back to the scientists a measured wind speed of 170 knots (87.5 ms^{-1}). The failed mission highlighted not only how crucial it was to better understand the jet stream, but also the complete ignorance of Ooishi's earlier findings among the military scientists of the United States.

Shortly after World War II, the U.S. Weather Bureau released two volumes of upper-level charts of the Northern Hemisphere. With this information, staff members of the Department of

Meteorology at the University of Chicago, including Rossby, Charney, Riehl, and Palmén, conducted a synoptic study on the mid-latitude atmospheric general circulation. The synoptic analysis, published in 1947, marked the forward movement of jet stream understanding with the major conclusion: the jet stream is a narrow, meandering, and continuous area of high winds situated within a tropopause break and above an intense baroclinic polar front (University of Chicago 1947).

The golden era of jet stream research that ensued led to major advancements in the understanding of jet stream dynamics. Integral to this understanding was the separation between a subtropical and a polar jet stream. Riehl (1948) and Palmén and Newton (1948) were some of the first to provide evidence for two distinct jet streams over the Northern Hemisphere: one near 45°N above a polar front (the polar jet) and another higher altitude maxima over the subtropics (the subtropical jet). These two species of jet streams are driven by differing underlying dynamics, wherein the subtropical jet results from poleward angular momentum transport by the tropical Hadley cell (Krishnamurti 1961; Held and Hou 1980) and the polar, or eddy-driven, jet stream is generated from baroclinic eddy processes within the mid-latitudes (Held 1975; Rhines 1975; Panetta 1993).

During the Northern Hemisphere (NH) winter, the jet has two regions of maximum intensity- one extending from the east coast of North America into the Atlantic Ocean and another over the North Pacific extending from East Asia into the central Pacific, known as north Pacific jet. Soon after the identification of a separate subtropical jet stream, Mohri (1953) demonstrated that the north Pacific jet had properties of both a polar and subtropical jet, making it a hybrid feature. In fact, a subsequent study by Krishnamurti (1961) investigating the mean axes of the subtropical jet stream revealed that the subtropical and polar jet were nearly out of phase with one

another, flowing side-by-side in proximity over the west Pacific. The out-of-phase axes over the west Pacific creates a conducive environment for interaction between the polar and subtropical jets, especially during the NH winter when there is a strengthening of the meridional temperature gradient and deep tropical convection (Hoskins and Valdes 1990; Eichelberger and Hartman 2007; Handlos and Martin 2016, Christenson et al. 2017). Consequently, considerable attention has focused on the wintertime north Pacific jet and its interactions with extratropical and tropical processes.

1.2 North Pacific Jet Variability

During the NH cold season [November-March (NDJFM)] both the climatological intensity and zonal extent of the north Pacific jet increase, reaching their zeniths in February before weakening and retracting thereafter (Newman and Sardeshmukh 1998). Throughout the same season, the north Pacific jet undergoes significant intraseasonal variability, with large and often rapid variations in both its zonal extent as well as the meridional deflection of its exit region. These modes of variability of the Pacific jet have been the focus of a number of recent studies (e.g. Schubert and Park 1991; Athanasiadis et al 2010; Jaffe et al., 2011; Griffin and Martin, 2017; Breeden and Martin, 2018; Winters et al., 2019a, 2019b). As one of the most important features at the interface between the large-scale general circulation and the life cycle of individual weather systems, there is both theoretical and operational incentive to more comprehensively understand the details of jet variability.

One of the earliest investigations of wintertime Pacific jet variability was undertaken by Schubert and Park (1991), in which they applied empirical orthogonal function (EOF) analysis to low-frequency 200-hPa zonal winds over seven years (1981-87). Their results characterized the leading mode of variability, EOF 1, as a shift in jet core intensity and shape, and the next leading

mode, EOF 2, as a zonal extension/retraction of the jet exit region. They found that these leading modes were also associated with fluctuations in circulation patterns like the Pacific-North American (PNA) Pattern and wave propagation emanating from eastward-moving tropical convection between the Indian Ocean and the west Pacific.

Current understanding of the intraseasonal variability within the wintertime Pacific jet, later refined by Athanasiadis et al. (2010) and Jaffe at al. (2011), is centered on two predominant modes: a zonal extension or retraction of the jet exit region between 160°E to 120°W (EOF 1) and a ~20° meridional shift of its exit region (EOF 2, Fig.1.2). These leading modes are associated with basin-scale anomalies in the Pacific that have substantial impact on the synoptic-scale structure and downstream sensible weather. For example, Chu et al. (1993) demonstrated that the zonal extent of the Pacific jet had a considerable impact on Hawaiian wintertime rainfall. They analyzed two consecutive winters between 1981-1983, illustrating that a zonally retracted jet was associated with a wet Hawaiian winter, whereas an extended jet was associated with an extremely dry winter. Additionally, in constructing a climatology of subtropical (Kona Low) cyclones over Hawaii, Otkin and Martin (2004) found that a retracted Pacific jet is linked to an increased frequency of such storms in the central Pacific. This was later supported by Athanasiadis et al. (2010), who associated the leading EOF with a north-south shifting of the Pacific storm track in addition to the PNA teleconnection pattern (Wallace and Gutzler 1981).

Similarly, Jaffe et al. (2011) examined 19 cold season jet retractions that occurred within 28 years of NCEP/NCAR reanalysis data and found that variability within the Pacific storm track occurs in tandem with retraction events. Composite analysis of the retraction events revealed that prior to the retraction, enhanced storm track density downstream and poleward of the climatological jet exit region prevails (Fig. 1.3). After the retraction events, however, the same

region has suppressed storm track density, while enhanced storm track density appears in the central subtropical Pacific. Retraction events were also associated with a rapid onset of a negative PNA pattern. Over the 10 days surrounding each event, both 500-hPa geopotential height and sea level pressure (SLP) anomalies switched polarity from negative to positive in the north Pacific, exhibited an equivalent barotropic structure with broad areal extent, and had magnitudes in excess of 200m and 20 hPa, respectively. Additionally, the composite 200-250-hPa Ertel PV anomaly field showed rapid deformation during the jet retraction events, suggesting that PV anomalies may play an important role in initiating retraction events.

Breeden and Martin (2018) investigated the initiation of a long-lived Pacific jet retraction from mid-February to early March 2006 that preceded a persistent negative PNA pattern and led to record rainfall, flooding, and mudslides in Hawaii (Jayawardena et al., 2012). Using a quasi-geostrophic piecewise tendency analysis, they found that the retraction event was largely influenced by the deformation of a high-amplitude ridge downstream of an extended jet exit region. Key to the initiation of the retraction event were two anticyclonic anomalies in an area of strong deformation that, through a series of LC1 (Throncroft et al. 1993) wavebreaking events, diverted and retracted the jet. A negative PV anomaly on the cyclonic shear side largely influenced the growth of the ridge downstream of the jet exit region and the subsequent series of LC1 wavebreaking events.

In addition to sensible weather impacts in Hawaii and elsewhere in the Pacific basin, recent studies have demonstrated that intramodal changes of the Pacific jet have impacts over North America. Griffin and Martin (2017) showed that jet extensions and poleward shifts were both associated with enhanced 250-hPa cyclonic circulations in the central north Pacific and 850-hPa low-level warm anomalies over North America. For jet extensions, the warm anomalies were

localized over western North America whereas for poleward shifts, they were localized over north-central North America. Conversely, jet retractions and equatorward shifts led to enhanced 250-hPa anticyclonic circulations in the central north Pacific and low-level cold anomalies over western North America. These results were corroborated by Winters et al. (2019a) who tied extreme temperature events (ETEs) in North America to the four Pacific jet regimes using a north Pacific jet (NPJ) phase diagram constructed from the two leading EOFs of 250-hPa zonal wind. They found that warm ETEs on the U.S. west coast are frequently characterized by an evolving jet extension and equatorward deflection in the 10 days preceding the event. Conversely, cold ETEs on the west coast and warm ETEs on the east coast occur most frequently in the days following jet retractions. This is consistent with studies that show negative PNA patterns are associated with jet retraction events (e.g. Athanasiadis et al. 2010; Jaffe et al, 2011; Breeden and Martin, 2018). Additionally, equatorward shifts of the jet preceded most cold ETEs on the U.S. east coast.

Using the same NPJ phase diagram employed in Winters et al. (2019a), Winters et al. (2019b) showed that the EOF mode and changes within EOF modes of the north Pacific jet have an apparent impact on medium-range forecast skill over North America. The study analyzed 30 years of Global Ensemble Forecast System (GEFS) reforecasts to conclude that the greatest forecast skill occurred in conjunction with an extended or poleward deflected jet whereas the worst skill occurred in conjunction with a retracted or equatorward shifted jet (Fig. 1.4). Additionally, there was reduced forecast skill when forecast periods occurred during a transition between extensions, retractions, and deflections poleward and equatorward.

Despite recent work demonstrating the substantial impact that Pacific jet variability has on the large-scale structure, sensible weather phenomena, and forecast skill in and around the vast north Pacific basin, the *transitions between the leading modes* of such variability are poorly understood.

Better understanding of such transitions promises new insight into aspects of tropical/extratropical interaction and may provide additional guidance in the medium-range forecasting of some extreme events. As a step toward remedying this deficit of understanding, *this work investigates the following research questions:*

    RQ1) *Are there preferred transitions within the wintertime Pacific jet? If so, what are they?*

    RQ2) *What are the characteristic evolution, synoptic-scale structure, and downstream impacts associated with the preferred transitions?*

1.3 Tropical Interactions

In addition to **RQ1** and **RQ2,** consideration of tropical influences on jet stream variability is integral in examining transitions. An earlier study by Hoskins and Karoly (1981) utilized a linearized steady-state baroclinic model to examine the atmospheric response to a subtropical and mid-latitude thermal source. They determined that a subtropical thermal source induced from anomalous convection leads to a wave train from the associated upper-level divergence in the tropics. The long wavelengths propagate poleward and eastward out of the tropics and into the vicinity of the mid-latitude storm track. The resulting Rossby wave source from subtropical and tropical thermal sources induced a teleconnection response pattern like the PNA, which has frequently been associated with the zonal extent and magnitude of the Pacific jet (Wallace and Gutzler 1981; Trenberth et al. 1998).

In addition to Hoskins and Karoly (1981), many studies have demonstrated tropical influences on jet stream variability, including tropical heating anomalies like the El Nino-Southern Oscillation (ENSO) and the Madden Julian Oscillation (MJO). Trenberth et al. (1998) revealed

that SST changes associated with ENSO events shifted the location and intensity of organized tropical convection and that the shift induced anomalous thermal sources through latent heat release and divergence in the upper troposphere. The response, a quasi-stationary Rossby wave train of stream function anomalies propagating poleward and eastward, enhanced the westerlies and resembled the positive PNA-like pattern described in Hoskins and Karoly (1981).

The MJO is another tropical thermal forcing that strongly impacts anomalies in the extratropical circulation. Being the dominant mode of intraseasonal variability in the tropics, the MJO is an important feature to consider when investigating variability at subseasonal timescales and developing mid-range forecasts. The MJO is a tropical convective disturbance, originating in the Indian Ocean, that migrates eastward, in 30-60 day cycles (Madden and Julian 1972). MJO events consist of anomalous convection in one area as well as a companion region of suppressed convection. Anderson and Rosen (1983) demonstrated that variations in atmospheric angular momentum (AAM) are linked to tropical thermal forcings, like the MJO, and propagate poleward whereafter they may impact the Pacific jet. Findings from Shubert and Park (1991) later supported this idea, which revealed substantial asymmetries in composited outgoing longwave radiation (OLR) anomalies following extremes in the leading EOF modes of 200 hPa zonal winds.

More recently, anomalous convection from MJO events has been linked to anomalies in the Pacific jet exit region (Wheeler and Hendon 2004; Moore et al. 2010). Moore et al. (2010) examined the Pacific basin extra-tropical response to MJO events over 24 cold seasons (DJF). Their analysis depicted negative anomalies in 250-hPa winds during earlier phases of the MJO with suppressed convection over the central Pacific (Fig. 1.5a). Conversely, positive anomalies in upper-level winds characterized later phases of the MJO, with enhanced convection over the central tropical Pacific (Fig. 1.5b). The relationship between jet stream anomalies and the MJO

phase corresponded to a Matsuno-Gill response to convection wherein an anticyclonic anomaly develops northwest of the heating maximum, enhancing the meridional temperature and potential vorticity (PV) gradient poleward of the anticyclone (Matsuno 1966; Gill 1980; Moore et al. 2010). Another perspective is that diabatic heating alters the PV gradient through eroding PV above the heating maximum while generating positive (cyclonic) PV below the maximum (eg. Raymond 1992; Stoelinga 1995). Consequently, during an MJO event in which enhanced convection traverses over the central tropical Pacific, there is an outflow of low PV, high θ_e air. This, in turn, erodes PV equatorward of the jet stream, raises the tropopause, and increases the PV gradient.

Overall, the asymmetry in tropical convection between leading modes of Pacific jet variability highlights the importance of considering tropical processes in characterizing Pacific jet transitions. Though prior research demonstrates that the wintertime Pacific jet is modulated by both tropical and extratropical environments, the details of these teleconnections and their impact on transitions within the jet, are still incomplete. Jaffe et al. (2011) found that retraction events coincided with growing, quasi-stationary negative OLR anomalies over Indonesia; however, the physical mechanisms relating the OLR anomalies and retraction events were unclear. One of the difficulties in characterizing the relationship between tropical processes and Pacific jet transitions is the varying temporal and spatial scales at which extratropical and tropical processes interact with one another. *Therefore, another focus of this thesis will be pursuit of the following research question:*

> ***RQ3)*** *How predictable are these transitions? What is the role and relative importance of tropical heating and the extratropical circulation on these transitions? What is the role of the MJO in these evolutions?*

This dissertation work consists of five components. In Chapter 2, the most common jet structures within 71 winter seasons of the NCEP/NCAR Reanalysis data (Kalnay et al., 1996) are identified and characterized with a 12-node self-organizing maps (SOM) analysis. In Chapter 3, transition probabilities amongst the 12 nodes are presented on various timescales ranging from the sub-weekly to the sub-seasonal. Chapter 4 details composites of the basin-wide extratropical and tropical structure and evolution of the most frequent transitions, lending insight into the physical mechanisms driving specific transitions and the sensible weather associated with them. In Chapter 5, a Linear Inverse Model (LIM) is employed to assess the predictability of the common SOM transitions identified in Chapter 2. Additionally, optimal precursors are identified to diagnose conditions that grow towards Pacific jet states specified in the SOM analysis. Lastly, Chapter 6 provides concluding remarks and future work directions.

Figure within chart: Vertikala distribuo de la rapideco de la vento (Sezona mezzo)

Labels on chart: Somero, Printempo, Autuno, Vintro
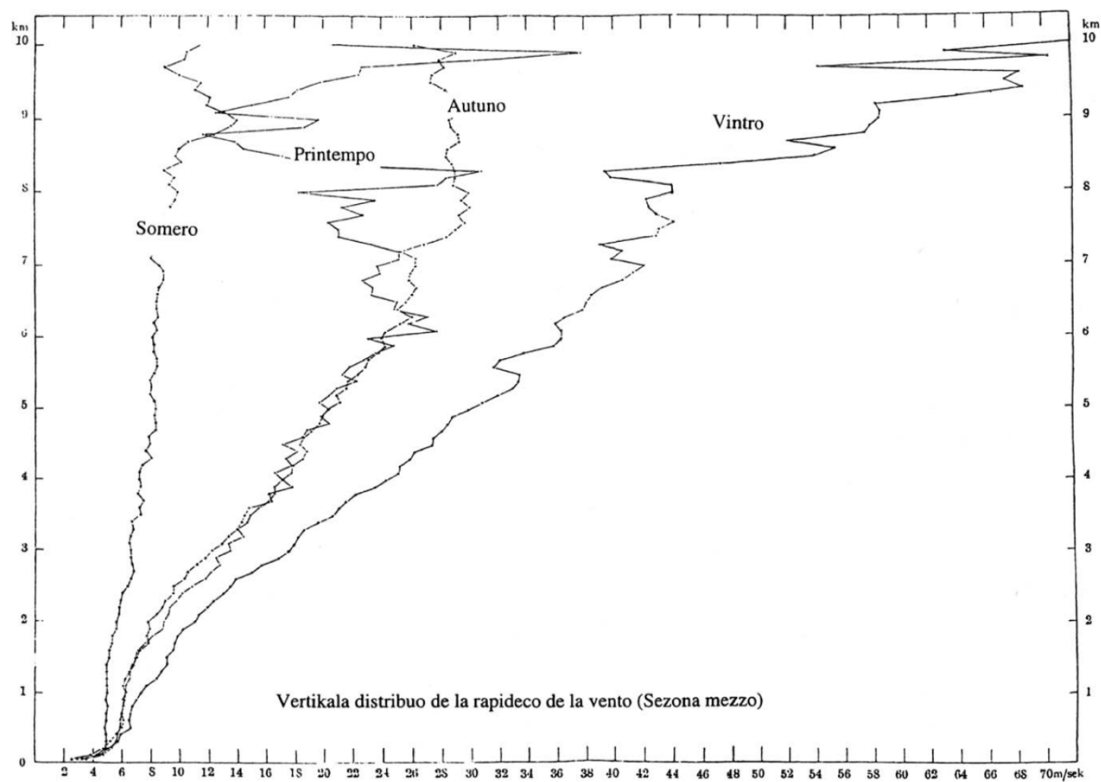
Figure 1.1 Seasonal mean vertical wind profiles from 1924-26 over Tateno, Japan. Data recorded by Wasaburo Ooishi from pilot balloons. X-axis denotes wind speeds (ms^{-1}) and y-axis denotes altitude (km). Vintro, Autuno, Printempo, and Somero, are Esperanto for winter, autumn, spring, and summer, respectively. (From Ooishi, 1926 adapted by Lewis 2003).

a. EOF 1 (Extend/Retract) – 20% Var. Expl.   b. EOF 2 (Shift) – 13% Var Expl.
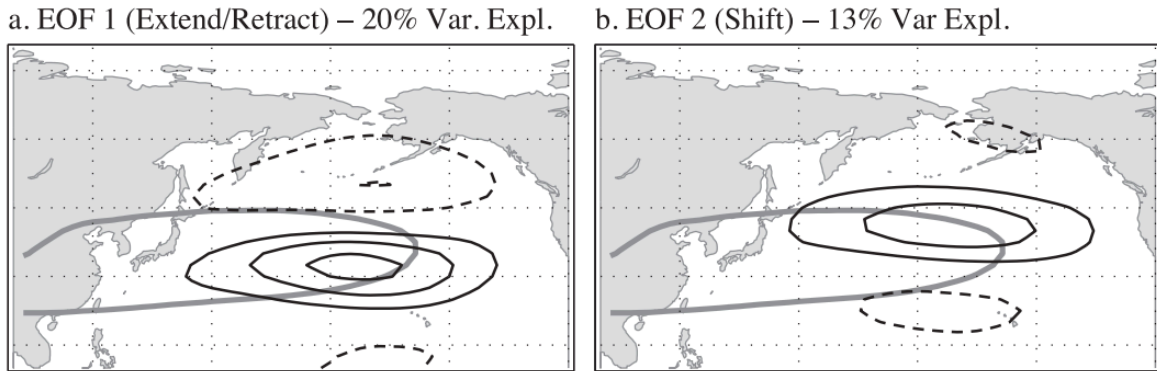
Figure 1.2 From Delcambre et al. 2013a. Leading two EOFs of 300-hPa zonal wind from 20°-80° N regressed onto the zonal wind field from 0°-80° N. Contours are every 4ms^{-1} and zero line removed. Solid (dashed) lines are positive (negative) perturbations and the gray contour is the 20 ms^{-1}isotach of the 300-hPa mean NDJFM zonal wind.
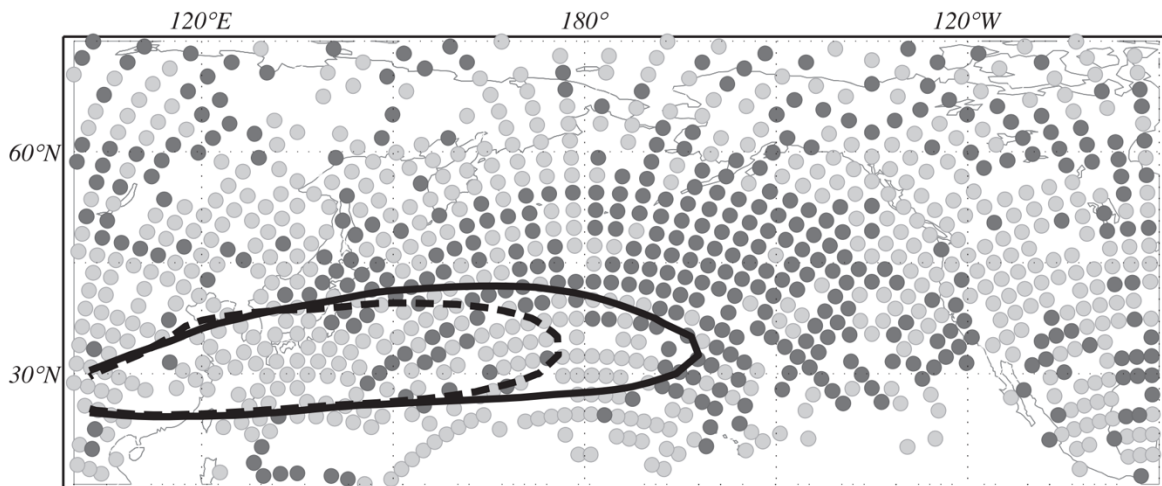
Figure 1.3 (From Jaffe et al., 2011).Differences in storm track density before and after retraction events. Solid (dashed) line denotes 40 ms^{-1} isotach of mean 300-hPa zonal wind of 19 jet retraction events before (after) the retraction. Dark (light) circles represent an increase in storm track density before (after) the retraction.
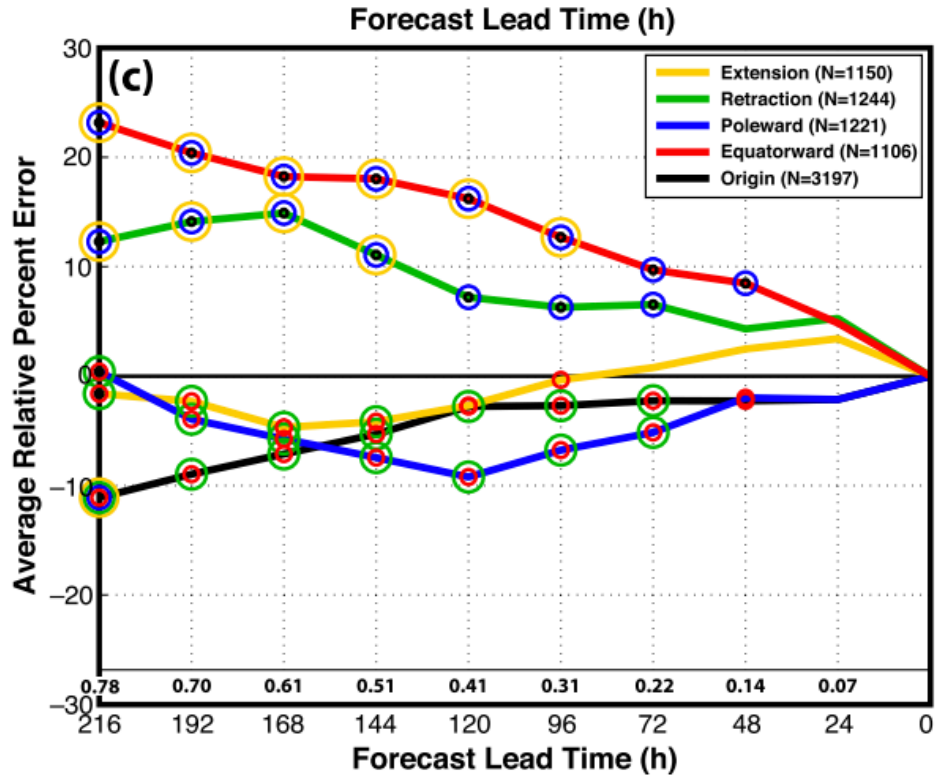
Figure 1.4 From Winters et al. (2019) depicting average percent distance error of mean NPJ phase diagram GEFS ensemble forecasts verified during the same NPJ regime. Errors are calculated relative to the cool season ensemble mean of average distance errors.
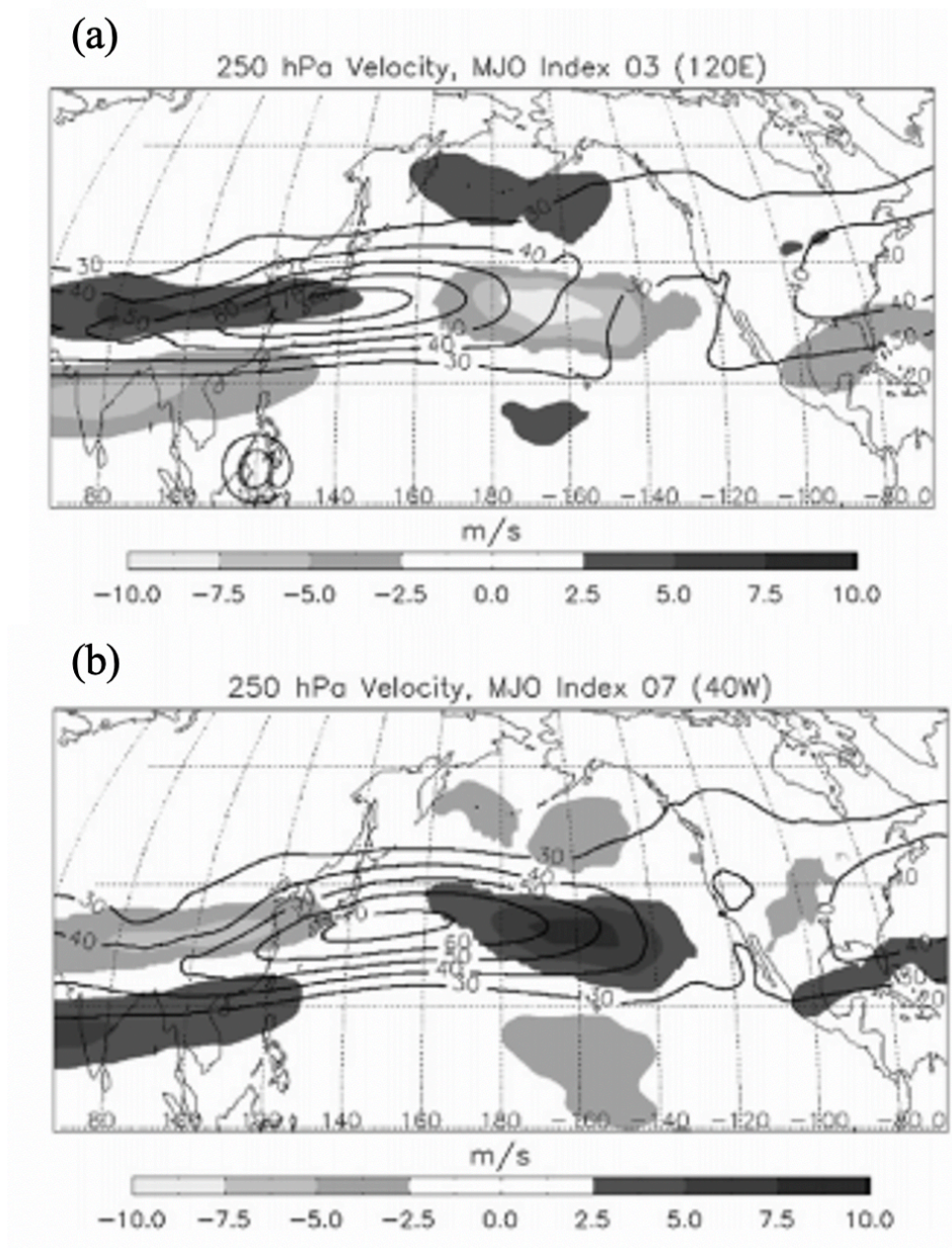
Figure 1.5 Adapted from Moore et al. (2010) depicting 1979-2002 DJF mean 250-hPa wind speed ms^{-1} (black contours every 10 ms^{-1} beginning at 30 ms^{-1}) and anomalies from DJF average (shading) for (c) MJO index 3 and (e) MJO index 7.

CHAPTER 2: SOM-BASED ANALYSIS CHARACTERIZING WINTERTIME NORTH PACIFIC JET VARIABILITY

2.1 EOF Analysis

The use of EOF analysis to decompose and filter spatiotemporal data is a common form of exploratory data analysis that has long been a central part of weather and climate research. EOF/PC analysis identifies a hierarchy of orthogonal spatial patterns most representative of the modes of variability within a state space (the EOFs), as well as a time-series of coefficient values for each EOF that represents the magnitude of the EOF's contribution to the state space through time (the principal components, or PCs) (e.g., Lorenz,1956; Kutzbach, 1967; Cohen, 1983; Smith et al., 1986; Hannachi, 2004; Wilks, 2011). The leading EOFs are the patterns explaining the largest amount of variance of the dataset. Wintertime Pacific jet variability has been traditionally studied with the use of EOF/PC analysis (e.g. Athanasiadis et al., 2010; Jaffe et al., 2011; Griffin and Martin, 2017; Winters et al., 2019a, 2019b). Previous work has identified the leading mode, EOF 1, as an extension/retraction, with anomalies nearly along the climatological jet exit region. The next leading mode, EOF 2, is characterized by anomalies displaced poleward or equatorward of the exit region.

Although previous research on jet variability has relied heavily upon EOF analysis, the leading patterns explain only ~30% of the total variance and, by construction, each mode is linearly independent from the other. Therefore, EOF analysis, while important to developing understanding of Pacific jet variability, provides a rather static view of Pacific jet *transitions*. Transitions within the Pacific jet involve nonlinear processes (e.g. Breeden and Martin, 2019) that are not captured through EOF/PC analysis alone. Identifying commonly observed transitions requires an analysis

technique that objectively identifies the physically observed patterns and captures the nonlinearities of the data. Consequently, this work also employs a self-organizing maps (SOM) analysis. SOM analysis is free from the orthogonality constraint of EOF/PC analysis and incorporates the nonlinear nature of jet stream variability. The inclusion of both linear and nonlinear aspects is a significant advantage of the SOM. This statistical technique has recently been applied to meteorological data sets in both synoptic-climatologies (e.g. Hewitson and Crane 2002; Hope et al. 2006; Lynch et al. 2006; Cassano et al. 2006, 2007; Reusch et al. 2007; Schuenemann et al. 2009; Johnson and Feldstein 2010) as well as examinations of climate model output (e.g. Skific et al, 2009a,b ; Schuenemann and Cassano 2009, 2010). The use of SOMs in this work provides a less subjective, more physical, and versatile visualization tool for characterizing transitions that compliments, rather than replaces, the traditional EOF/PC analysis.

2.2 Self-Organizing Maps

SOMs is a method within the field of artificial neural networks that organizes large, multi-dimensional datasets into finite arrays of recurring *physical* patterns (Kohonen, 2001). This method has been gaining popularity over the last few decades and has been applied to a wide range of atmospheric and oceanic phenomena for feature extraction and classification. For example, Hewitson and Crane (2002) employed SOMs to characterize temporal changes in synoptic scale circulation. Reusch et al. (2007) examined nonlinear aspects of North Atlantic Oscillation (NAO) variability through applying SOMs to mean December-February mean sea level pressure data. More recently, Gervais et al. (2016) used SOMs to characterize future changes in atmospheric variability, and Gu and Gervais (2020) applied SOMs to investigate north Atlantic and north Pacific decadal climate prediction. Unlike EOF/PC analysis and other cluster methods in which the data is assumed to be stationary, SOM treats the data as a continuum.

The SOM is trained through an unsupervised iterative process that begins with a grid of generalized patterns distributed across a user-determined number of nodes (archetypal states) (Kohonen, 2001). The generalized patterns are defined by reference vectors that are linearly initialized using the leading eigenvectors of the 250-hPa zonal wind, where nodes within close spatial proximity are referred to as neighboring nodes. A training period ensues in which the input vectors of daily zonal wind are read into the SOM and matched to the reference vector of greatest similarity (smallest Euclidean distance between the input and reference vector). The reference vector of greatest similarity, also referred to as the best matching unit (BMU), updates to include properties of the newly assigned input vector. A self-learning process continues to update both the nodes with properties of the assigned input vectors as well as reference vectors of neighboring nodes to maximize differences between neighboring nodes. The amount of adjustment within a node is determined by a time-decreasing learning rate, and the adjustment of neighboring nodes is determined through a neighborhood function with a time-decreasing radius.

The SOM in this study utilizes batch training, as it is the most computationally efficient with larger datasets (Kohonen, 1998; Vesanto et al.1999, 2000; Liu et al., 2006). Unlike sequential training, the batch training process does not specify a learning rate function; rather, the weight vector, m_i, adjusts the reference vectors by:

$$m_i(t+1) = \frac{\sum_{j=1}^{M} n_j h_{ij}(t)\overline{x_j}}{\sum_{j=1}^{M} n_j h_{ij}(t)} \tag{2.1}$$

where M is the user-determined number of groups into which the data is partitioned, t is each learning iteration, $\overline{x_j}$ is the mean of the n input vectors within the current group, and h_{ij} is the neighborhood function. An Epanechikov neighborhood ('ep') function is selected for its higher performance in comparison to three other neighborhood functions available in the Matlab SOM toolbox (Vesanto et al., 2000; Liu et al., 2006). The 'ep' function updates neighboring nodes by,

$$h_{ci} = \max(0, 1 - (\sigma_t - d_{ci})^2), \qquad\qquad (2.2)$$

in which a neighborhood radius of influence at time t, σ_t, is specified, and d_{ci} is the distance between SOM nodes c and i. The SOM is run with two sets of trainings of decreasing neighborhood radius. The initial batch training uses a larger neighborhood radius of influence equal to the size of the smaller SOM grid dimension (3). The training iterates for 10 times the length of the input vector and creates a broad pattern distribution. A second training specifies a smaller neighborhood radius of 1 and finetunes the SOM nodes based on the distribution from the resultant initial batch training. The SOM iterates through this process until a mean quantization error is minimized for the entire collection of nodes. The end result is a large SOM array comprised of the updated reference vectors which is then converted into a two-dimensional matrix of maps. The resulting matrix of nodes consists of the most representative physical patterns spanning the continuum of, in this analysis, the zonal 250-hPa winds.

The tunable parameters in the SOM, including grid size, number of iterations, neighborhood radius, and initialization, are selected to achieve a balance of low average quantization error (QE) and topographic error (TE) as well as an evenly distributed Sammon map. The QE quantifies the difference between the node average and the input vectors. Lower QE values indicate a better representation of the BMU to the data. Every SOM node consists of a collection of input vectors with varying QEs as well as a mean QE. Another important map quality measure is TE, which measures the percentage of input vectors that do not have a neighboring second BMU. In a SOM map, the nodes closest to one another are most similar. Therefore, the smaller the TE, the better the SOM map quality. Lastly, a Sammon map illustrates the Euclidian distances between each node in the SOM grid on a two-dimensional distortion plane (Sammon, 1969). A quality SOM map will have a balance of low QE and TE, and a flat, evenly distributed Sammon map.

The present work employs a 3x4 SOM grid consisting of 12 nodes. Smaller grid sizes lead to a blending of relevant patterns whereas larger grid sizes yield patterns not easily distinguishable from one another. Therefore, a 3x4 grid size includes enough interpretable patterns to examine transitions while maintaining low QE and TE errors (Table 2.1) and a well distributed Sammon map (Fig. 2.1). Both the EOF and SOM analyses utilize daily 250-hPa zonal wind data from the NCEP/NCAR Reanalysis (Kalnay et al. 1996), available at a 2.5°x 2.5° horizontal resolution. The zonal wind dataset consists of 71 cold seasons (1948/49-2018/19) in which a cold season is defined as November 1 through March 31 (NDJFM). The spatial domain is 100°E to 120°W and 10° N to 80°N which covers nearly all of the north Pacific basin. Prior to the analyses, the long-term mean and seasonal cycle are removed from the zonal wind anomalies by subtracting a 21-day running mean of the seasonal cycle from the instantaneous 250 hPa zonal wind.

2.3 North Pacific Jet Regimes

2.2.1. Leading modes of variability

The leading modes of wintertime Pacific jet variability obtained from the present analysis are consistent with previous findings (e.g. Athanasiadis et al. 2010; Jaffe et al. 2011; Griffin and Martin 2017; Winters et al. 2019), with EOF 1 (describing 14% of the variance) characterized by anomalies nearly along the climatological cold season jet exit region (Fig. 3a), representing a jet extension in the positive EOF phase (hereafter EOF 1+) or jet retraction in the negative phase (hereafter EOF 1-). EOF 2 (describing 10% of the variance) is characterized by anomalies displaced poleward or equatorward of the exit region (Fig. 2.2), representing a poleward deflection in the positive phase (EOF 2+) or an equatorward deflection in the negative phase (EOF 2-). The leading modes are also statistically well separated, as determined from applying the North et al. (1982) test.

2.2.2. North Pacific Jet SOM nodes

In conducting a SOM analysis of the 250 hPa zonal wind, 12 intraseasonal jet anomaly regimes are depicted in the SOM nodes with a frequency of occurrence (FOC) calculated by the number of cold season days falling within the associated node divided by the total number of cold season days (10,721) (Fig. 2.3). Nodes physically closest to one another in the 3x4 grid depict more similarity (e.g. nodes 4 and 8) whereas nodes furthest apart depict the largest differences (e.g. nodes 1 and 12). Reference numbers are assigned to patterns in which number order is arbitrary and does not indicate similarity. For example, nodes 8 and 12 depict patterns of larger similarity than nodes 6 and 8. Additionally, the calendric listing of days characterizing each node is used to construct composites of the associated circulation patterns and downstream impacts, consisting of 500-hPa geopotential height anomalies (Z500) (Fig. 2.4), sea-level pressure (SLP) anomalies, and 850-hPa temperature (850T) anomalies (Fig. 2.5).

Beginning with the upper left of the SOM grid, node 1 depicts a strong retraction reaching -$20ms^{-1}$ located slightly south of the climatological jet exit region with a positive zonal wind anomaly between 4-$20ms^{-1}$ south of the Aleutian Islands. The zonal wind anomalies are attended by a Z500 anticyclone over the north Pacific and a weaker sprawling cyclonic anomaly between northeast Russia and western Canada (Fig. 2.4). At the surface, a weak positive SLP anomaly is centered near 165°W, with an even weaker negative SLP anomaly over Alaska and Yukon (Fig. 2.5). There are no 850T temperature anomalies associated with node 1, and the FOC is 7.6%.

Below node 1, another retraction is evident in node 5, with strong negative anomalies of -$24ms^{-1}$ in the climatological jet exit region and weaker positive anomalies centered at 50°N and 15°N (Fig. 2.3). This node most closely resembles EOF 1+. The tripole anomaly structure indicates a split-jet feature with midlatitude and subtropical counterparts. The frequency of occurrence for

this pattern is 9.1%, which is the largest of the other SOM nodes depicting jet retractions. The circulation pattern associated with the strong retraction is characterized by a dominant Z500 anticyclonic anomaly centered over the north Pacific basin with two weaker cyclonic anomalies over northeast Russia and western Canada (Fig. 2.4). At the surface, an associated positive SLP anomaly sits over the central north Pacific, with a small tongue of weak warm 850T anomalies stretching from the center of the SLP anomaly to ~200°W (Fig. 2.5).

A stronger retraction is illustrated by node 9, with negative zonal wind anomalies between -$4ms^{-1}$ and -24 ms^{-1} extending further northeast into British Columbia than in nodes 1 and 5 and with a slightly lower FOC of 7.1%. A strip of positive zonal wind anomalies poleward of the climatological jet stretches northeast from east Asia to Alaska, while another strip of positive zonal wind anomalies equatorward of the climatological jet extends from 150°E into the California coast (Fig. 2.3). As in node 5, the tripole anomaly structure implies a split-jet feature; however, the equatorward counterpart extends much further east than in node 5. Circulation composites reveal a SW-NE-tilted positive Z500 and SLP anomaly south of the Aleutian Islands with an equivalent barotropic structure (Fig. 2.4 & 2.5). A weaker cyclonic anomaly sits downstream off the Pacific Northwest coast, disconnected from a smaller cyclonic anomaly south of the anticyclone (Fig. 2.4). A third weak cyclonic anomaly is evident over northeastern Russia. A localized area of cool 850T anomalies is evident over western Canada, whereas a larger tongue of warm 850T anomalies stretches from the coast of Japan to south of the Aleutian Islands (Fig. 2.5).

Resembling the positive phase of EOF 1 is node 8, with strong positive zonal wind anomalies from the climatological jet exit region to 225°E, weaker negative zonal wind anomalies poleward of the climatological jet, and a small area of weaker negative anomalies near 15°N (Fig. 2.3). The FOC of this jet extension is 9.1% which is the same as the jet retraction depicted by node 5.

Associated with the jet extension is a strong surface (Fig. 2.5) and Z500 cyclonic anomaly on the cyclonic shear side of the jet, a weaker positive Z500 anomaly over northwestern North America, and another weak Z500 cyclonic anomaly over eastern North America (Fig. 2.4). The Z500 circulation pattern resembles a positive PNA teleconnection pattern, with the warm 850T temperature anomalies over Alaska and northeastern Canada consistent with positive PNA low-level temperature anomalies (Fig. 2.5).

Node 4, on the other hand, illustrates an extension further poleward and eastward, with strong positive zonal wind anomalies 5-10° poleward than those characterizing node 8 (Fig. 2.3). Similarly, negative zonal wind anomalies lie poleward and equatorward of the climatological jet (Fig. 2.3). Associated with the extension is a cyclonic Z500 and SLP anomaly centered south of Alaska (Figs. 2.4 & 2.5). Two weaker areas of positive Z500 anomalies are located south and east of the cyclonic anomaly (Fig. 2.4). Near the surface, warmer than normal 850T temperatures are evident over central Canada (Fig. 2.5). The FOC of node 4 is the third largest of the SOM nodes at 9.8%.

Another jet extension is evident in SOM node 12, with strong positive zonal wind anomalies in excess of 24 ms^{-1} near 30°N, flanked on the poleward side by an expansive negative zonal wind anomaly (Fig. 2.3). This extended pattern has the lowest FOC compared to the other extended nodes (4 and 8), with a FOC of 6.6%. The circulation pattern associated with node 12 resembles that of node 8, but with stronger cyclonic anomalies over the north Pacific and eastern North America displaced 5° equatorward and 5° poleward, respectively (Figs. 2.4 and 2.5). Near the surface, 850T anomalies differ more substantially than those characterized by node 8, with cold anomalies over northeast North America and on the western flank of the cyclonic SLP anomaly (Fig 2.5).

Along the top edge of the SOM grid are variations of poleward deflections, with node 2 having the lowest FOC of 7.5% (Fig. 2.3). In this node, a weak $4ms^{-1}$ positive zonal wind anomaly stretches along the poleward edge of the climatological jet stream, whereas a stronger area of positive zonal wind anomalies extends northeast into British Columbia from the climatological left jet exit region (Fig. 2.3). Negative zonal wind anomalies of similar magnitude lie south of the positive anomalies. The mid-level circulation associated with node 2 depicts a weak Z500 anomaly couplet over the North Pacific, with a weaker cyclonic anomaly on the cyclonic shear side of the jet and a stronger anticyclonic anomaly on the anticyclonic shear side (Fig. 2.4). At the surface, a weaker positive SLP anomaly is evident below the upper-level anticyclone, whereas a weaker negative SLP anomaly is located downstream of the upper-level cyclone (Fig. 2.5).

The poleward deflection depicted by node 3, on the other hand, is characterized by a maximum positive zonal wind anomaly in the climatological left jet exit region that extends northeast and most closely resembles the positive phase of EOF 2 (Fig. 2.3). Weaker negative zonal wind anomalies are located over the Bering Sea and the subtropical eastern Pacific. The FOC is 7.5%, which is slightly larger than the FOC of node 2. The associated circulation pattern is characterized by a stronger Z500 cyclonic anomaly centered over the Aleutian Islands and a weaker Z500 anticyclonic anomaly on its southeastern flank (Fig. 2.4). Both Z500 anomalies over the Pacific basin have weaker associated SLP anomalies (Fig. 2.5). No 850T anomalies are evident in the composite of node 3 days.

Equatorward deflections are evident in nodes 10 and 11, with node 10 representing 7.3% of the cold season days (Fig. 2.3). In node 10, a bowed band of zonal wind anomalies between 4 and 8 ms^{-1} extends into the California coast, while a stronger area of negative zonal wind anomalies concentrates over the climatological jet exit region, extending NE into British Columbia (Fig. 2.3).

Another weak positive zonal wind anomaly is situated over the Bering Sea. As in nodes 5 and 9, the tripole anomaly structure implies a split-jet feature; however, the poleward midlatitude counterpart is much weaker than in the other nodes. Circulation composites reveal a positive isotropic Z500 anomaly and a σ-shaped SLP anomaly over the Aleutian Islands with an equivalent barotropic structure (Fig. 2.4 & 2.5). A weaker elongated Z500 cyclonic anomaly stretches from the dateline to central Canada (Fig. 2.4). An area of cool 850T anomalies is evident over the western Canada, whereas warm 850T anomalies sit over far northeastern Russia to the Aleutian Islands (Fig. 2.5).

The zonal wind anomalies characterizing node 11 have stronger positive anomalies along the equatorward side of the climatological jet than in node 10 and a lower FOC of 6.8% (Fig. 2.3). An area of negative zonal wind anomalies sits poleward of the climatological jet, and a weaker area of positive zonal wind anomalies is evident near 75°N. Below the zonal wind anomalies, there is a dipole structure in the SLP and Z500 anomalies over the North Pacific, with a weaker cyclonic Z500 anomaly over Canada (Fig. 2.4 & 2.5). Node 11 is also characterized by the largest areas of 850T anomalies, with warm anomalies over northeast Russia and cold anomalies stretching across most of Canada (Fig. 2.5).

Apart from the nodes resembling variations of the leading EOF patterns, node 6 depicts the weakest anomalies, with a 4-8ms^{-1} negative anomaly east of the climatological jet exit region and small areas of 4ms^{-1} positive anomalies centered over the Gulf of Alaska, south of Hawaii, and over the Sea of Japan (Fig. 2.3). The mid- and lower-level circulation depicts a weak anticyclonic anomaly south of Alaska and no associated 850T anomalies (Figs. 2.4 & 2.5). Node 6 is also characterized by the second largest FOC at 10%. The highest FOC in the SOM grid is illustrated by node 7, with positive anomalies centered in the eastern half of the climatological jet indicating

an enhancement of the jet exit region (2.3). Weaker and smaller $4ms^{-1}$ isotachs are evident over the Aleutian Islands and off the California coast. In the mid-levels, there is a negative Z500 anomaly on the cyclonic shear side of the jet and a positive Z500 anomaly downstream off the coast of British Columbia (Fig. 2.4). At or near the surface, weak SLP anomalies are evident over the Pacific basin, with no cold 850T anomalies (Fig. 2.5).

While there are distinct differences in zonal wind, Z500, SLP, and 850T anomalies between SOM nodes, there are also variations in average QE and node residence time (Table 2.2). The QE for each SOM node provides a measure of error between the days characterizing the node and the anomaly pattern depicted in Fig. 2.3. Therefore, a smaller mean QE indicates a pattern better representative of the days characterizing the respective node. Larger QE values characterize nodes featuring equatorward deflections or jet retractions, with mean QE values of 399, 387, 385, and 381 for nodes 9, 10, 11, and 5 respectively. The lowest QE values are associated with poleward deflected nodes 2 and 3, with errors of 361 and 356, respectively. The remaining 6 nodes all have a QE near the grid mean QE of 373.

Mean residence times reflect the transient nature of the jet stream, with a range between 2.2 days (nodes 3 and 6) to 4 days (node 12). However, the maximum number of consecutive days residing in a particular node ranges between 10 days (nodes 3 and 7) to 44 days (node 12). The stark difference between mean residence and max residence times highlights the complex nature of jet stream variability in that while short fluctuations of the jet stream are common, the jet can also exhibit a weekly to monthly persistence. The substantially larger mean residence time and persistence exhibited by node 12 suggests that it might be strongly associated with other persistent teleconnection patterns, some of which are described in subsequent sections.

To further illustrate the relationship between the two leading EOF/PC patterns of the north Pacific jet and the SOM patterns, days with a QE at or below the mean QE of the entire SOM grid are projected onto an EOF/PC two-dimensional phase space in Fig. 2.6. Following the NPJ phase space developed in Winters et al. (2019b), the leading two PCs serve as the axes of the phase space wherein the *x*-axis is defined by PC1 (jet extension/jet retraction), and the y-axis is defined by PC2 (poleward/equatorward deflection). Prior to regressing days onto the phase space, the leading PCs for each day are normalized to unit variance.

For most of the SOM nodes, there is a clear clustering in a specific quadrant of the phase space; however, some of the nodes have a larger scatter into two or more PC quadrants. Nodes 4, 8, and 12 cluster on the right half of the phase space, with node 12 clustering slightly below the positive x-axis (equatorward deflected jet extension), node 8 clustering nearly along the positive x-axis (jet extension), and node 4 clustering above the positive x-axis (poleward deflected jet extension). Conversely, nodes 1, 5, and 9 scatter along the left half of the phase space, with node 5 clustering nearly along the negative x-axis (retraction), node 1 scattered above the negative x-axis (retraction and poleward deflection), and node 9 scattered below the negative x-axis (retraction and equatorward deflection). The projection of days characterized by SOM node 10 averages marginally to the left of the negative y-axis, denoting an equatorward deflection with a minimal retraction, whereas node 11 clusters within the bottom right of the phase space, denoting a slightly extended and equatorward deflected jet regime. The poleward deflections denoted by nodes 2 and 3, however, scatter along the top half of the phase space. Similarly to the equatorward deflected nodes, neither nodes 2 or 3 cluster along the positive y-axis; rather, node 2 clusters to the left of the positive y-axis whereas node 3 clusters to the right of the y-axis. Lastly, nodes 6 and 7 depict the weakest anomalies and are represented as a weak jet retraction and a weak jet extension in the

mean of the phase space, respectively. Overall, the two-dimensional phase space illustrates that some of the patterns comprising the 12-node SOM grid resemble the leading EOF patterns or combinations of the two leading EOFs. However, despite consistencies between the leading EOF/PC modes of Pacific jet variability and many of the SOM nodes, the scatter evident in the phase space suggests that subtleties of Pacific jet variability are far better represented by the SOM than by the traditional EOF/PC phase space.

2.2.3. Variability of SOM node FOC

To gain a better understanding of the intraseasonal, interannual, and interdecadal variability of the 12 SOM nodes, cumulative frequency diagrams are generated for each of the five months within the cold season (November-March), each of the 71 cold seasons (1948/59-2018/19), and each decade beginning with 1950. For the seasonal variability, an average monthly FOC is given by first summing the total the number of days characterized by a particular node for each month and then dividing by the total number of timeseries days characterized by each month (e.g., for the month of November, 30 days x 71 years = 2130 days). A similar procedure follows for calculating FOC over 71 cold seasons, instead summing the number of days characterized by a particular SOM node for each cold season and dividing by the number of cold season days (151 days). For interdecadal FOC, the annual FOC is averaged over six 10-year periods beginning with 1950-1960 and one 8-year period beginning with 2010.

The monthly distribution of the 12 SOM nodes illustrates only slight variability between months, as a 21-day smoothed seasonal cycle is removed from the data prior to the SOM analysis (Fig. 2.7). In November, nodes 3, 4, 6 and 10 reach their maximum in FOC, while nodes 1, 2, and 12 occur less frequently compared to the other cold season months. The jet extension depicted by node 12, in particular, has a much lower FOC compared to other nodes (2.2%). From December

into February, the FOC of node 12 increases, reaching its maximum of 10.8% in February. This is also when node 10, an equatorward deflection, reaches a minimum in FOC. Retracted nodes denoted by nodes 5 and 9 have the lowest FOC in January. By March, however, the FOC of retractions increases, with nodes 1 and 5 having a maximum in FOC of 8.8% and 12.5%, respectively.

Examination of FOC of the 12 SOM nodes over each cold season from 1948/49-2018/19 reveals substantial interannual variability, with abrupt year-to-year changes within many of the nodes (Fig. 2.8). One way to compare the interannual variability between nodes is to calculate the variance within each timeseries. Node 3 has the smallest variance (18.9), followed by node 6 (19.5). Regimes with larger variances are nodes 2 (35.0) and 12 (68.2). Along with having a considerably larger variance than the other 12 nodes, node 12 also features the largest peak in the timeseries- an annual cold season frequency of 43% in 1982-83. The 1982-83 cold season was also characterized by one of the strongest El Niño events on record. This is unsurprising, as prior work has shown that the increased sea surface temperatures over the central and eastern Pacific, in tandem with anomalous convection associated with an El Niño, provide a favorable environment for jet extensions (e.g. Horel and Wallace 1981; Yang et al. 2002; Li and Wettstein 2012; Cook et al. 2017). The strong El Niño cold seasons from 1957-58 and 1997-98 are also characterized by peaks in node 12 FOC, with a frequency of 17% and 30%, respectively. In fact, there is a 0.58 correlation between the timeseries of node 12 FOC and the timeseries of the seasonal mean Niño-3.4 index (ESRL), which is the highest correlation coefficient of all 12 nodes. Comparison of other extended nodes (4 and 8) to the interannual variability in node 12 reveals that there is low correlation between them. Although there are some years in which peaks in node 12 are collocated with peaks in nodes 4 and/or 8 (e.g. 1996, 2002, 2009), it is weakly correlated to the other

timeseries. Similar relationships are illustrated between retractions (1,5,9) and poleward deflections (9, 10, 11). However, the correlation between the FOC of equatorward deflected nodes 2 and 3 is 0.61, exceeding the correlation between any other node which all fell below 0.40. Lastly, a linear regression performed on each of the 12 timeseries revealed no statistically significant trend in FOC over time.

A look at decadal variability of the SOM grid distribution also reveals the absence of a significant trend in FOC (Fig. 2.9). However, some nodes exhibit stronger decadal variability than others. For example, extended node 12 increased in FOC between 1950 to 1990, beginning with a FOC of 2.4% in the 1950s and reaching a maximum FOC of 10.9% in the 1990s, before decreasing again. The decade between 1980 and 1990 was characterized by a larger frequency of jet extensions overall (nodes 4, 8, and 12). The maximum in the extended nodes is supplemented by lower frequencies of retracted nodes 5 and 9. Most of the nodes, however, exhibit a seesawing of mild FOC fluctuations over the 7 decades.

2.2.4. SOM Node Teleconnections

As demonstrated in previous studies, large-scale atmospheric teleconnection patterns are related to fluctuations within the north Pacific jet, and thus, are likely tied to the intraseasonal and interannual frequency distributions of the 12 SOM nodes (e.g. Wallace and Gutzler 1981; Horel and Wallace 1981; Higgins et al. 2000; Athanasiadis et al. 2010; Franzke et al. 2011; Winters et al. 2019). The relationship between atmospheric teleconnections and the north Pacific jet is investigated through considering SOM node frequency changes during Pacific-North American (PNA) events, Arctic Oscillation (AO) events, and ENSO events.

The PNA is a dominant, wavelike anomaly teleconnection pattern in the Northern Hemisphere boreal winter that drives temperature and precipitation anomalies in North America and is

associated with fluctuations within the North Pacific jet (e.g. Dickson and Namias 1976; Barnston and Livezey 1987; Franzke et al. 2011; Griffin and Martin 2017; Henderson et al. 2020). In its positive phase, anomalous troughs sit over the north Pacific and southeastern United States, and anomalous ridges are located over the subtropical north Pacific and the intermountain west of North America. The juxtaposition of the anomalous trough and ridge over the north Pacific supports enhanced westerly flow between them and, subsequently, an enhanced and extended north Pacific jet. Therefore, it would be expected that nodes characterized by jet extensions, namely, 4, 8, and 12, would have a significantly larger FOC during positive PNA events. The negative phase of the PNA, on the other hand, is characterized by anomalous ridges over the north Pacific and eastern US and an anomalous trough over the western US. The anomalous ridge over the north Pacific, often associated with blocking activity, would support enhanced easterly flow within the vicinity of the Pacific jet exit region, leading to a jet retraction or equatorward deflection. Consequently, it would be expected that frequencies for nodes 5, 9, and 10 increase during negative PNA events.

Daily PNA index values (CPC 2017b) are utilized to separate SOM FOC into three categories: positive PNA events with an index above 1σ, negative PNA events with an index below -1, and a neutral PNA with an index between -1 and 1. Figure 2.10a illustrates the disparity of SOM node frequency between positive and negative PNA events. As expected, positive PNA events are largely characterized by jet extensions. Node 8 is the dominant pattern characterizing positive PNA events, with a FOC near 30%, followed by nodes 4 at 22% and 12 at 18%. This is in stark contrast to negative PNA events, which are largely characterized by nodes 5, 9, 10, and 11 -variations of jet retractions and/or a split jet with equatorward and poleward components. Overall, it is evident that the frequencies of many of the SOM nodes are well associated with the PNA. The nodes

exhibiting the weakest relationship with the PNA are nodes 1 and 2, which both illustrate a reduced FOC during both positive and negative PNA events.

Another dominant Northern Hemisphere teleconnection pattern strongly tied to weather and climate variations is the AO (Thompson and Wallace 1998; Higgins et al. 200). During a positive AO, anomalously low pressure lies over the Arctic, whereas anomalously high pressure sits over the north Pacific and Atlantic basins. The negative phase is characterized by a similar pattern but of opposite sign. As in the PNA analysis, daily AO indices are employed and partitioned into positive AO events (above an index of 1σ), negative AO events (below -1σ) and neutral AO events (between -1σ and 1σ). Figure 2.10b reveals that positive AO events are most frequently characterized by nodes 5 and 9, whereas negative AO events are most frequently characterized by nodes 8, 7, and 12. However, the FOC is more evenly distributed during AO events than for PNA events, with differences from the climatological FOC remaining below 4% for most of the nodes. Nodes 8, 5, and 12 illustrate the largest disparity between positive and negative AO events, which suggests that they are the most strongly associated with the AO teleconnection pattern.

As evidenced by the correlation between the timeseries of node 12 seasonal FOC and the ENSO index (0.58), the SOM node frequency distribution is also associated with ENSO events. This relationship is examined through applying the Niño-3.4 index and distinguishing between El Niño events (above a Niño-3.4 index of 1), La Niña events (below -1), and a neutral ENSO (between -1 and 1). As for the PNA and AO events, FOC is then calculated during each of the three categories. Illustrated in Figure 2.10c, it is unsurprising that El Niño events are most frequently accompanied by jet extensions (nodes 4, 8 and 12). Conversely, La Niña events are most frequently associated with retractions and/or poleward deflections (nodes 1, 2, and 3), as well as node 4. However, as in the frequency distribution during AO events, the discrepancies in FOC

between positive and negative events are much lower than the discrepancies evident during PNA events, with node 12 exhibiting the largest FOC difference between events. The more substantial SOM node FOC changes associated with PNA events could be a reflection of the extratropical eddy dynamics largely influencing PNA growth through interactions with the jet stream (e.g. Simmons et al. 1983; Borges and Hartmann 1992; Borges and Sardeshmukh 1995; Mori and Watanabe 2008; Franzke et al. 2011).

2.2.3. MJO and SOM Nodes

Another important teleconnection that has been tied to changes within the north Pacific jet is the MJO. The MJO is the leading mode of tropical intraseasonal variability that is characterized by anomalous tropical convection migrating east from the Indian Ocean toward the Pacific in 30-60 day cycles (e.g. Madden and Julian, 1971). The anomalous convection associated with the MJO, like the anomalous convection associated with ENSO events, can act as a point source for Rossby waves generated by the upper-tropospheric horizontal divergence and latent heating (Hoskins and Karoly 1981; Kiladis and Weickmann 1992). The subsequent Rossby wave train can then propagate eastward and poleward into the vicinity of the north Pacific jet, interacting with the extratropical flow. However, the timescale and intensity within which the Rossby wave train propagates from the tropics and into the extratropics are dependent not only on the longitudinally varying extratropical basic state, but also on the initial longitudinal location of the enhanced convection (Hoskins and Ambrizzi 1993; Jin and Hoskins 1995). Therefore, the MJO, a longitudinally propagating heat source, is a complicated and important teleconnection to consider for wintertime extratropical variability.

An MJO event is typically characterized by 8 phases representing active and suppressed convection over different regions throughout the course of the event (Wheeler and Hendon, 2004).

During phases 2 and 3, the enhanced convection is over the Indian Ocean with suppressed convection over the tropical west Pacific. By phases 4 and 5, the enhanced convection migrates towards the Maritime Continent, then to the Pacific by phases 6-8 with suppressed convection over the Indian Ocean. By phases 8 and 1, the convection weakens over the Pacific and enhanced convection develops over the western Indian Ocean.

Following a method similar to that employed by Cassou et at. (2008) and Lee et al. (2020), the influence of the MJO on the 12 SOM jet states is investigated through calculating the percent change in anomalous frequency of occurrence of the 12 nodes following strong MJO phases (Figs. 2.11 – 2.13). The percent change is calculated at each lag between 1 and 16 days following the strong MJO phase. Strong MJO events are identified using the Real-Time Multivariate MJO (RMM) indices from the Australian Bureau of Meteorology for 1979-2019 NDJFM cold seasons (Wheeler and Hendon, 2004; http://www.bom.gov.au/climate/mjo/). The indices consist of RMM1 and RMM2, defined by the leading two EOF/PCs of satellite-observed outgoing longwave radiation anomalies and 850-hPa and 200-hPa zonal wind anomalies. MJO amplitude is determined by $\sqrt{RMM1^2 + RMM2^2}$, in which amplitudes greater than 1 are considered. The MJO phases are then organized into 9 phases- phases 1-8 are the phases described above and as in Wheeler and Hendon (2004), and the 9th phase, or phase 0, consists of days in which the amplitude is < 1. Additionally, ENSO events are filtered to remove constructive or destructive interference that might impact the MJO signal on jet node FOC. A neutral ENSO is identified when the Niño-3.4 index falls below 0.5 and exceeds -0.5, El Niño events are identified when the Niño-3.4 index exceeds 0.5, and La Niña events are identified when the Niño-3.4 falls below -0.5. As in Lee et al. (2020), anomalous occurrences are subjected to two significance tests. The first is a χ^2 test for the anomalous frequency distribution of the 12 SOM nodes together at each MJO phase and lag, and

the second is a binomial test for the individual nodes. Statistical significance is established only if the anomalous FOC passes both the χ^2 test at the 99% significance level and the binomial test at the 95% significance level.

In comparing SOM nodes featuring jet retractions, jet extensions, poleward deflections, equatorward deflections, and weaker anomalies, the existence of statistically significant anomalous occurrences and a slope as a function of lag following active MJO phases indicates a MJO forcing. Beginning with MJO events during a neutral ENSO state, the retraction and equatorward deflection denoted by node 9 illustrates the largest increase in anomalous occurrence during MJO phase 1, approaching 200% in the following week (Fig. 2.11). By MJO phases 2 and 3, however, the retraction denoted by node 5 exhibits enhanced frequencies, while node 9 shifts from an >100% increase in the 5 days following phase 2, to an ~50% decrease by day 8. Although nodes 9, 10, and 11 all feature equatorward deflections, nodes 9 and 5 are characterized by stronger negative anomalies in the climatological jet exit region, suggesting that earlier phases of the MJO are associated more strongly with negative zonal wind anomalies confined to the jet exit region. Extended nodes 8 and 12 also have reduced frequencies between 50-100% during the early MJO phases. During the middle phases of the MJO, nodes 5 and 9 exhibit significant reduced regime frequency in the following 2-14 days, whereas the extension denoted by node 12 begins to increase in FOC in the week following MJO phase 5. Between MJO phases 5 and 7, the anomalous frequencies for node 12 approach 200%. The increase in node 12 FOC is supplemented by a decrease in FOC of nodes 5 and 9. However, by MJO phase 7, node 9 shifts again from negative anomalous frequencies between 1-5 days to positive anomalous frequencies in the 8-14 days following the active phase. Overall, the nodes most strongly tied to the progression of the MJO during ENSO neutral events are nodes 5, 9, and 12.

The anomalous frequency distribution for MJO events during El Niño episodes illustrates key statistical differences. During El Niño episodes, MJO phase 1 is largely characterized by increases in node 9 and 12 FOC (Fig. 2.12). However, the retracted node 9 only increases in frequency beyond lag 5, whereas extended node 12 begins to decrease in frequency beyond lag 5. MJO phases 2 and 3 are not as discriminative for SOM node regimes, with either a weak or nonexistent slope as a function of lag for most of the nodes. By MJO phase 4, with enhanced convection migrating into the west Pacific, nodes 5 and 9 begin to decrease in anomalous occurrence, while node 12 exhibits a gradual increase over lags 7 to 16. Between MJO phases 5 and 8, the anomalous FOC for node 12 reaches 200-300%, exhibiting much larger anomalous occurrences than during neutral ENSO MJO phases 5-8. The extension characterized by node 8 also presents a marginal increase in FOC, whereas nodes 1, 2, 5, and 9 reduce in FOC within the later phases of the MJO.

The anomalous FOC during active MJO phases and La Niña episodes (Fig. 2.13) illustrate even stronger statistical differences when compared to ENSO neutral and El Niño episodes. For example, MJO phase 1 is no longer largely characterized by SOM node 9 or 12, but rather by substantial frequency increases in node 1 at lags 5-14. This is in stark contrast to El Niño and ENSO neutral events, in which the MJO has little to no influence on node 1. The influence of the MJO on node 1 FOC is evident from phases 1-4. Also during the early MJO phases, nodes 7, 8, 10, 11, and 12 all exhibit a reduction in frequency. MJO phases 4 and 5, however, are evidenced to have an impact on equatorward deflected node 2, with anomalous frequencies exceeding 200% between lags 1-5, while extended node 12 depicts the strongest frequency reduction between phases 3 and 5. Between MJO phases 6 and 8, there are no significant increases in FOC for any of the nodes; however, retracted and/or equatorward deflected nodes 9 and 10 exhibit reduced frequencies.

Overall, the lagged relationships between the MJO phases and anomalous SOM node occurrences illustrated in Figs. 2.11-2.13 demonstrate a teleconnections pattern consistent with previous findings and provide a more detailed analysis of the subtleties of the jet stream anomalies following specific MJO phases. Separation of strong MJO events between ENSO neutral, ENSO positive, and ENSO negative also illustrate the importance in stratifying ENSO phase when investigating MJO teleconnections. In particular, retracted and/or equatorward deflected nodes 5 and 9 contribute the most to the increased frequencies associated with MJO phases 1-2 during ENSO neutral events, with enhanced convection over the Indian Ocean and suppressed convection in the Pacific basin. MJO phase 4, on the other hand, is not as discriminative for the jet regime. The later phases of the MJO are largely characterized by increases in extended node 12 FOC, when the enhanced convection migrates over the Pacific basin. The large increases in node 12 FOC during MJO phases 1 and 4-8 during El Niño events can be attributed largely to ENSO, given that the FOC during ENSO positive events (Fig. 2.10c) was over two-fold the climatological FOC. However, there is a slope as a function of lag evident in both ENSO neutral and ENSO positive episodes for node 12, suggesting that the MJO is a precursor to node 12 jet extensions. This relationship is not as robust for other extensions denoted by node 8 and 4, which further establishes the importance in complementing the previous EOF-identified 4-pattern model of Pacific jet variability. The teleconnections for the MJO during La Niña episodes are much different. Unsurprisingly, extended nodes 8 and 12 exhibit negative or insignificant anomalous frequencies, as convection over the tropical east Pacific is suppressed. SOM nodes 1 and 2, however, were characterized by the largest increases in FOC following early and middle phases of the MJO. While these large increases were only noted during La Niña episodes, the minimal increases in FOC

during La Niña illustrated in Fig. 2.10 suggests that constructive interference between early phases of the MJO and La Niña leads to large increases in nodes 1 and 2 FOC.

2.4 Discussion and Conclusions

A novel self-organizing maps analysis is applied to 250 hPa zonal winds over 71 NDJFM cold seasons to better understand variability within the wintertime Pacific jet. Prior work in understanding intraseasonal Pacific jet variability has proceeded from identification of the leading modes of variability: a zonal extension or retraction and a meridional deflection of the jet exit region, as depicted in EOF/PC analysis (e.g. Athanasiadis et al. 2010; Jaffe et al. 2011; Griffin and Martin 2017; Breeden and Martin 2018; Winters et al. 2019a, 2019b). The SOM analysis described in this chapter expands and compliments previous EOF/PC analysis, identifying 12 archetypical Pacific jet patterns resembling variations of the extended/retracted and poleward/equatorward deflected patterns of EOF-based Pacific jet variability (e.g., Schubert and Park 1991; Athanasiadis et al. 2010; Jaffe et al. 2011), as well as new complex modes of variability not captured by these previous analyses. Examples of these include an enhancement of the jet characterized by node 7, a poleward deflected jet jutting into the Gulf of Alaska characterized by node 2, and a split jet with extratropical and subtropical counterparts denoted by nodes 9 and 10.

The expanded SOM-based jet regimes add important detail characterizing wintertime Pacific jet variability. For example, composites of Z500, SLP, and 850T illustrate that seemingly minor variations in EOF 1 and 2-like patterns are tied to distinct differences in synoptic-scale anomalies over the Pacific and North America and both upstream and downstream low-level temperature anomalies. Additionally, investigation of intraseasonal, interannual, and decadal variability of SOM node FOC reveals that there is variability at both the inter- and intra-seasonal timescales. Seasonally, November is characterized by a higher FOC of poleward and/or extended jet nodes 3

and 4, as well as of a retracted and equatorward deflected node 10. Conversely, extended node 12 has its lowest FOC in November (2.2%). Mild variations are noted between December, January, and February, with jet extensions becoming more frequent and peaking in January and February. By March, retracted nodes 1 and 5 become more common.

The FOC for each node varies even more substantially at interannual timescales, with no statistically significant trend. Nevertheless, the interannual variation is evidenced to be, in part, tied to teleconnection patterns like the PNA, AO, ENSO, and MJO. Node 12, in particular, exhibited one of the strongest relationships to the PNA, AO, and ENSO, while node 1 exhibited one of the weakest relationships to the aforementioned teleconnection patterns. However, in examining anomalous FOC associated with strong MJO events during La Niña episodes, the signal for node 1 suggested an MJO influence, more than doubling its FOC following early phases of the MJO. During ENSO neutral or El Niño episodes, however, early phases of the MJO coincided or preceded FOC increases in node 9. Although these teleconnection patterns provide insight into the varying nature of SOM nodes at inter- and intra-seasonal timescales, a key objective of this work is to better understand the likelihood and nature of transitions between common wintertime Pacific jet patterns. Therefore, the next chapter characterizes transitions between the 12 SOM nodes at short 5-day timescales, mid 10-day timescales, and longer 15- and 20-day timescales.

SOM Grid Size	Quantization Error	Topographic Error
2x2	389	.3 %
3x3	377	1.8%
3x4	372	4.9%
4x4	366	13%
4x5	362	15%

Table 2.1: Quantization and topographic error of SOM grid for various grid sizes.

SOM Node	Mean Residence Time (days)	Max Residence Time (days)	Average QE Error (Grid mean: 373)
Node 1	2.4	18	374
Node 2	2.4	13	361
Node 3	2.2	10	356
Node 4	2.7	16	369
Node 5	2.5	11	381
Node 6	2.2	20	371
Node 7	2.5	10	364
Node 8	2.6	11	364
Node 9	3.2	18	399
Node 10	2.4	17	387
Node 11	3.4	18	385
Node 12	4	44	375

Table 2.2: Characteristic residence times and quantization errors for each SOM node within the SOM grid.
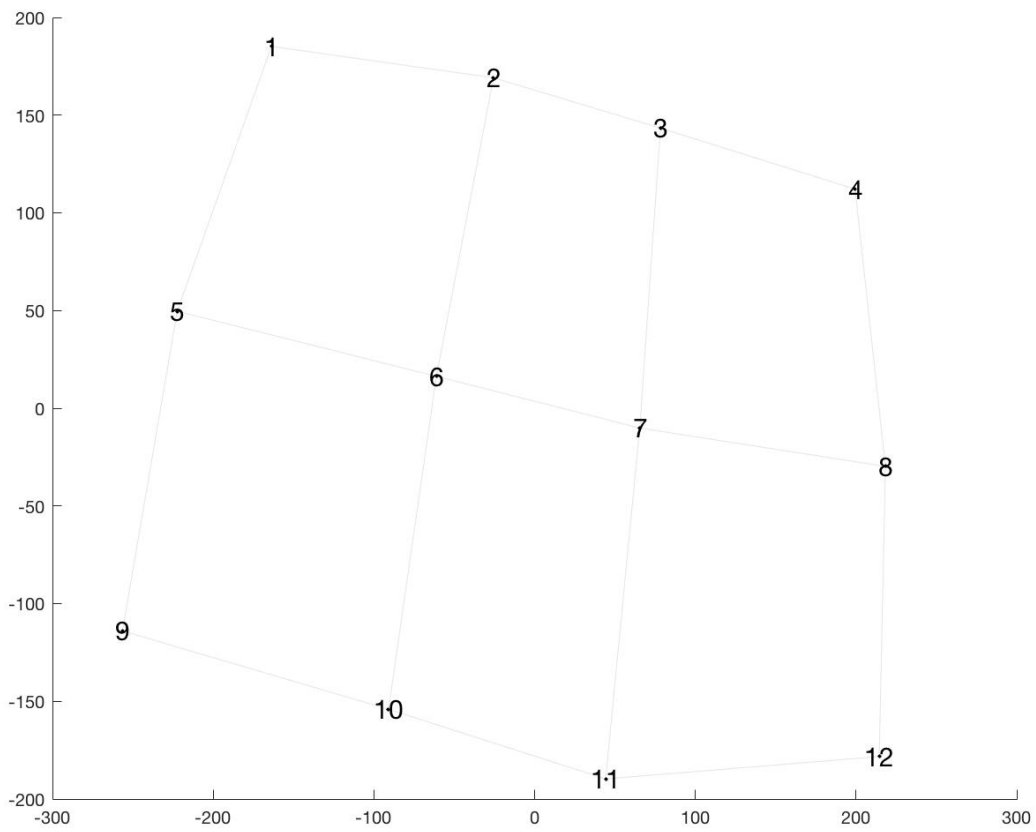
Figure 2.1: Sammon Map of the Euclidian distances between each node in the 3x4 SOM grid on a two-dimensional distortion plane.

EOF1 - 14% Var. Expl.

EOF2 - 10% Var. Expl.
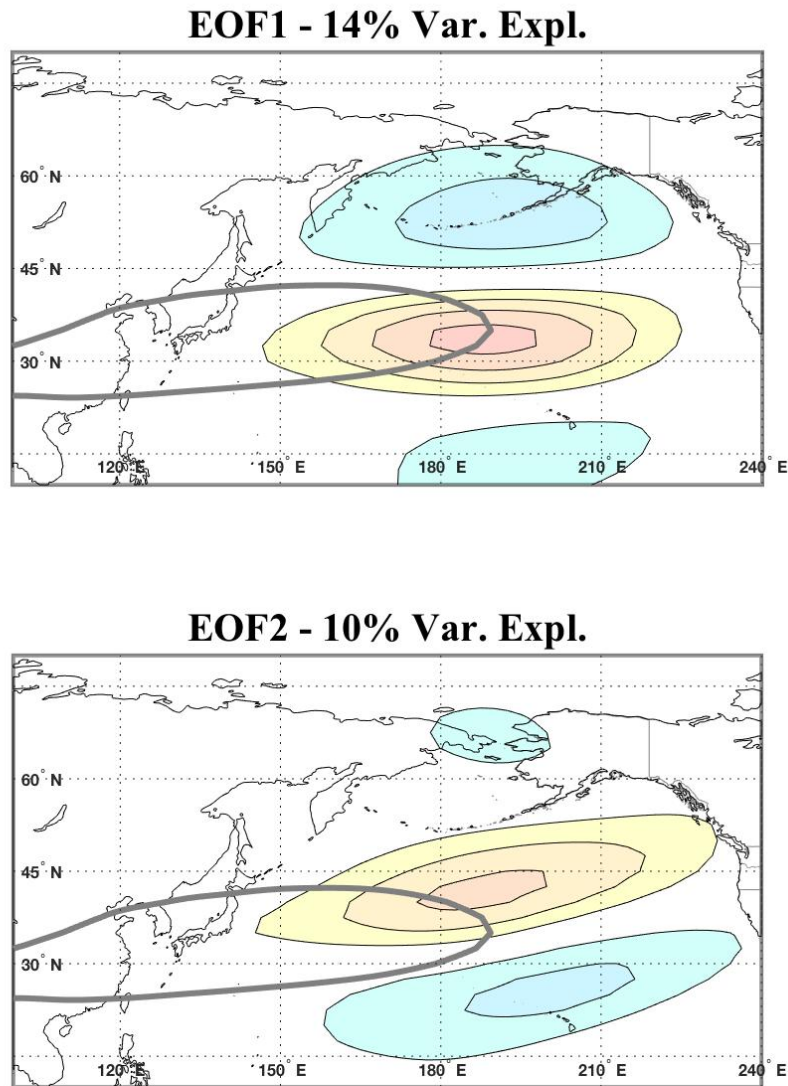
Figure 2.2: EOF pattern of the 250-hPa zonal wind over the North Pacific. Perturbations are shaded (ms^{-1}) every 4 starting at 4 (-4). Mean 40 ms^{-1} isotach over the 71 cold seasons is contoured in grey. (top) EOF1 (bottom) EOF2.
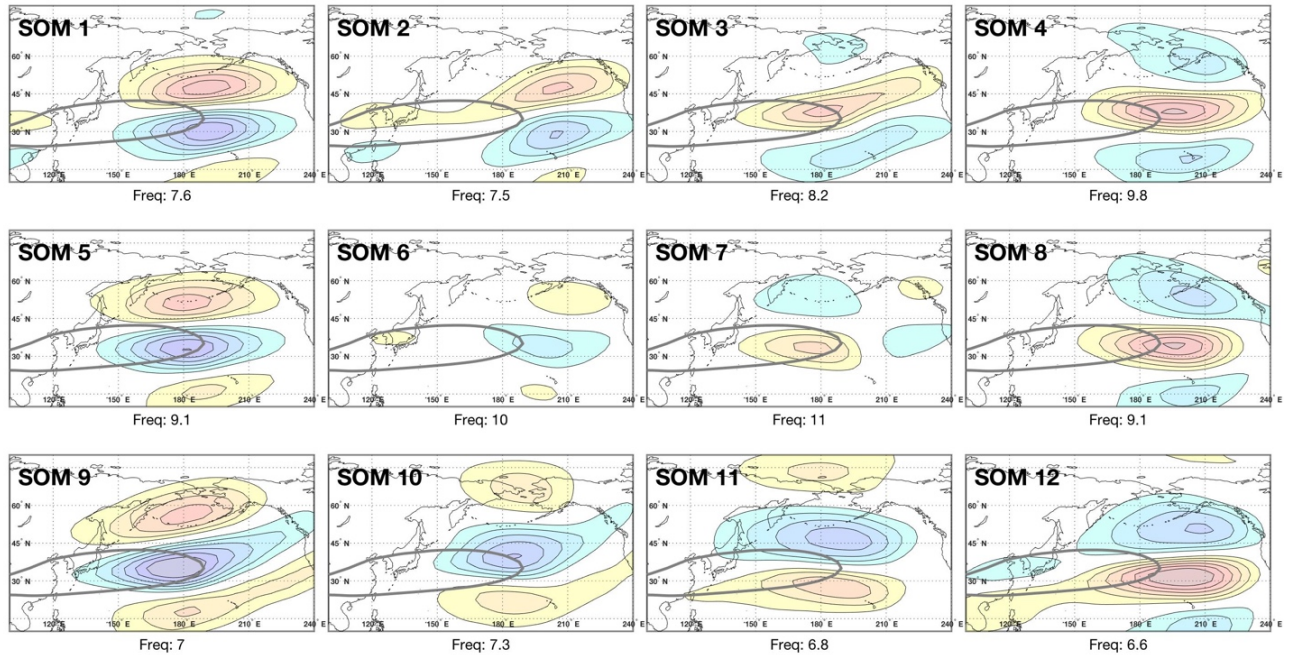
Figure 2.3: SOM grid of 12 most recurring patterns of the wintertime Pacific basin 250-hPa zonal wind. Anomalies of the 250-hPa isotachs (ms^{-1}) are shaded in warm (cool) colors every 4 starting at 4 (-4). The mean 71 cold season 40 ms^{-1} isotach is in gray. Below each node is the associated frequency of occurrence (in %) relative to all other nodes.
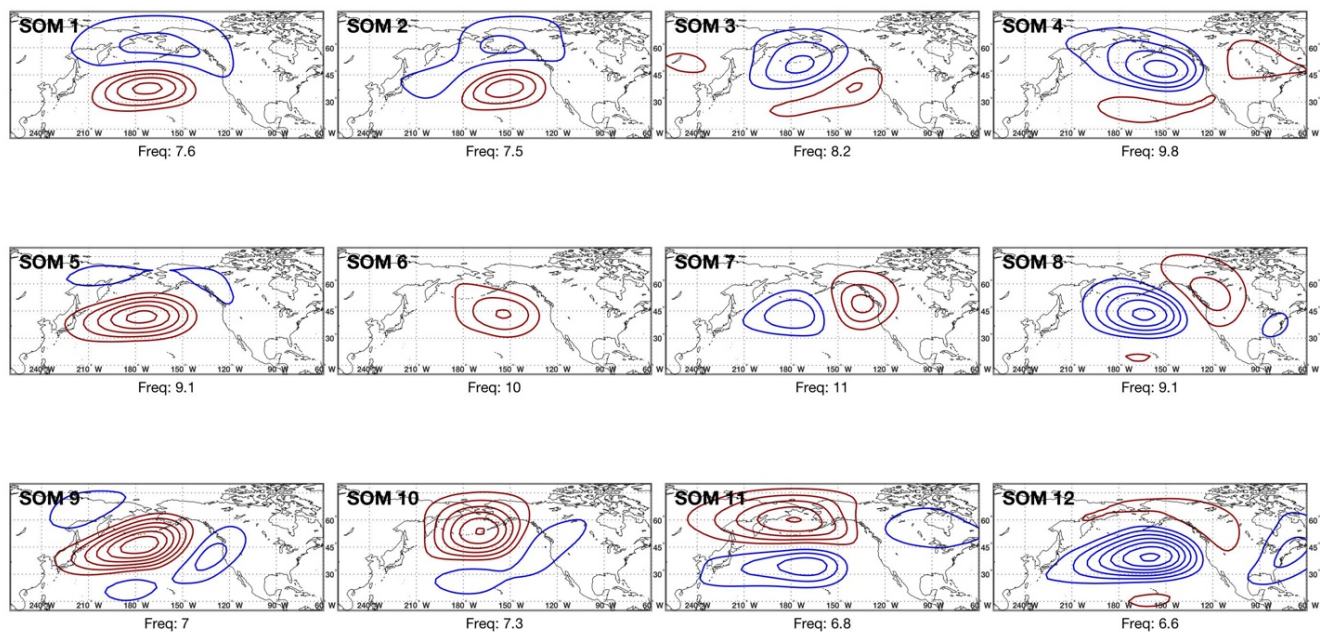
Figure 2.4: Composite 500-hPa geopotential height anomalies of days within each SOM node. Below each node is the associated frequency of occurrence (in %) relative to all other nodes. Positive (negative) 500 hPa geopotential height (m) anomalies are contoured in red (blue) every 25m starting at 25 (-25).
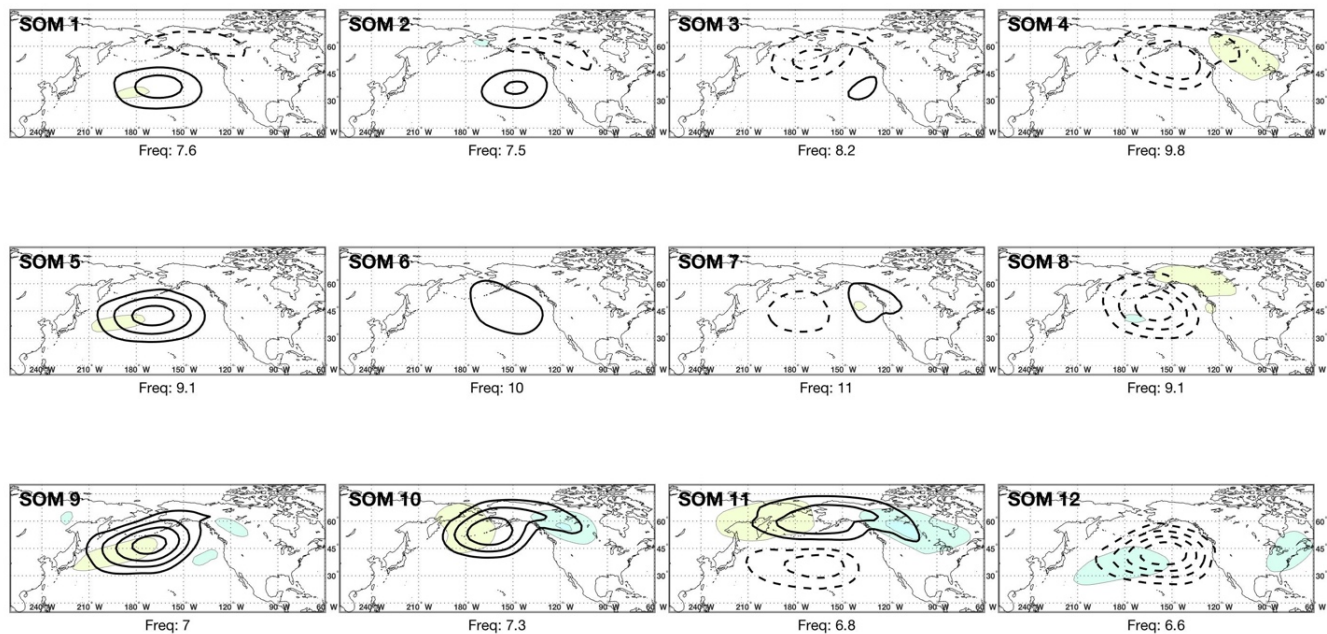
Figure 2.5: As in Fig. 5 but composite positive (negative) SLP anomalies (hPa) in solid (dashed) black lines contoured every 3 hPa starting at 3 hPa (-3 hPa) and 850 hPa temperature anomalies (°K) in red/yellow (blue/purple) contoured every 2 K starting at 2 K (-2 K).
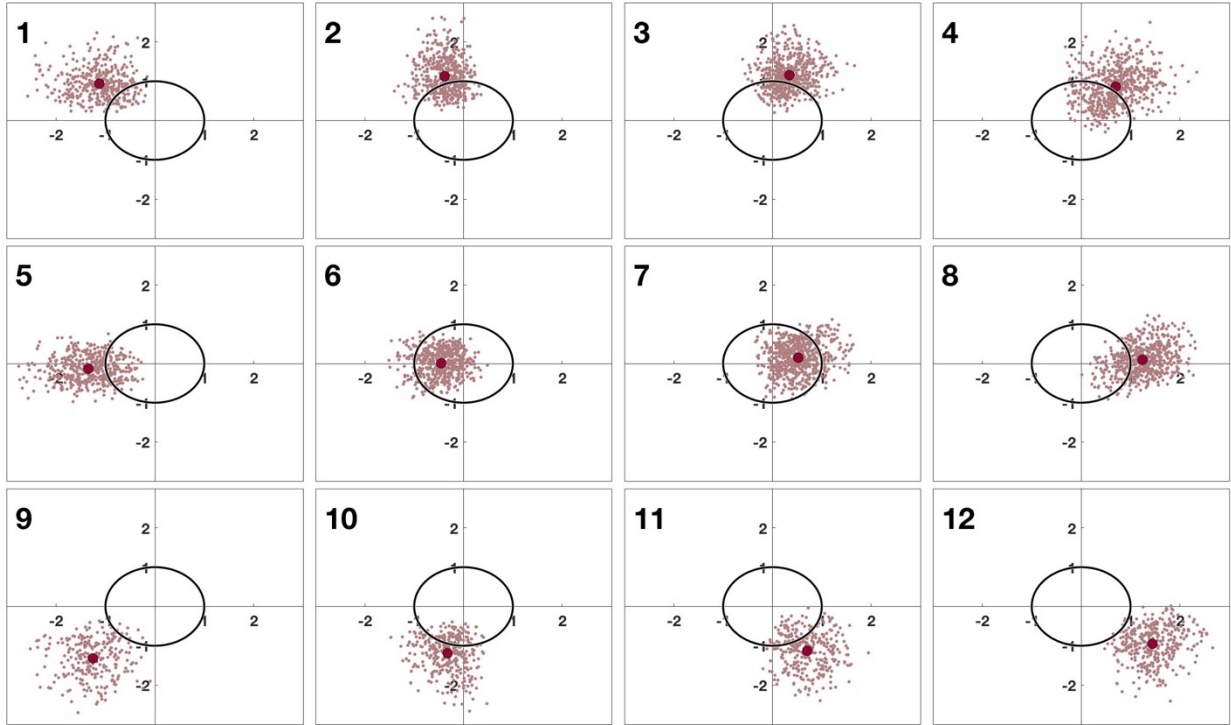
Figure 2.6: State of the daily Pacific jet (maroon circles) in the 2D phase space of the leading 250-hPa zonal wind PCs for every day comprising each of the 12 SOM nodes within the 71 cold seasons (1948/49-2018/19). Black circles represent the 2 and 4 contours of magnitude in the EOF/PC phase space.
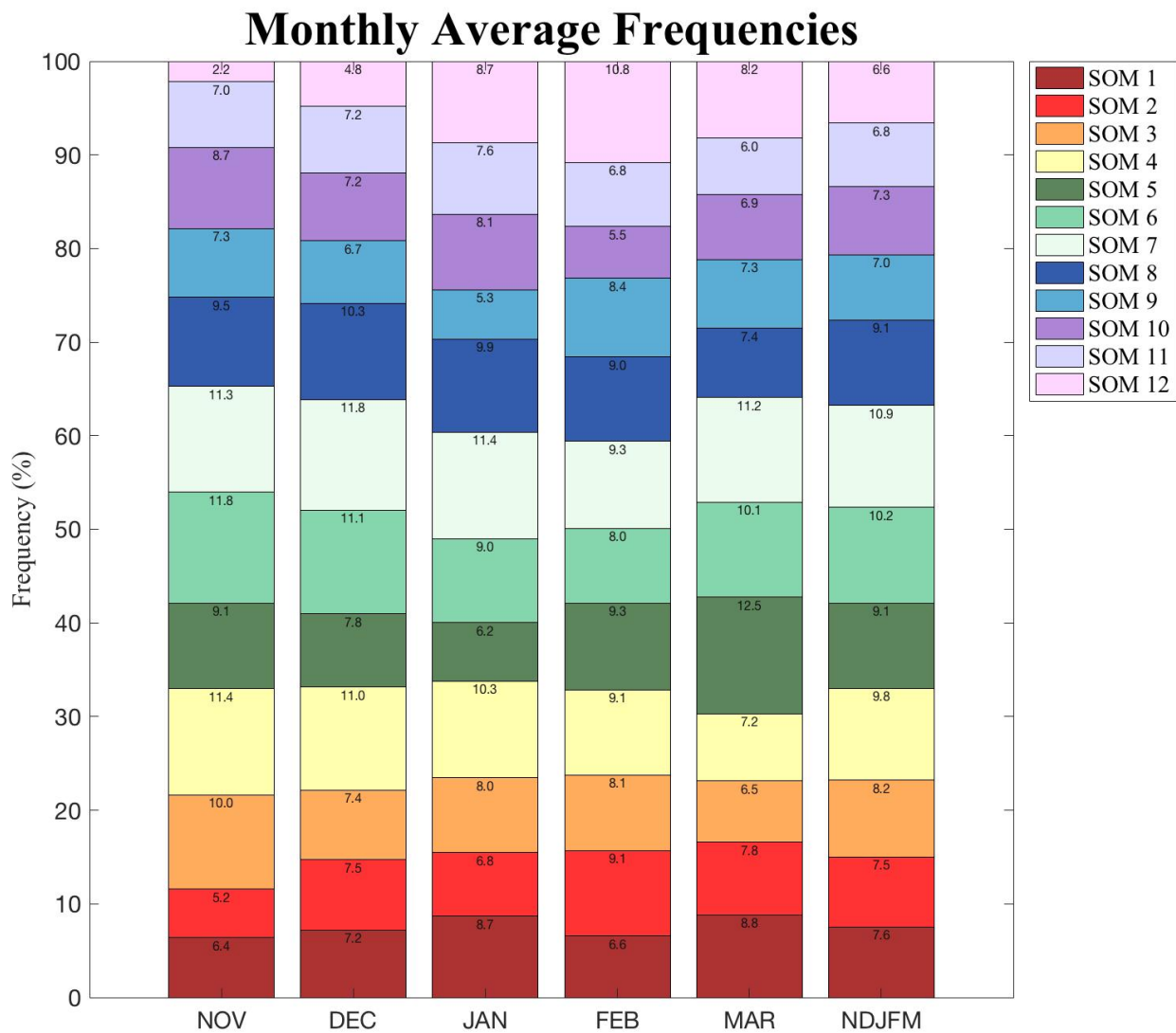
Figure 2.7: Percent frequency of occurrence for each SOM node during each month of the cold season.

49
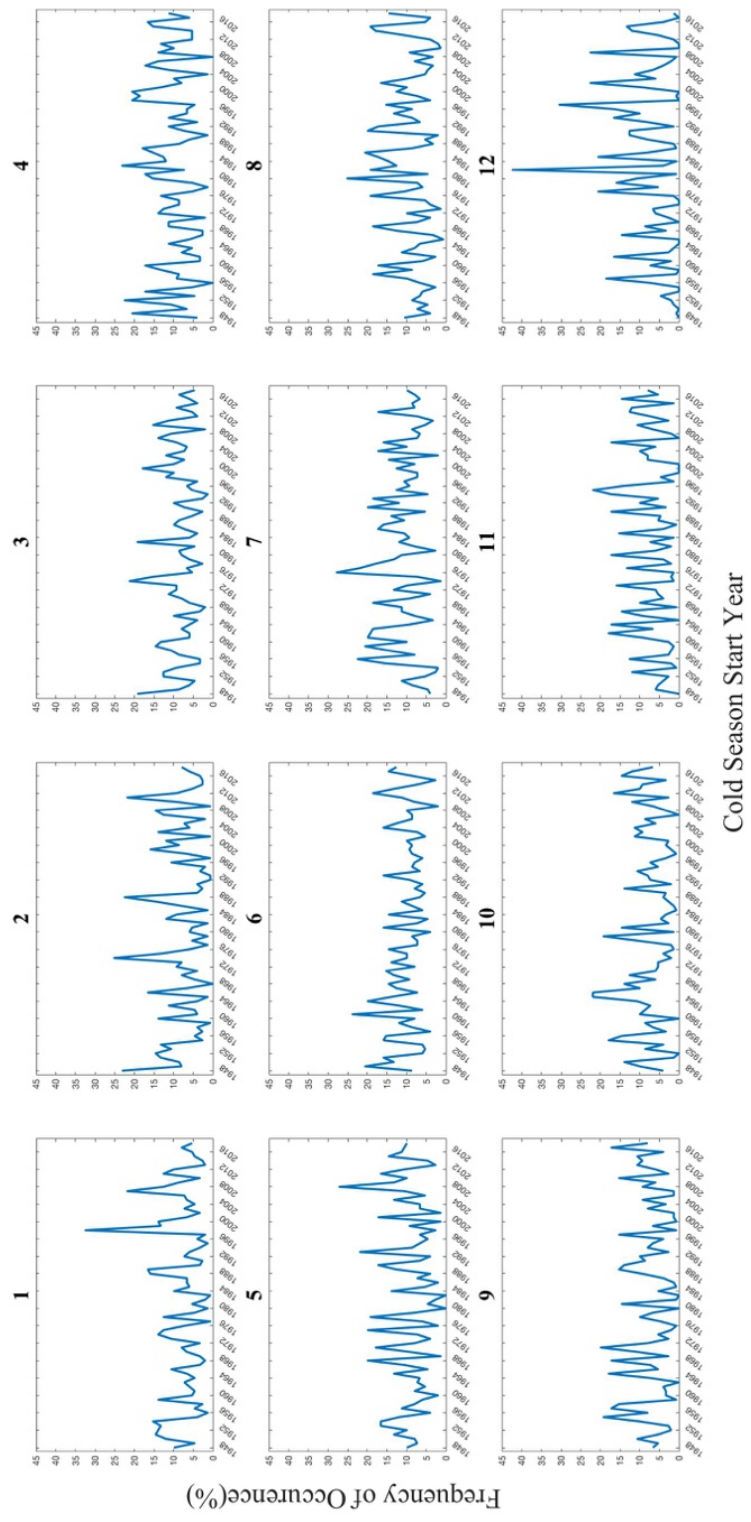
Figure 2.8: Percent frequency of occurrence for each SOM node during each cold season.
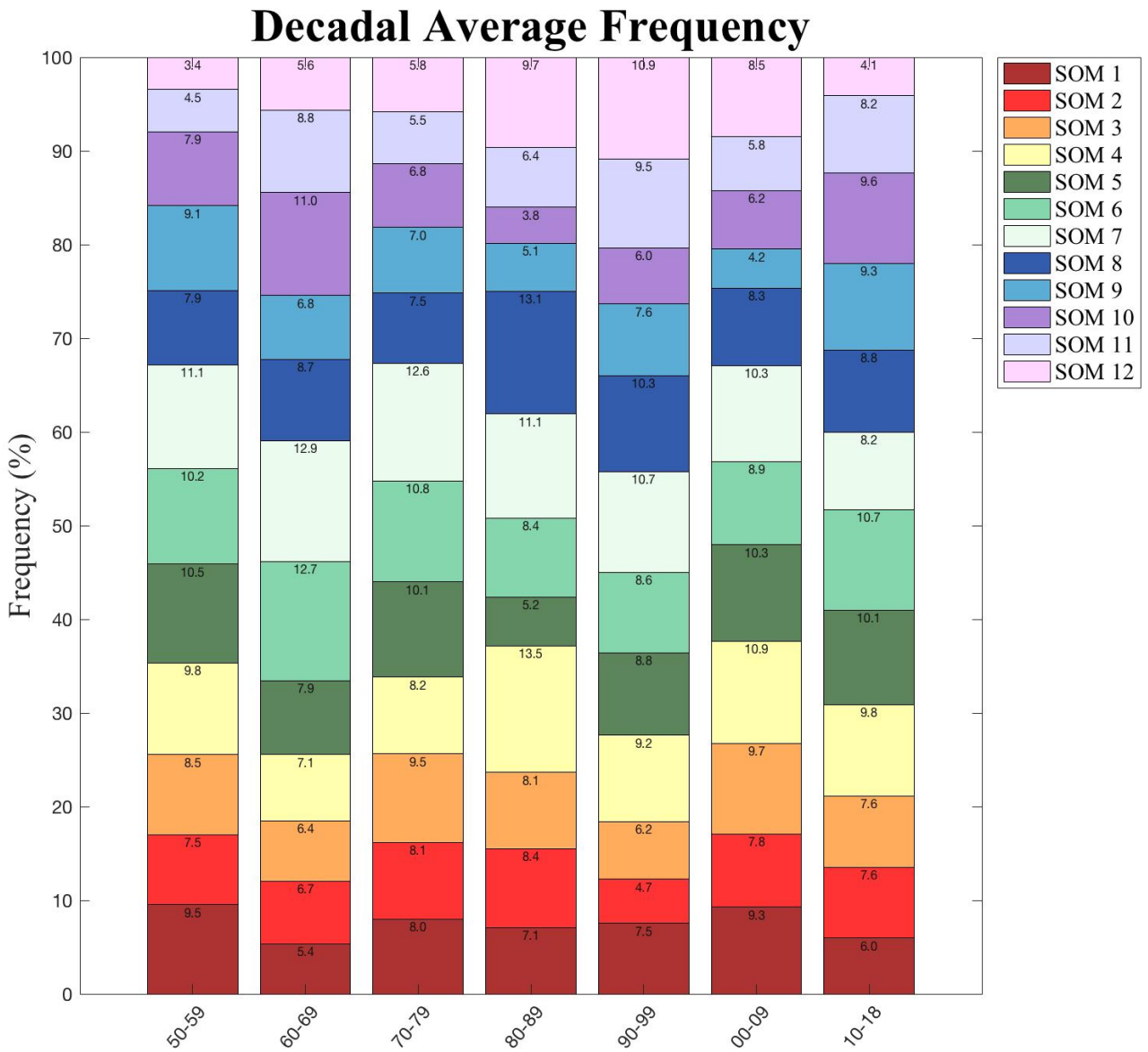
Figure 2.9: Decadal mean of frequency of occurrence for each SOM node beginning with 1950.
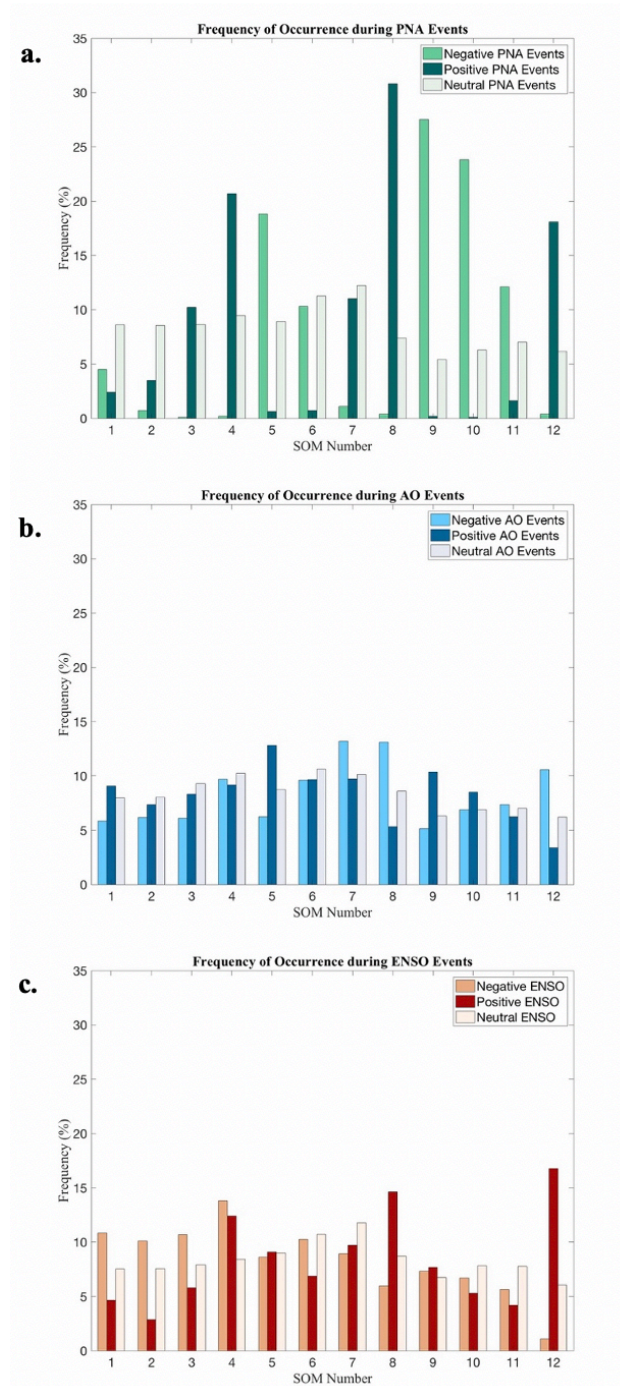
Figure 2.10: Frequency of occurrence of each SOM node for days characterized by PNA events (a), AO events (b), and ENSO events (c).

Anomalous FOC During MJO and Neutral ENSO
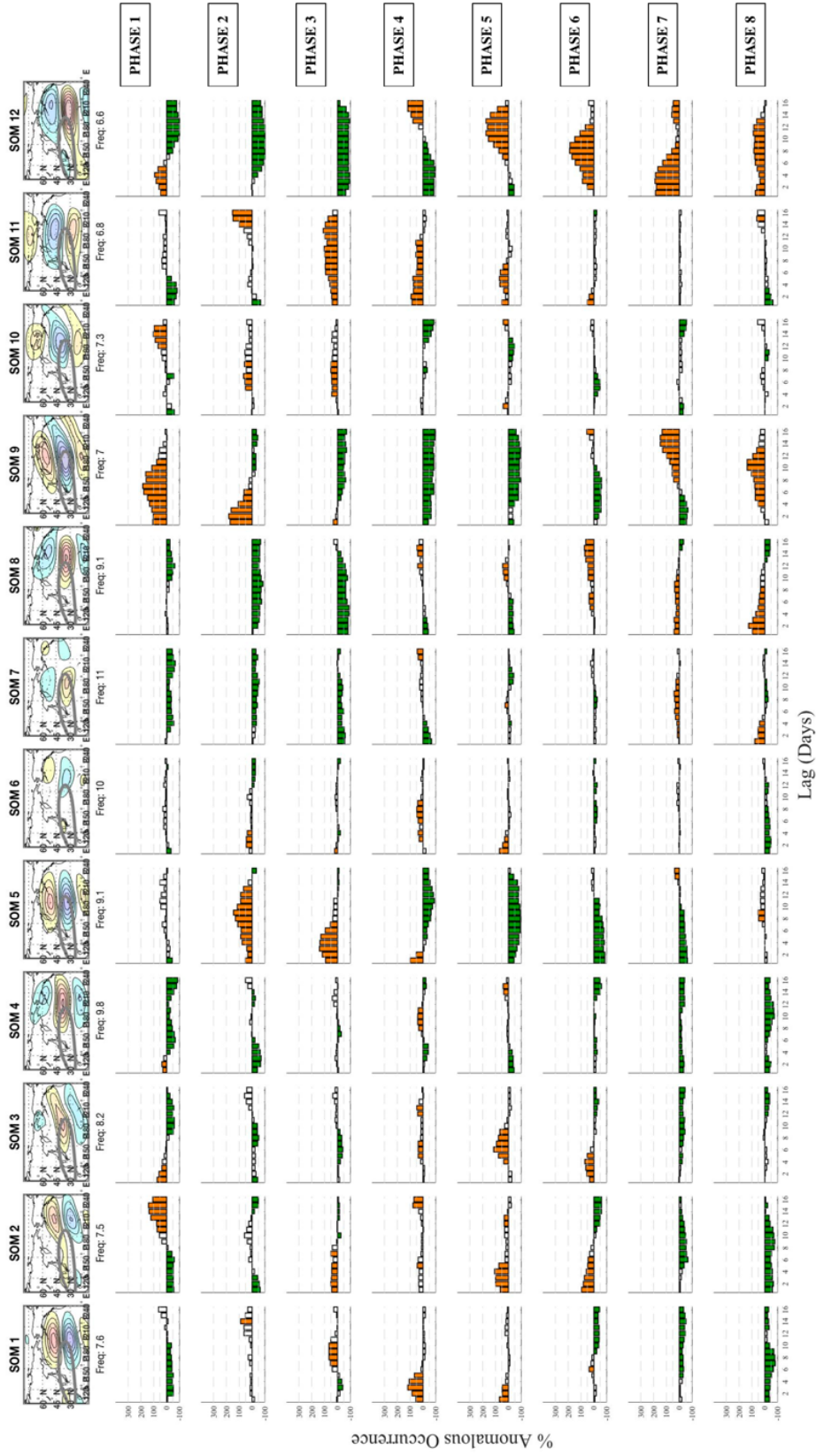
Figure 2.11. Lagged relationships between the eight phases of the MJO and SOM nodes during ENSO neutral events. For each active MJO phase, (RMM >1), the anomalous FOC of SOM nodes is plotted as a function of lag from 1 to 16 days after the active MJO phase. A 100% anomalous FOC denotes a FOC twice that of the climatological FOC for the SOM node, whereas a -100% anomalous occurrence denotes a FOC of 0. Orange (green) shading denote statistically significant anomalous FOC as determined from a χ2 test and binomial test.

53

Anomalous FOC During MJO and Positive ENSO
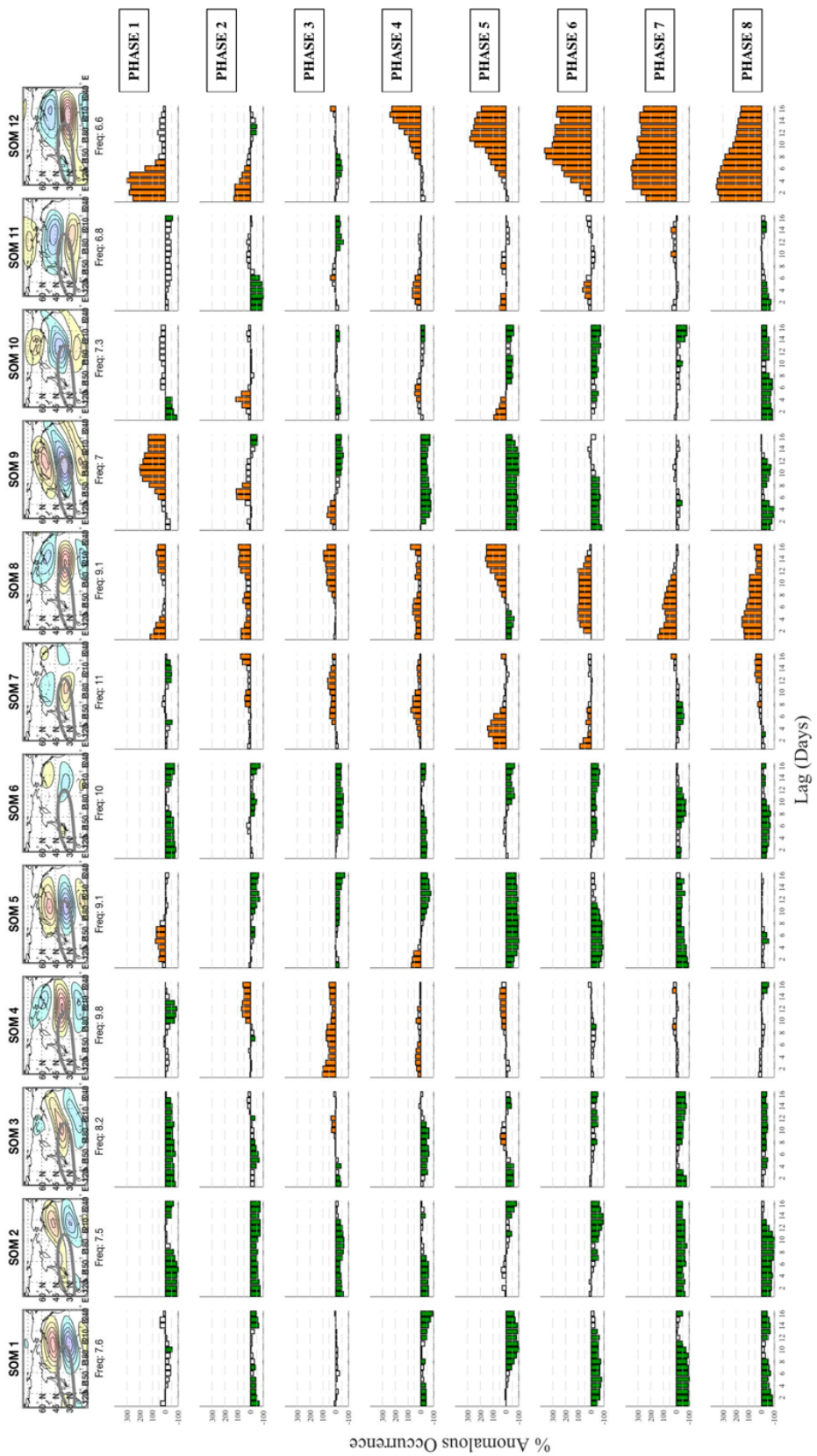
Figure 2.12. As in Fig. 2.11 but during positive ENSO events.
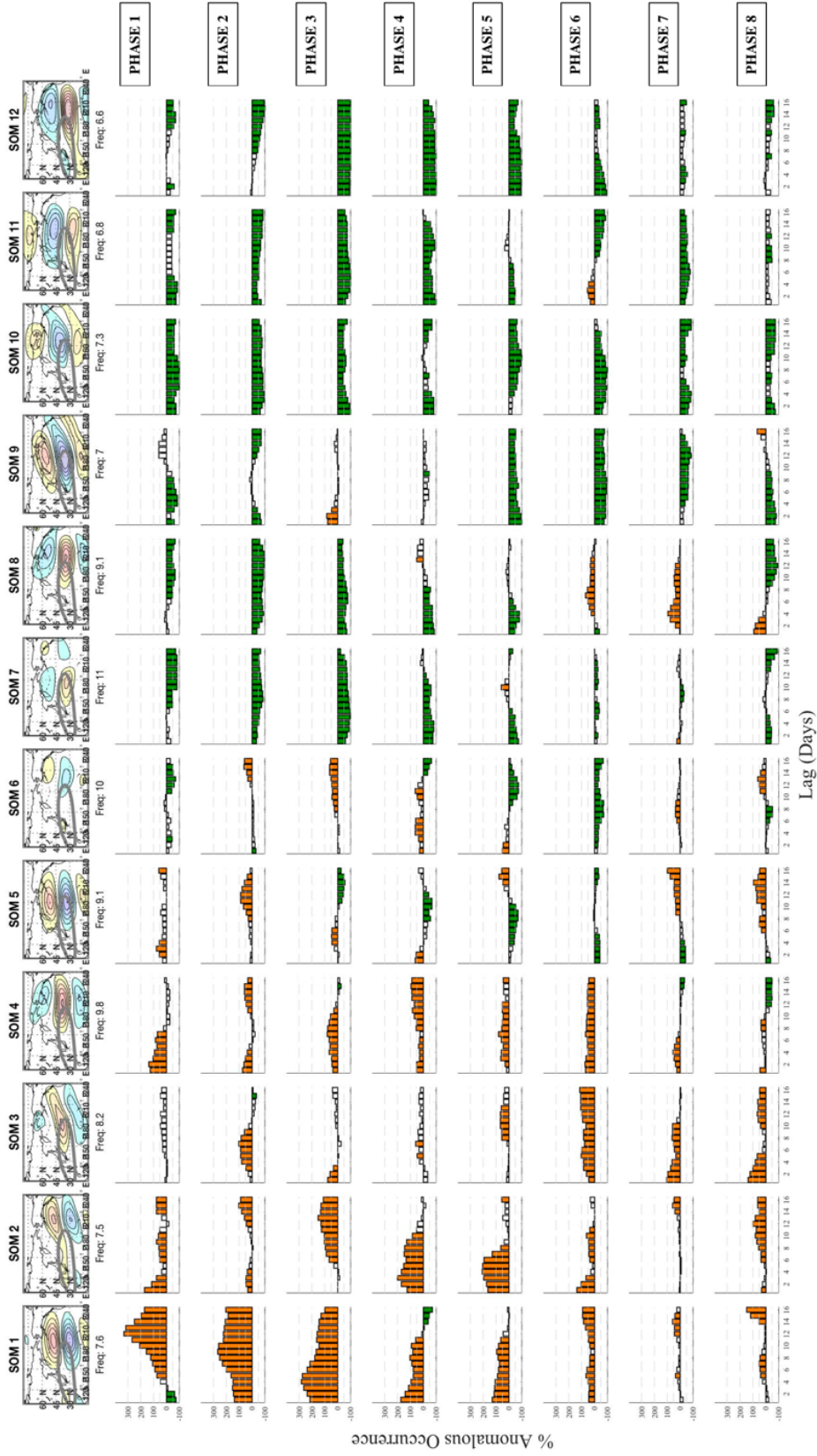
Figure 2.13. As in Fig. 2.11 but during negative ENSO events.

CHAPTER 3: PREFERRED AND UNLIKELY TRANSITIONS WITHIN THE NORTH PACIFIC JET

3.1 Methods

In the previous chapter, it was demonstrated that teleconnection patterns such as the PNA, AO, ENSO, and the MJO, are tied to distinct changes in SOM node FOC. Some of the nodes exhibit a stronger relationship to teleconnection patterns than others, suggesting that seemingly similar Pacific jet patterns like nodes 5 and 9, or nodes 4, 8, and 12 are likely driven by different extratropical and/or tropical processes. Furthermore, knowledge of the prevailing teleconnection pattern and its relationship to particular SOM nodes could offer additional value to medium and extended range forecasts. Also key to improving predictability at these timescales is a better understanding of Pacific jet transitions, including the likelihood and nature of transitions between representative wintertime Pacific jet patterns. As such, transition probabilities between SOM nodes are computed and analyzed in this Chapter to identify common and uncommon transitions at varying time scales. The analysis considers 5, 10, 15, and 20-day transition probabilities in order to elucidate differences between rapid transitions and longer two-to-three-week transitions. Transition probabilities are computed based off a first-order Markov chain:

$$P_{ij}(n) = P\{X_{t+n} = j \mid X_t = i\}, \tag{3.1}$$

in which the probability of transitioning into node j at lag n only depends on the initial node i. Thus, for the daily 250 hPa zonal winds within node j at $t = 0$, the total number of transitions to nodes 1-12 by the end of that interval[1] is tabulated. These values are referred to as transition totals, and there are 12 per starting node for each time interval. Next, the 12 transition totals are divided

---

[1] The transition total includes only days in which the 5, 10, 15, and 20-day intervals are within the same NDJFM season.

by the number of days in the complete time series that are occupied by the starting node to give a probability of each SOM node transitioning into any of the 12 nodes within the time lag of interest. For example, node 8 (a zonally extended jet, see Fig. 2.3), is identified in 975 of the 10,721 NDJFM days in the 71-year NCEP time series. These days represent starting points for 975 forward trajectories. The 10-day probability table totals the number of trajectories that end up in nodes 1-12 in the subsequent 10-day interval. The total for each node is divided by 975 to determine the 10-day probabilities of transitioning into node 1, node 2, and so on. A similar procedure yields transition probabilities for any N-day interval.

Following the work of Gu and Gervais (2021), statistical significance of the transition probabilities is determined through a Monte Carlo sampling method. The null hypothesis is that transitions between the 12 SOM nodes are random. In order to reject the null hypothesis, unconditional probabilities are produced by sampling 100 random days from the dataset and calculating the frequency of occurrence (FOC) of each SOM node within the sample. This is repeated 100,000 times to yield a distribution of FOC for every SOM node. A two-tailed t test is then performed to identify the transition probabilities above the 95% significance level.

Additionally, a "metatest" is performed based on Livezey and Chen (1983) and Wilks (2006) to assess the theoretical predictability of each SOM node. The method is based off of "field significance" or "global significance" in which the significance tests for each individual SOM node are evaluated jointly. The prior individual tests were evaluated at the significance level of 0.05, also known as α_{local}. Therefore, the global significance is assessed based on rejection of the global null hypothesis that for m number of local SOM node probabilities, significant at the level of α_{local},

$$\Pr\left(M \geq m\right) \leq \alpha_{global}, \tag{3.2}$$

where α_{global} is the level for the global significance, which is also 0.05. Thus, if the probability

of having m local null hypothesis rejections is less than or equal to 0.05, the global null hypothesis

is rejected, and the initial node is considered *theoretically predictable*. Pr $(M \geq m)$ is determined

through a binomial distribution, which assumes that the 12 individual SOM node significance tests,

K, are mutually independent,

$$\Pr(M \geq m) = \sum_{i=m}^{K} \frac{K!}{i!(K-i)!} (\alpha_{local})^i (1 - \alpha_{local})^{K-i}, \qquad (3.3)$$

Evaluation of Pr $(M \geq m)$ at various values of m between 1 and 12 reveals that the global null

hypothesis is rejected when m is greater than or equal to 3. Therefore, when the number of

statistically significant probabilities for each row of the transition tables equals or exceeds 3, the

initial node is determined globally significant and theoretically predicable at that lag time.

To elucidate common and infrequent transitions, transition probabilities are analyzed at

shorter 5-day timescales (Fig. 3.1a), medium 10-day timescales (Fig. 3.1b), and extended 15-day

and 20-day timescales (Fig. 3.1c and 3.1d). Statistically significant enhanced (reduced) transition

probabilities are depicted in red (blue) boxes to illustrate preferred (unlikely) pathways for each of

the 12 SOM nodes.

3.2 November-March North Pacific Jet Transitions

3.2.1. 5-Day Transitions

The 5-day transition probability table (Fig. 3.1a) illustrates that a majority of the SOM

nodes are more likely to persist than transition into another node in this short interval. The

increased likelihoods of persistence range from 15% (node 3) to 32% (node 12). There is only 1

node that has a larger probability of transitioning into another node than persisting. Node 3, which

depicts a poleward deflection extending into British Columbia, has a 15% likelihood of remaining

in node 3 and a slightly higher 16% likelihood of transitioning into the poleward deflected and stronger extension denoted by node 4. It also has a statistically significant increased probability of 14% of transitioning into the extension denoted by node 8 as well. The poleward deflected node depicted by node 2, however, has a reduced probability of transitioning into the extended node 8, as well as nodes featuring equatorward deflections (9-12). The most likely transition from node 2 outside of persistence (24%) is into nodes 1 (13%) and 3 (15%). Node 1 has only one preferred transition outside of persistence (23%) into node 2 (16%). Like node 2, unlikely transitions are into extended nodes 8 and 12, and equatorward deflected nodes 10 and 11.

Nodes depicting extended regimes (4, 8, 12) have increased likelihoods of transitioning into other extended states. Beginning with node 4, it is most likely to persist (23%) or transition into node 8 (16%). The extended node 8, however, has 3 preferred transitions outside of persistence (24%). Node 8 is either likely to transition into node 4 (15%), 7 (18%), or 12 (14%), and unlikely to transition into nodes 1, 5, 6, 9 and 11. Node 4 also has reduced transition likelihoods into nodes 9 and 11. The extension denoted by node 12 has a 32% likelihood of persisting, a 14% probability of deflecting poleward to a more canonical extended state (node 8) and an 12% likelihood of weakening and deflecting equatorward into node 11. As in probabilities for nodes 4 and 8, it is unlikely to transition into the strong retraction denoted by node 9. It also has reduced likelihoods of transitioning into nodes 1-3 and 5.

Retracted states denoted by nodes 5 and 9 exhibit preferred transitions into one another, as well as persistence of 24% and 28%, respectively. Additionally, it is unlikely for the retracted nodes to transition into jet extended/jet enhanced states 7, 8, and 12. Node 9, which features a stronger subtropical jet, also is unlikely to transition into poleward deflected nodes 2-4. Moving towards equatorward deflected nodes, node 10 is most likely to persist (29%) or transition into

node 11 (14%), whereas it is least likely to transition into poleward deflections and/or extensions (3, 4, 8). Node 11, on the other hand, is likely to persist (24%), or transition into nodes 12 (18%) and 7 (17%). Like node 10, it is unlikely to transition into nodes 3 and 4, as well as nodes 1, 5, and 9. Lastly, the weakest anomaly states 6 and 7 have significant persistent probabilities of 17% and 18%, respectively. For node 6, this is the only significant likely transition, whereas unlikely transitions are into nodes 4, 8, and 12. Node 7, however, is likely to transition into node 8 and unlikely to transition into nodes 5 and 9. Overall, at timescales at and below 5-days, it is most likely that the Pacific jet will either persist or undergo a minimal transition into a neighboring node.

3.2.2. 10-Day Transitions

By 10-days, the number of statistically significant transition probabilities decreases substantially (Fig. 3.1b). Persistence at this interval is still a likely tendency for many of the nodes, with significant probabilities ranging from 13% for node 9 to 20% for node 12. However, poleward deflected node 3, retracted node 5, and weaker anomaly nodes 6 and 7 lose persistence by day 10. Only a handful of nodes have preferred transitions into other nodes. Poleward deflected node 2, for example, is likely to persist (16%) or transition into node 1 (12%), whereas it is still unlikely to transition into nodes 9 and 12. Node 3 only has one statistically significant reduced transition into node 9. The extension denoted by node 4 is also unlikely to transition into node 9, as well as into nodes 10 and 12. The retraction in node 5 only has 1 preferred transition into node 9 (14%) and is unlikely to transition into the extended node 12. Retracted node 9, however, still has an enhanced likelihood of persisting (13%), but it is more likely to transition into node 10 (15%) and unlikely to transition into node 8. Nodes 11 and 12 have some of the highest probabilities of transitioning into other nodes, with node 11 exhibiting a 17% likelihood of persisting and a 20%

likelihood of transitioning into node 12. Furthermore, Node 12 has a 20% likelihood of persisting and a 16% likelihood of transitioning into node 7. Both nodes have significant low probabilities of transitioning into retracted node 5, and node 12 is unlikely to transition into nodes 1, 9 and 10 as well. Lastly, the extension denoted by node 8 has only one significant high probability of persisting, and one significant low probability of transitioning into a retraction (node 5).

3.2.3. 15-Day Transitions

At extended-range timescales of 15 days, the number of statistically significant transitions decreases even further (Fig. 3.1c). Node 12 is the only node with a significant high probability (21%) of persistence (or a transition back into the initial node, hereafter referred to as *reoccurrence*). Otherwise, only a handful of nodes have significant preferred transitions into other nodes. Node 2, for example, still is likely to transition into node 1 (14%) and has another preferred transition into node 3 (13%). The extended and poleward deflected node 4 is most likely to transition into node 2 (13%) and unlikely to transition into a retraction (node 5), whereas node 5 is unlikely to transition into a poleward deflection (node 3) at longer timescales. Nodes 6-8 do not have any statistically significant probabilities, whereas retracted node 9 only has one significant low probability of transitioning into an extension (node 12). Node 10, however, has a 14% probability of transitioning into nodes 5 or 9, and is least likely to transition into nodes 2 and 8. Lastly, node 11 is most likely to extend into a pattern characterized by node 12, and least likely to transition into a retracted and poleward deflected regime denoted by node 1.

3.2.4. 20-Day Transitions

At longer 20-day timescales, most nodes still have at least one significant transition probability. Node 12 has the largest number of statistically significant probabilities, with one high probability of persistence or reoccurrence (13%) and two low probabilities of transitioning into

node 1 or node 4. Node 11 has the same significant probabilities as in day 15, wherein it is most likely to transition into node 12 (12%) and least likely to transition into node 1. The equatorward deflection denoted by node 10, however, no longer has any significant high probabilities; rather, there is only one unlikely transition into node 12. Interestingly, the retraction denoted by node 9 is most likely to transition into the extension denoted by node 8 at 20 days, whereas it is least likely to transition into node 1. This is the only preferred transition from a retracted state to an extended state throughout the 5- to 20-day period. However, this is not the case for the retracted node 5, in which there is only one statistically significant low probability of transitioning into node 7. As in lag 15, nodes 6-8 do not have any statistically significant probabilities. Lastly, the nodes featuring poleward deflections have preferred transitions into other poleward deflections at 20-days, with node 2 most likely to transition back into node 2 or persist (12%), node 3 most likely to transition into node 1 (12%), and node 4 most likely to transition into node 3 (14%).

3.2.5. NDJFM Preferred Transitions

The transition probabilities depicted in Fig. 3.1 demonstrate that transitions within the wintertime Pacific jet are not random; rather, there are transitions that are more likely and less likely to occur at short, medium, and extended timescales. Figure 3.2 illustrates the preferred transitions between nodes throughout the 5- to 20-day period. At short to medium 5- and 10-day transition times, almost every node has a tendency to persist. The increased likelihood for persistence is especially strong throughout the 20-day transition period for the extension depicted in node 12. This is to be expected, as node 12 is characterized by the longest mean residence time of all the nodes (Table 2.2) and exhibited a stronger correlation to teleconnection patterns like the PNA and ENSO. Also notable is that for timescales of 10-days and under, all preferred transitions occur into adjacent nodes, and very few nodes have preferred transitions into the weaker anomaly

states of nodes 6 and 7. Importantly, this suggests that relaxation towards a near-climatological state in such intervals is not a preferred tendency.

At medium timescales of 10-days, most of the preferred transitions occur into nodes featuring equatorward deflections (9-12). Fig. 3.2b illustrates a counterclockwise transition tendency through the SOM space, from a retracted state (node 5) into an extended state (node 12). However, by day 15, that tendency is no longer evident, with preferred transitions to the left in the SOM grid from node 10, and a preferred transition to the right from node 11 into 12. The node 11 to node 12 transition is a preferred tendency throughout shorter 5-day lags to longer 20-day lags. Another consistent preferred transition throughout the 5- to 20-day period is the poleward deflection extending into British Columbia (node 2) transitioning into node 1. The other poleward deflections evident along the top edge of the SOM grid exhibit varying preferred transitions with each lag. Interestingly, there are no preferred pathways to poleward deflected nodes 1-3 from retractions characterized by nodes 5 and 9, and at timescales of 10 days or less, there are no preferred pathways from extended nodes 4, 8, or 12. A transition from extended node 4 into a more canonical poleward deflection is not likely until timescales beyond 2 weeks.

Substantial anomaly shifts that occur from one edge of the SOM grid to another are not evident until longer timescales, wherein at 20-days, there is a preferred transition from the retracted jet pattern characterized by node 9 into an extension characterized by node 8. This preferred transition, taken with the counterclockwise transition tendency through the bottom of the SOM grid at shorter 5- and 10-day timescales, suggests that extensions (nodes 8 and 12) are likely to transition from equatorward deflections and/or retractions featuring an equatorward positive anomaly.

In focusing on unlikely transitions, the shorter 5-day to medium-range 10-day probability tables (Fig. 3.1a,b) illustrate that nodes depicting robust jet extensions (nodes 4, 8, 12) have at

least one reduced likelihood of transitioning into, or from, a retracted jet (nodes 5, 9). Similarly, retracted nodes are unlikely to transition into extensions over a 10-day period. This suggests that the more commonly studied transitions between an extended jet and retracted jet (e.g. Jaffe et al. 2019; Breeden and Martin 2018; Breeden and Martin 2019) are rare when compared to other transitions. Rather, it appears that strong extensions and retractions are more likely to transition into neighboring nodes.

Lastly, a look at the number of statistically significant conditional probabilities for each initial SOM node, both preferred and unlikely, at varying lags from 1-20 day lends insight into the theoretical predictability of the initial node. Figure 3.3 depicts the significant transitions as a function of lag, in which the black dashed line denotes the level of global significance (3). Most of the 12 nodes remain above the global significance line by lag 8, implying that they are theoretically predictable at weekly timescales. Weaker anomaly states 6 and 7 lose predictability at shorter lags than the other nodes, falling below the global significance line by lag 6. Equatorward deflected nodes 10 and 11 are the last to fall below the global significance, and both gain global significance at longer lags, along with poleward deflected node 2. Overall, there is general agreement between the theoretical predictability of the SOM nodes and the medium-range forecast errors associated with the Pacific jet leading modes of variability presented in Winters et al. (2019). In their analysis of forecast errors from GEFS forecasts initialized during an extension, retraction, poleward deflection, or equatorward deflection, it was found that the smallest forecast errors were initialized during jet extensions and poleward deflections. This is consistent with the higher theoretical predictability of SOM node 11 and 12 over the 8-11-day period. Furthermore, the largest medium-range GEFS forecast errors were initialized during jet retractions, consistent with a low theoretical predictability of SOM node 5 beyond 7 days.

3.3 December-February North Pacific Jet Transitions

The above analysis for wintertime north Pacific jet transitions is applied to a shorter wintertime season (December-February, DJF), as minor intraseasonal variability is evident in SOM node FOC, described in Chapter 2 (Fig. 2.7). Namely, November is characterized by a significantly lower FOC of node 12, marginally lower FOC of nodes 1 and 2, and a higher FOC of nodes 3, 4, and 6. Further, March is characterized by a larger FOC of nodes 1 and 5, and a lower FOC of node 3. Investigation of transitions over a shorter wintertime season will add insight into how sensitive preferred and unlikely transitions are to the definition of cold season.

3.3.1. 5-Day Transitions

The probability table for DJF transitions at short 5-day timescales (Fig. 3.4a) is largely similar to the NDJFM table (Fig 3.1a). Nodes 1, 4, 6, 7, 9, and 11 all have the same significant likely and unlikely transitions, with marginally different probability values. Nodes featuring retractions (1, 5, 9) all have the same unlikely transitions, whereas retracted node 5 has an additional preferred transition into node 10 (12%) at 5-days that was not evident in the longer cold season. The preferred transitions for node 8 remain the same (persistence and into nodes 4, 7 and 12) but there are additional significant reduced transitions into nodes 2 and 10. Node 12, however, is no longer characterized by a preferred transition into node 8 at 5-days and has an additional significant reduced probability into node 4. The only preferred 5-day transition for node 12 during DJF is persistence (36%) and into node 11 (15%). For poleward deflected nodes 2 and 3, node 2 has similar preferred transitions into 1 and 3 and an additional unlikely transition into node 5, whereas node 3 is no longer likely to persist or transition into 8; rather, it is likely to transition into nodes 2 and 4. Finally, equatorward deflected node 10 exhibits two additional unlikely transitions into nodes 5 and 1, whereas preferred transitions remain unchanged from the extended cold season.

3.3.2. 10-Day Transitions

At medium-range timescales, the only node with the same significant likely and unlikely transitions in both the longer NDJFM cold season and the DJF season is the retracted, equatorward deflected node 10 (Fig. 3.4b). However, many of the nodes exhibit only minor differences in preferred and unlikely transitions, losing or gaining statistical significance from only a 1-3% difference in likelihood percentages. For example, node 1 has equivalent preferred transitions to the extended cold season, and the additional unlikely transitions into nodes 11 and 12 are only ~1% less likely than the transitions in the NDJFM table. Retracted node 5 has flipped probabilities into nodes 9 and 10, with node 10 statistically significant during DJF as opposed to node 9 during the NDJFM cold season. However, both DJF and NDJFM tables identify extended node 12 as an unlikely transition at 10-days. For node 9, there is no longer a persistence signature at 10-days; however, it is still likely to transition into node 10 and unlikely to transition into an extension (node 8). Extended node 4 is more likely to transition into node 8 at 10-days during DJF, which could be due to a peak in node 8 FOC during December and January. As in the extended cold season, node 4 is unlikely to retract (node 9). Similarly, node 8 is unlikely to retract into a pattern characterized by node 5 in both 10-day transition tables. For equatorward deflected node 11, the most probable transition is still into extended node 12, whereas it is unlikely to transition into a retracted node 5 pattern. Lastly, DJF transition probabilities for node 12 illustrate a consistent enhanced likelihood of transitioning into node 7 (16%) or persisting, whereas it is still unlikely to retract into a pattern characterized by nodes 1 and 5.

3.3.3. 15- and 20- Day Transitions

At longer 15-day timescales (Fig. 3.4c), more substantial changes are noted in DJF preferred transitions. Beginning with nodes featuring retractions, node 5 has a significant likely

transition into a near climatological state (node 6, 16%), whereas node 9 is likely to transition into an extension (node 8, 16%). The transition from node 9 to 8 is a likely transition for NDJFM at 20-days, but it becomes a statistically significant preferred transition at shorter timescales for DJF. Node 9 is the only node with a preferred transition into extended node 8; however, both nodes 11 and 8 have a preferred transition into the extension denoted by node 12, whereas node 10 is unlikely to transition into poleward deflections characterized by nodes 1-3.

By 20 days, there are almost twice the number of DJF significant probabilities (Fig. 3.4d) as in the NDJFM cold season. The likely transitions that are consistent between the 20-day NDJFM table and DJF table occur between node 3 to 1, node 9 to 8, and node 11 to 12. Node 12 is still persistent at 20-days and is unlikely to transition into nodes 1 and 4. However, it is almost just as likely to transition into node 8 (14%) as it is to persist (15%). Extended and poleward deflected node 4 has an enhanced likelihood of transitioning into node 11 by 20-days, whereas it is unlikely to transition into a retraction (node 5).

3.3.4. DJF Preferred Transitions

A look at the preferred transitions for DJF (Figure 3.5) demonstrates that there is little change in preferred transitions at shorter 5-day timescales. By medium to longer timescales, however, the most notable differences occur between retractions and extensions. For example, the transition from a strong retraction denoted by node 9 into a strong extension denoted by node 8 occurs on shorter timescales during DJF than it does over the entire cold season. However, both NDJFM and DJF probability tables illustrate that the only preferred transition from a retraction to an extension occurs from node 9. Additionally, there are no instances of preferred transitions from extended states 4, 8, or 12 into retracted states 5 and 9 from shorter 5-day timescales to longer 3-

week timescales, suggesting that the north Pacific jet is more likely to transition from a retraction to an extension than it is from an extension to a retraction.

The theoretical predictability for initial nodes during DJF (Fig. 3.6) varies slightly from NDJFM. Although nodes 6 and 7 lose global significance before any other node, they are characterized by higher theoretical predictability during DJF by about 1 and 2 days, respectively. Similarly, most other nodes remain above the global significance line for 1 to 3 days longer than in NDJFM transitions. Nodes 10 and 12, in particular, remain theoretically predictable until lag 16. Also, retracted node 9 becomes predictable again by lag 18, which is not evident in the extended cold season global significance. Overall, comparison between the transition probability tables and global significance suggests that transitions and theoretical predictability are marginally sensitive to cold season definition, with nodes slightly more predictable during DJF than in the extended NDJFM cold season.

3.4 Summary and Discussion

The 12 SOM nodes established in Chapter 2 serve as initial state north Pacific jet patterns in which the temporal evolution is traced through the SOM space to characterize common and uncommon transitions. Transition probabilities are quantified through probability tables which indicate the conditional probability that the jet will reside within any SOM node after a specific time interval given the initial SOM node. The probability tables from shorter 5-day intervals to longer 20-day intervals demonstrate that there are preferred transitions that vary between 5-, 10-, 15-, and 20-day lags. At shorter 5-day transition times, most of the SOM nodes are more likely to persist than to transition into other nodes. By 10 days, persistence is still likely for many of the nodes, though most also exhibit statistically significant likelihoods of transitioning into nearby nodes, consistent with the transient behavior of the jet stream. By extended-range timescales of 15

days to 20 days, the persistence signature drops dramatically, as does the number of statistically significant transition probabilities into other nodes. However, the identified preferred transitions at longer 2-to-3-week timescales are not confined to adjacent nodes.

Investigation of transitions over a shorter DJF cold season reveals general agreement in the statistically significant likely and unlikely transitions, especially for shorter transition times of 5 and 10-days. Notable differences at 10-days include DJF preferred transitions from node 3 into nodes 1 and 2 and node 4 into 8; however, the absence of these statistically significant transitions during NDJFM could be tied to the lower FOC of nodes 1 and 2 in November and a lower FOC of node 8 in March (Fig. 2.7). Preferred transitions (excluding persistence/reoccurrence) that are identified in both the longer NDJFM and shorter DJF cold season probability tables include the transition from node 10 to 9, node 11 to 12, and node 12 to 7, all of which have probabilities exceeding 16%.

Directional transitions through the SOM space, indicated by high transition probabilities consistently in specific SOM nodes throughout the 5- to 20-day interval, can indicate predictable underlying dynamics driving preferred transitions. However, Figures 3.2 and 3.5 illustrate that only a few of the SOM nodes exhibit a consistent preferred transition. A counterclockwise NDJFM transition tendency through the SOM space (Fig. 3.2), from a retracted state (node 5) into an extended state (node 12) suggests that extensions characterized by node 12 are likely to develop from equatorward and/or retracted jet structures. This is supported by the consistent high transition likelihood from equatorward deflected node 11 to node 12 in both DJF and NDJFM cold seasons as well as over the entirety of the 5- to 20-day transition period. Additionally, the longer 15 and 20-day probability tables identify retracted node 9 into extended node 8 as a preferred transition,

whereas other nodes characterized by a retraction (nodes 1 and 5) do not tend to extend over longer timescales.

The preferred and unlikely transitions identified in this chapter further highlight the necessity of expanding wintertime Pacific jet variability into the SOM-identified 12 node grid. Distinct differences in transitions are noted from shorter 5-day timescales to longer 20-day timescales. Moreover, the theoretical predictability varies between SOM nodes as well. For example, although nodes 8 and 12 are both characterized by jet extensions, node 12 remains above the global significance line longer than node 8 over both NDJFM and DJF cold seasons. In Chapter 4, a composite analysis is performed on select 10-day preferred transitions that are consistent between the DJF and NDJFM analyses, as well as on a longer 15-day transition from a retraction (node 9) to an extension (node 8).

SOM Transition Probability Tables

(a) Lag 5 — Final Node

Original Node	1	2	3	4	5	6	7	8	9	10	11	12
1	23	16	11	11	12	11	7	3	4	2	0	1
2	13	24	15	9	7	10	10	5	2	3	1	0
3	9	10	15	16	5	10	13	14	2	1	3	2
4	7	9	12	23	6	9	9	16	2	4	2	2
5	11	5	9	6	24	10	5	4	15	9	2	0
6	9	11	11	4	9	17	15	4	5	9	6	1
7	6	7	6	7	3	13	18	14	2	8	8	8
8	3	4	7	15	3	4	17	24	2	3	3	14
9	7	3	3	3	20	9	4	2	28	15	5	1
10	4	4	2	1	8	14	8	2	9	29	14	4
11	2	4	3	3	2	8	17	6	3	11	24	18
12	0	2	2	6	4	8	12	14	2	5	12	32

(b) Lag 10 — Final Node

Original Node	1	2	3	4	5	6	7	8	9	10	11	12
1	17	9	8	8	11	12	8	7	7	6	3	3
2	12	16	11	12	10	8	10	9	2	4	3	2
3	10	10	11	13	7	9	16	9	3	4	4	4
4	8	12	12	16	6	8	10	12	3	3	5	3
5	11	5	8	5	14	10	8	9	14	10	4	2
6	7	10	8	8	11	13	9	10	8	9	6	2
7	6	6	6	6	9	11	16	10	4	10	9	9
8	4	5	10	12	5	7	12	17	5	6	6	10
9	8	4	7	8	13	9	7	4	13	15	8	4
10	7	6	3	3	9	13	9	7	16	15	7	6
11	4	4	7	8	3	4	10	8	5	10	17	20
12	3	6	5	9	4	10	16	9	3	3	10	20

(c) Lag 15 — Final Node

Original Node	1	2	3	4	5	6	7	8	9	10	11	12
1	11	9	6	9	11	11	10	8	6	8	7	4
2	14	11	13	6	10	8	12	10	5	4	3	3
3	10	11	11	8	11	9	13	8	6	4	5	5
4	10	13	10	14	4	8	8	11	4	4	7	7
5	9	9	4	8	10	13	8	8	10	8	8	5
6	8	7	7	10	9	12	11	9	8	9	7	4
7	7	5	5	11	9	10	14	8	7	7	8	8
8	7	8	9	12	6	8	14	11	6	5	6	9
9	8	4	10	14	12	8	8	12	4	9	7	2
10	5	3	4	8	14	13	13	4	14	10	7	5
11	3	4	5	10	7	13	11	7	6	10	10	13
12	5	6	7	7	7	8	9	10	8	6	8	21

(d) Lag 20 — Final Node

Original Node	1	2	3	4	5	6	7	8	9	10	11	12
1	8	9	10	12	9	10	6	9	9	8	4	5
2	10	12	13	9	12	11	8	6	6	5	3	5
3	12	9	10	7	8	12	11	6	7	9	6	4
4	9	8	14	12	5	8	11	9	5	3	9	7
5	11	7	7	8	11	10	6	8	6	9	10	7
6	7	7	10	8	10	10	11	7	7	10	7	5
7	8	7	6	7	8	10	14	10	9	6	5	9
8	8	10	6	12	6	7	13	9	11	6	9	5
9	3	5	11	13	6	11	10	16	6	6	6	7
10	9	6	7	7	13	13	8	9	8	10	7	3
11	3	8	5	7	6	10	14	12	8	7	9	12
12	4	6	6	4	11	7	14	12	8	8	7	13

Figure 3.1: 5 through 20-day anomalous transition probabilities for SOM Nodes 1-12 observed in the NCEP Reanalysis data. Within each subplot, columns 1-12 correspond to the SOM Node into which the transition is observed and rows 1-12 correspond to the node at the start of the transition. Red (blue) squares indicate enhanced (reduced) transition frequency at the 95% significance level.

NDJFM Preferred Transitions

(a) Lag 5

(b) Lag 10

(c) Lag 15

(d) Lag 20
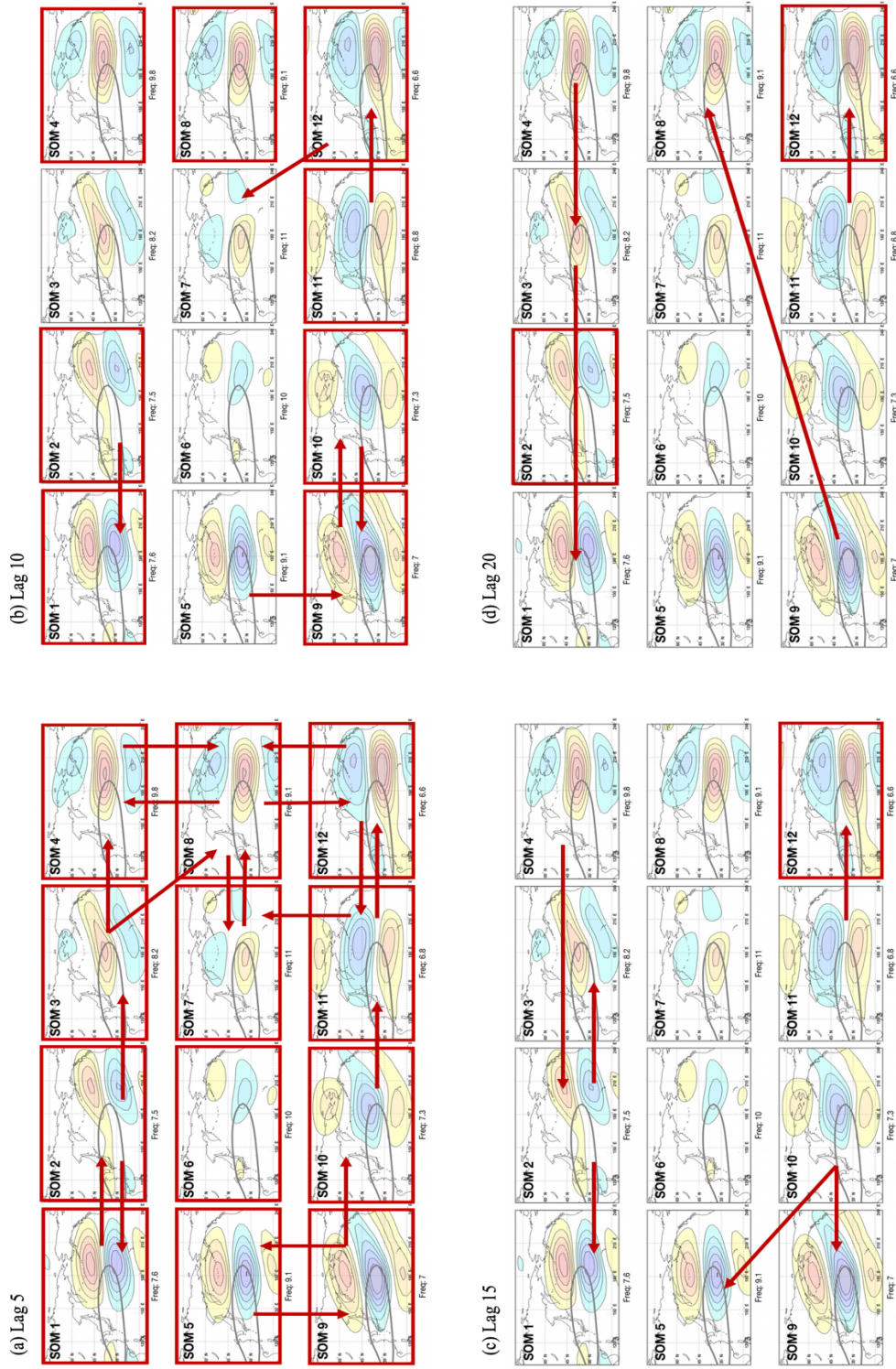
Figure 3.2: Schematic of statistically significant preferred transitions identified in the probability tables at lags (a) 5, (b) 10, (c) 15, and (d) 20 (Fig. 3.1). Red boxes indicate a preferred tendency to remain in the initial node, and red arrows point towards a preferred transition from the initial node into the final node at the corresponding lag.
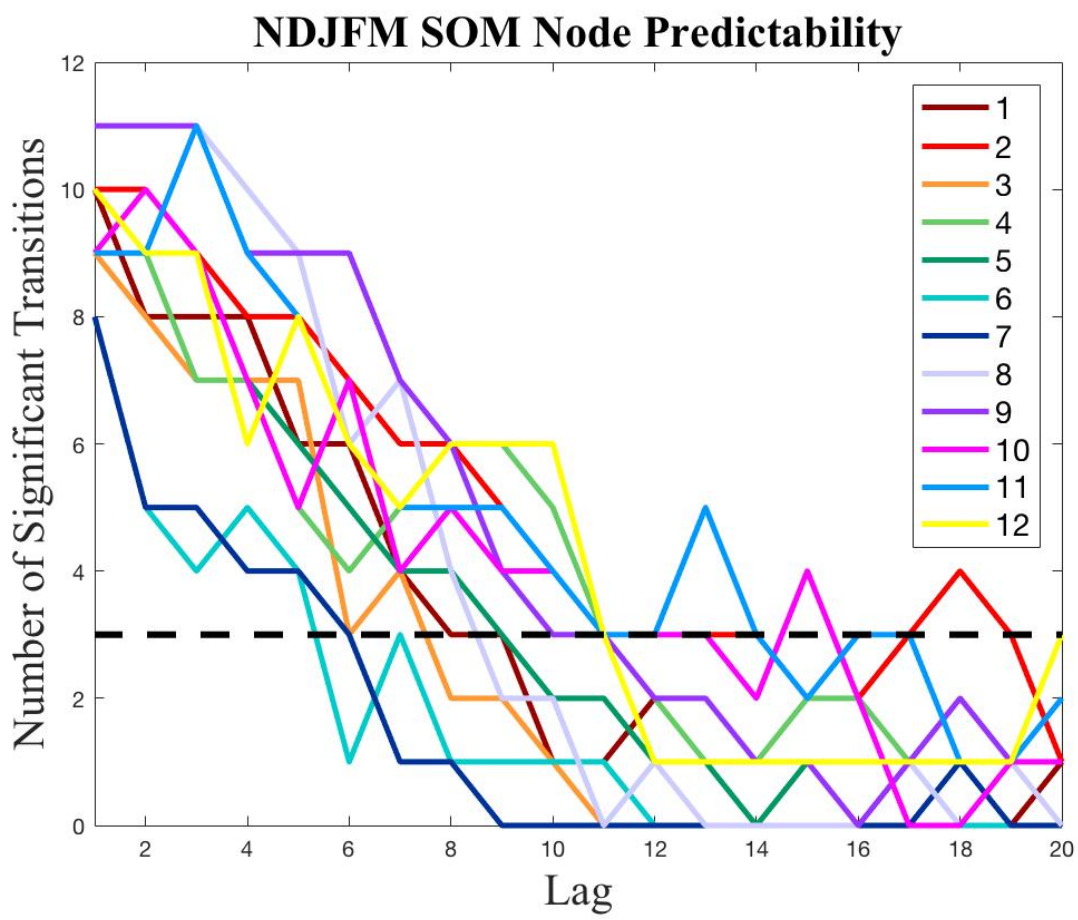
Figure 3.3 Number of statistically significant NDJFM conditional probabilities for the initial SOM node between lags 1 to 20. Global significance, determined from the Livezey-Chen method, is indicated by the black dashed line (3).

DJF SOM Transition Probability Tables

(a) Lag 5 — *Final Node*

Original Node	1	2	3	4	5	6	7	8	9	10	11	12
1	26	17	11	11	11	11	5	1	4	1	0	1
2	14	26	16	9	4	10	11	6	2	2	1	0
3	10	12	12	16	8	11	12	10	2	2	2	3
4	9	9	11	24	5	7	8	18	2	3	1	2
5	12	7	9	7	21	9	5	3	14	12	2	0
6	8	9	10	4	8	21	13	4	4	9	9	1
7	6	8	5	7	3	11	16	15	2	8	8	10
8	3	3	5	15	4	4	19	26	2	3	2	16
9	8	2	2	4	20	7	1	3	27	18	6	1
10	4	4	2	1	5	12	7	2	9	28	19	6
11	1	4	3	3	3	10	16	7	3	11	20	21
12	0	1	2	4	4	8	11	12	3	5	15	36

(b) Lag 10 — *Final Node*

Original Node	1	2	3	4	5	6	7	8	9	10	11	12
1	18	9	8	9	10	13	7	8	8	6	2	3
2	12	18	11	13	9	8	9	9	3	6	2	2
3	14	13	10	12	8	8	14	7	3	4	3	4
4	9	10	13	15	5	9	8	15	3	3	4	4
5	12	3	6	7	14	11	8	8	10	14	4	3
6	4	10	7	7	13	16	8	8	8	10	7	1
7	6	7	6	6	8	10	12	12	3	10	9	11
8	5	4	10	12	4	6	11	20	5	5	6	12
9	11	3	7	7	12	7	10	3	10	16	7	6
10	6	4	3	2	6	13	8	10	19	13	8	9
11	4	5	6	9	1	6	12	9	5	9	16	19
12	3	5	6	10	2	8	16	6	4	4	12	23

(c) Lag 15 — *Final Node*

Original Node	1	2	3	4	5	6	7	8	9	10	11	12
1	10	8	7	10	14	8	10	9	6	9	5	2
2	13	12	14	6	8	8	11	11	6	4	4	2
3	13	14	13	8	10	6	8	9	6	4	4	5
4	11	12	8	14	4	8	6	11	2	5	8	11
5	10	10	6	5	10	16	7	8	5	8	7	8
6	8	5	7	9	11	15	6	6	9	13	7	4
7	7	6	5	10	9	10	14	9	7	6	9	8
8	7	8	6	14	5	9	12	10	7	4	5	12
9	10	7	10	11	9	8	8	16	4	9	5	4
10	4	3	3	8	12	10	15	7	17	11	7	4
11	4	5	4	9	8	16	8	8	7	10	10	12
12	4	4	6	9	5	6	6	9	9	7	11	25

(d) Lag 20 — *Final Node*

Original Node	1	2	3	4	5	6	7	8	9	10	11	12
1	8	8	12	15	10	9	5	9	12	6	4	5
2	11	11	13	9	13	14	5	5	6	5	3	6
3	15	10	10	7	7	10	9	4	8	7	5	5
4	8	8	12	11	3	7	13	8	5	4	12	9
5	11	8	10	10	6	12	5	12	5	7	6	8
6	7	7	8	8	11	9	10	8	8	10	7	5
7	9	6	4	7	7	9	15	11	9	5	6	11
8	9	10	6	12	6	7	12	9	10	5	8	6
9	3	7	11	15	4	10	7	17	4	7	8	8
10	8	6	8	5	15	10	10	10	6	10	8	3
11	3	11	7	11	4	8	11	9	6	6	12	11
12	4	4	5	3	9	6	14	14	7	9	9	15

Figure 3.4 As in Fig. 3.1 but for DJF months only.

DJF Preferred Transitions
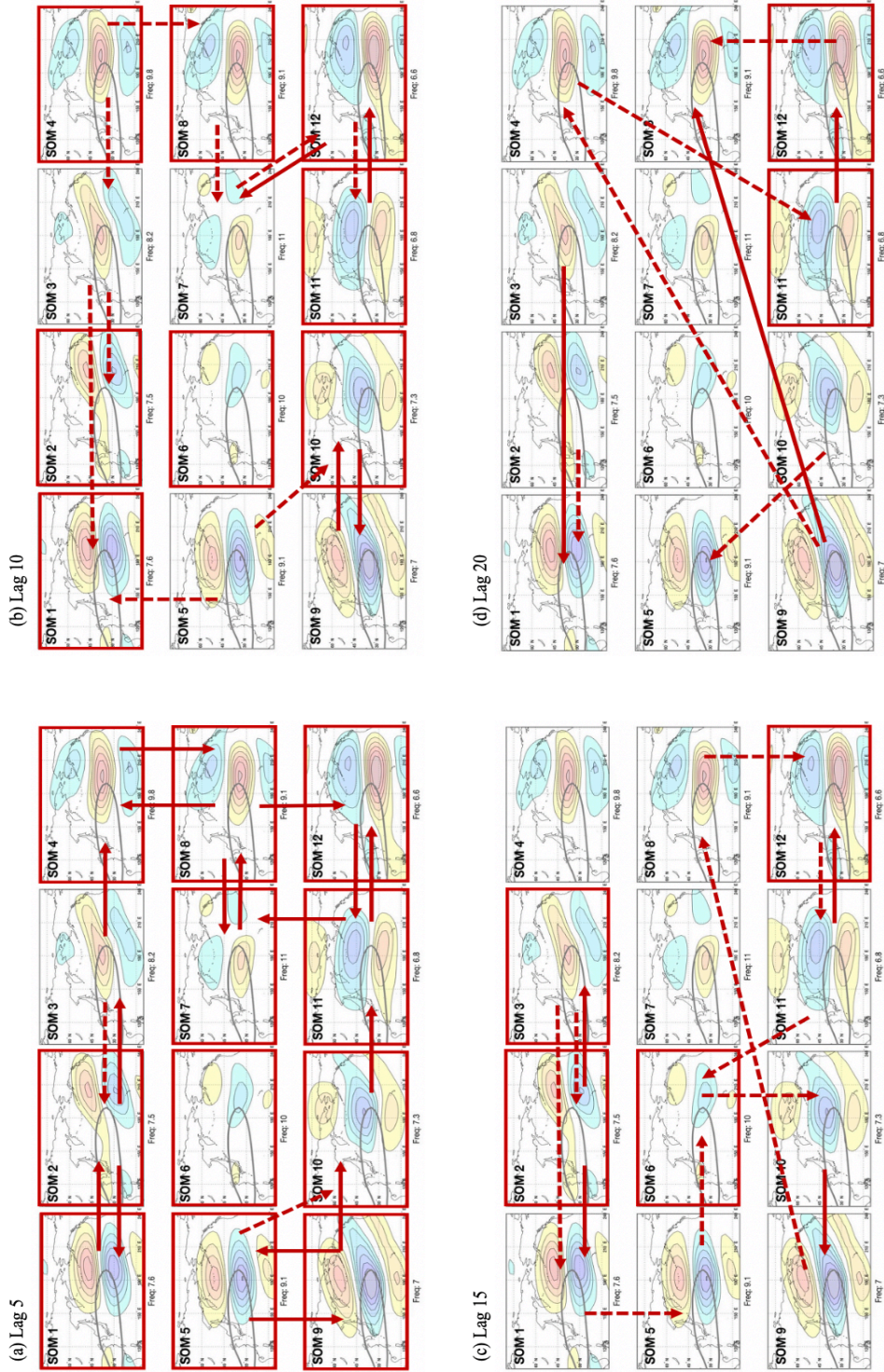
Figure 3.5: As in Fig. 3.2 but for DJF preferred transitions. Dashed arrows indicate a preferred transition not evident in NDJFM transition tables.
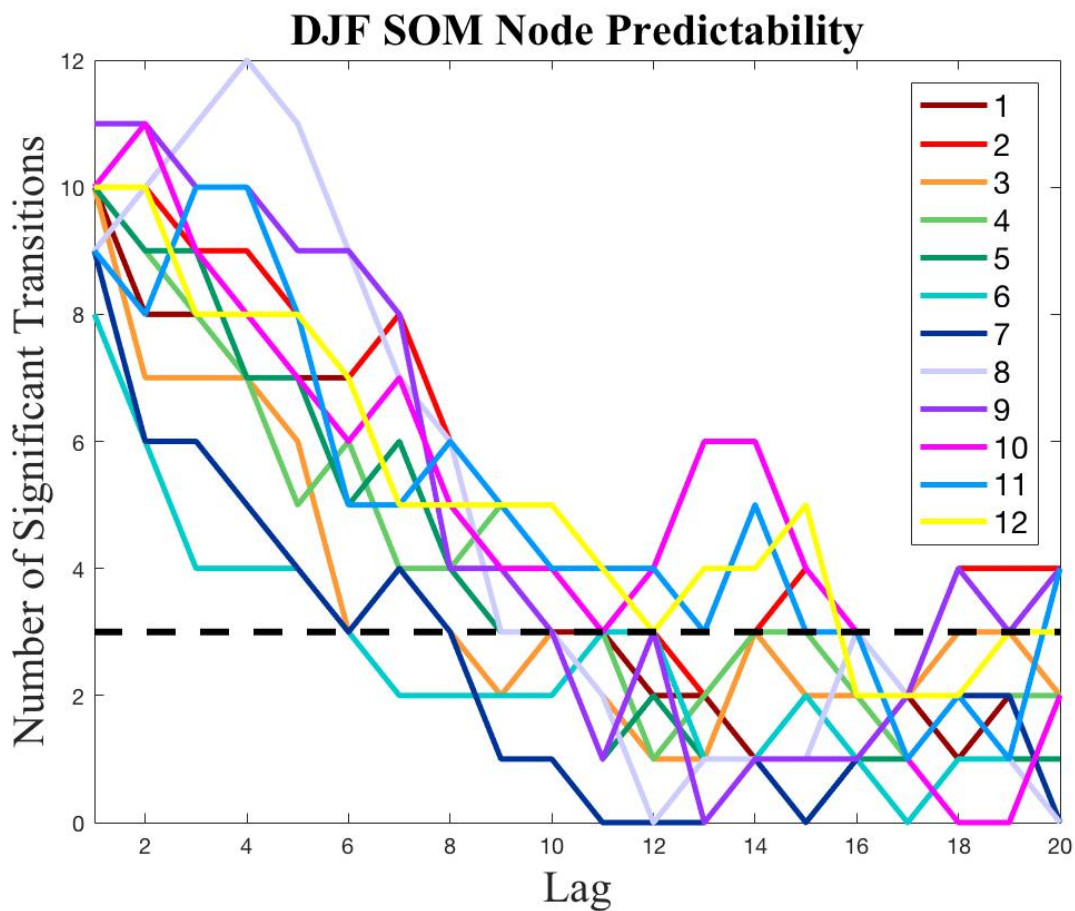
Figure 3.6: As in Fig. 3.3 but for DJF conditional probabilities.

CHAPTER 4: SYNOPTIC SCALE CIRCULATION AND DOWNSTREAM IMPACTS OF PREFERRED TRANSITIONS

4.1 Data and Methods

To illustrate the evolution of the synoptic scale environments associated with preferred Pacific jet transitions, a composite analysis for medium-range 10-day preferred transitions as well as a longer 15-day transition is performed. The selection of 10-day transition timescales provides a basis for comparison to prior research focused on EOF/TE-EOF analysis of characteristic environments of jet variability on medium-range timescales (e.g. Jaffe et al. 2011; Griffin and Martin 2017; Winters et al. 2019). Additionally, the 15-day DJF preferred transition from a retracted node 9 to an extended node 8 is composited, as it is the only preferred transition between nodes of nearly opposite anomaly patterns.

Composites are constructed with days that are contained within a single season between the years of 1979-2019. Transition events are identified by selecting days characterized by the initial node transitioning into the final node of interest at 10 days or 15 days later. The last day in a series of days is designated as the beginning of the transition event (Day 0). For example, if a 10-day transition from node 11 to node 12 begins on December 1, 2, and 3, December 3 is identified as Day 0 of the event. Each transition composite is then averaged with respect to Day 0. The transition evolution is depicted every 5 days over a time period of 5 days prior to the start of the transition (Day -5) to the end of the transition event (Day 10/Day 15). Anomalous quantities of NCEP/NCAR reanalysis 200 hPa stream function, 850 hPa stream function, 850 hPa temperature, and 250 hPa zonal winds are calculated by subtracting out a 21-day running mean seasonal cycle and long-term mean and are analyzed to characterize regional circulation changes and downstream impacts of different preferred pathways. Additionally, anomalies of outgoing longwave radiation (OLR) from

the NOAA Interpolated OLR dataset (Liebmann and Smith 1996) are computed by the same method described for the other atmospheric variables and serve as a proxy for tropical/subtropical convection and cloud cover. The inclusion of OLR will allow for comparison between extratropical and tropical processes involved in Pacific jet transitions. A two-tailed Student's t test is applied to determine statistically significant features at the 95% confidence level.

4.2 10-Day Transition Composites

Analysis of 10-day transitions for the extended NDJFM and shorter DJF cold season reveals that most nodes have a tendency to persist; however, many nodes exhibit at least one statistically significant transition into another node. Of these preferred transitions, the transition from equatorward deflected node 11 into a more extended node 12 has the highest likelihood of occurrence - 20% during NDJFM and 19% during DJF. The transition from node 12 into a weaker state characterized by a slight jet enhancement (node 7) is also amongst the highest likelihoods, with a 16% likelihood of occurrence for both cold season definitions. Lastly, the transition from node 10 into a stronger retraction characterized by node 9 is a robust preferred transition in both NDJFM and DJF, with a 16% transition likelihood during NDJFM and an enhanced 19% likelihood during DJF. The following 10-day transition composite analysis will focus on these three transitions, as they exhibit the highest likelihoods and are statistically significant preferred transitions in both NDJFM and DJF cold seasons.

4.2.1. Node 11 to Node 12 Transition

The 10-day transition of equatorward deflected node 11 into node 12 is shown in Figure 4.1, with the evolution of 250-hPa zonal wind anomalies from Day -5 to Day 10 illustrated in Fig. 4.1a-d. Five days prior to the transition, the jet is deflected equatorward, with positive zonal wind anomalies between 4-12 ms^{-1} south of the climatological jet stream (Fig. 4.1a). The upper level

stream function field on Day -5 is characterized by an anomalous upper-level low centered over the climatological jet exit region and a weaker anomalous upper-level high stretching between eastern Russia and Alaska (Fig. 4.1a). By Day 0, the jet strengthens, and is still characterized by anomalies south of the climatological $40 \, ms^{-1}$ isotach (Fig. 4.1b). Negative anomalies to the north also strengthen by $4 \, ms^{-1}$, supported by a strengthening of the 200 hPa positive and negative stream function anomalies on the cyclonic shear side of the jet stream (Fig. 4.1b). Five days into the transition, the jet extends further east by 5-10°, strengthens by $4 \, ms^{-1}$, and deflects poleward 5° (Fig. 4.1c). The strengthening is associated with a rapid enhancement of the upper-level high equatorward of the jet stream that connects to another high over the Pacific Northwest. A weaker negative anomaly is situated over southeastern U.S. The upper level stream function anomalies on Day 5 bear a strong resemblance to a positive PNA pattern (Wallace and Gutzler 1981). By Day 10, in which the jet is characterized by node 12, the jet exit region defects another 5° north, with positive anomalies between 4-20 ms^{-1} stretching equatorward from the climatological wintertime jet position (Fig. 4.1d). The circumambient stream function anomalies tilt northeastward between Day 5 and 10, in accord with the 5° poleward jet deflection.

Closer to the surface, Day -5 is characterized by a weak negative 850 hPa stream function anomaly near 30°N and 165°W, whereas another weaker positive anomaly sits over southeast Alaska (Fig. 4.1 e). Warm 850 hPa temperature anomalies are evident over far eastern Russia into the Bering and Chukchi Seas, and stronger cold 850 hPa temperature anomalies stretch over central Canada. On Day 0 (node 11), the 850 hPa low strengthens over the central Pacific, while negative temperature anomalies spread over far eastern and western Canada and into Alaska. Another area of negative temperature anomalies is evident over the western edge of the low, whereas the warm anomalies retrogress over Russia (Fig. 4.1f). By Day 5, the low over the central Pacific strengthens

further, and negative 850 hPa temperature anomalies over Canada are replaced with positive anomalies over the US west coast (Fig. 4.1g). The final day of the transition (Day 10) is characterized by a weakened 850 hPa low and weak 850 hPa negative temperature anomalies on the western periphery of the low as well as over Mongolia (Fig. 4.1h).

OLR anomalies characterizing the transition from node 11 to 12 are illustrated in Fig 4.1i-l. Negative (positive) anomalies correspond to enhanced (suppressed) convection. In the 5 days prior to the transition, an area of negative OLR anomalies is evident over the tropical west Pacific indicating anomalous convection, with three smaller areas of positive OLR anomalies just east of the dateline, near 220°E, and near 240°E (Fig. 4.1i). The negative anomalies over the Maritime Continent marginally strengthen by Day 0, and another region of negative OLR anomalies organizes near 30°N over the east Pacific (Fig. 4.1j). By Day 5, an area of suppressed convection is evident equatorward of the jet. The location of the suppressed convection is consistent with the TE-EOF 1+ OLR composites from Griffin and Martin (2017). Between Day 5 and Day 10, the OLR anomaly appears quasi-stationary, while OLR anomalies over the Indian Ocean dissipate (Fig. 4.1 l).

While the OLR anomalies do not seem to be associated with a propagating MJO feature over the 15 days, the distribution of enhanced convection on Day -5 and Day 0 resembles the OLR anomalies leading to positive PNA events (Franzke et al. 2011, their Fig. 11). As such, the semi-persistent negative OLR anomaly on Day -5 and Day 0 might serve as a forcing for an excitation of a positive PNA-like pattern and a transition into node 12. This is consistent with the strengthening of the upper-level anticyclonic stream function anomalies observed on Day 5 and 10, wherein convective outflow associated with the anomalous tropical convection can propagate northeastward and lead to the observed poleward deflection and extension of the jet exit region.

4.2.2. Node 12 to Node 7 Transition

The transition from extended node 12 to node 7 is illustrated in Figure 4.2. Five days prior to the transition, the jet is already extended, with 4-16 ms^{-1} 250 hPa zonal wind anomalies near the climatological jet exit region that dip equatorward east of the dateline (Fig. 4.2a). An upper-level negative (positive) stream function anomaly is north (south) of the jet exit region, and another region of negative stream function anomalies is evident over east Asia and southeast U.S. (Fig. 4.2a). Over the following 5 days, the jet strengthens and deflects 5° poleward over the central Pacific, while the upper-level stream function anomalies strengthen as well, forming a meridional dipole north and south of the Pacific jet (Fig. 4.2b). A PNA-like teleconnection pattern is evident at Day 0, consistent with the high correlation between node 12 FOC and positive PNA events (Ch. 2, Fig. 2.10). By Day 5, the jet weakens by 12 ms^{-1} in association with a weakening of the stream function anomalies (Fig. 4.2c). However, by Day 10, the positive stream function anomaly on the anticyclonic shear side of the jet becomes isotropic, while the negative anomaly north of the jet exit region diminishes almost entirely (Fig. 4.2c). The isotropic stream function anomaly supports the observed poleward deflection of the jet into a pattern characterized by an enhanced jet exit region (node 7).

At 850 hPa, a negative stream function anomaly over the central Pacific, indicative of a low-level low, strengthens between Day -5 and Day 0 (Fig. 4.2 e,f). Low-level cold air anomalies expand from -2°K over the midwestern and southeastern US on Day -5 (Fig. 4.2e) to -2°-4°K over the entirety of eastern North America on Day 0 (Fig. 4.2f). A small area of warm anomalies is observed off the coast of the Pacific Northwest, while another area of cold anomalies stretches east from the center of the low, consistent with temperature anomalies associated with a positive PNA teleconnection pattern. Five days later, the low over the central Pacific substantially diminishes,

and 850 hPa temperature anomalies are confined to northeastern North America and the Sea of Japan (Fig. 4.2g). By the end of the transition into node 7 (Fig. 4.2h), the weak negative 850 hPa stream function anomaly shifts westward, while small areas of 2°K temperature anomalies are evident over the eastern U.S., the southern edge of the Beaufort Sea, and west of the dateline beneath the jet exit region.

The OLR anomalies associated with the transition from node 12 to 7 depict propagating regions of suppressed and enhanced convection (Fig. 4.2 i-l). On Day -5, two regions of enhanced convection are observed- one over the tropical Pacific near the dateline and another at 30°N over the eastern Pacific (Fig. 4.2i). Regions of positive OLR anomalies are located in the subtropical Pacific between the areas of enhanced convection as well as over the eastern Indian Ocean. By Day 0, both positive OLR anomalies appear to move eastward and strengthen, while the negative OLR anomalies begin to dissipate (Fig. 4.2j). Day 5 of the transition is characterized by a weakening of the OLR anomalies and disorganized areas of positive anomalies over the subtropical Pacific. By Day 10, small regions of enhanced convection appear over the Indian Ocean and over the central north Pacific, while areas of suppressed convection remain scattered over the subtropical Pacific basin (Fig. 4.2l).

Overall, there appears to be an eastward progression of OLR anomalies over the 15 days with a phase speed consistent with convection associated with the MJO (Madden and Julian 1972; Zhang 2005). This suggests that the onset of extended node 12 is tied to the later phases of the MJO, which is consistent with the analysis of anomalous FOC following MJO phases discussed in Chapter 2. The transition from node 12 to 7, however, is likely associated with a progression from the later phases of the MJO (MJO phases 7-8) with enhanced convection over the Pacific and suppressed convection over the Indian Ocean, to early MJO phases (phase 1-2), with enhanced

convection forming over the Indian Ocean. Although significant changes in node 7 FOC were not evident in early MJO phases (Figs. 2.11-2.13), only strong MJO phases were considered in the prior analysis.

4.2.3. Node 10 to Node 9 Transition

The evolution of the 10-day preferred transition from node 10 to node 9 is depicted in Figure 4.3. In the 5 days prior to the start of the transition, there are weak negative zonal wind anomalies near the climatological left jet exit region and weak 4 ms^{-1} positive anomalies over the Chukchi and Bering Seas as well over southern Russia (Fig. 4.3a). The 200 hPa stream function anomalies depict an upper-level low near the jet-exit region, and a weak high over the Aleutian Islands. Another small upper-level low is observed over the subtropical eastern Pacific. On Day 0, which is characterized by node 10, stream function anomalies strengthen over the Pacific, and the subtropical low from Day -5 shifts northeast into Canada. The upper-level stream function pattern resembles a negative PNA-like teleconnection pattern, which is unsurprising due to the observed tripling of node 10 FOC during negative PNA events (Ch. 2, Fig. 2.10). Also notable is the lack of equatorward zonal wind anomalies on Day 0, which is unexpected given the composite SOM node 10 anomaly pattern (Ch. 2, Fig. 2.3). By Day 5, the upper-level stream function anomalies straddling the negative zonal wind anomalies strengthen further and shift south (Fig. 4.2c). Accordingly, the negative zonal wind anomalies shift south, residing nearly precisely along the climatological jet exit region. Zonal wind anomalies on the northern periphery of the upper-level high also strengthen and expand. The last day of the transition from 10 to 9 is characterized by the strongest negative zonal wind anomalies in the climatological jet exit region with a meridionally oriented dipole in stream function anomalies. The upper-level low is more isotropic, while the high over the North Pacific marginally flattens. By Day 10, there is another weak upper-level negative

anomaly downstream of the dipole, a stronger positive anomaly over Baja California, and another positive anomaly near the Caribbean Sea (Fig. 4.3d).

Near the surface, an 850 hPa positive stream function anomaly is situated over the Aleutian Chain on Day -5, with anomalously warm air on its eastern edge and over eastern Asia (Fig. 4.3e). Over the next 5 days, the 850 hPa low remains nearly static, while the anomalously warm air spreads over the northwestern boundary of the Pacific basin, and anomalous cold air appears over western Canada (Fig. 4.3f). On Day 5, the positive stream function anomaly strengthens, and another weak negative stream function anomaly develops equatorward of it (Fig. 4.3g), both exhibiting an equivalent barotropic structure with the upper-level stream function anomalies (Fig. 4.3c). Minor shifts in the extent of warm and cold air anomalies are also evident on Day 5. Between Day 5 and 10, there are minimal changes to the low-level circulation and temperature structure.

OLR anomalies associated with the transition from 10 to 9 exhibit a disorganized structure between Day -5 and 0 (Fig. 4.3i,j). However, by Day 5, there is a region of negative OLR anomalies over the central Pacific, indicative of enhanced convection (Fig. 4.3k). This region of enhanced convection grows between Day 5 and 10, and another region of enhanced convection develops south of India (Fig. 4.3l). Additionally, three regions of positive OLR anomalies are observed by Day 10 - the strongest one over the tropical central Pacific, another south of the Aleutian Islands, and a third near Madagascar (Fig. 4.3l). The OLR anomalies on Day 5 and 10 resemble the composite OLR of jet retractions from Jaffe et al. (2011) (their Fig. 12). As mentioned in their analysis, as well as in Otkin and Martin (2004b), the region of negative OLR anomalies over the central Pacific is likely tied to the altered storm-track activity associated with jet retractions. Retractions are associated with enhanced storm-track activity over the central Pacific, which would lead to enhanced convection and negative OLR anomalies observed in the Day 5 and 10

composites (Otkin and Martin 2004; Jaffe et al. 2011). The positive OLR anomaly over the tropical Pacific is also evident in the Jaffe et al (2011) retraction composites; however, it is of much stronger magnitude in this analysis and could reflect a weakened Hadley cell that might aid in the initiation of the node 10 to 11 transition.

4.3 15-Day Transition Composite

Composites of the 10-day preferred transitions demonstrate that while distinct circulation changes are associated with the transitions, the transitions all occur into neighboring SOM nodes. It isn't until longer timescales beyond two weeks that a statistically significant preferred transition into a nearly opposite node is evident. In both the NDJFM and DJF probability tables, the transition from retracted node 9 to extended node 8 is identified as a preferred transition. However, the preferred transition becomes statistically significant at shorter 15-day timescales during DJF (16%) as opposed 20-day timescales during the extended NDJFM cold season (16%). The proceeding composite analysis will focus on 15-day transitions between node 9 and 8 in order to compare this evolution (from a retraction to an extension) to previously studied rapid jet retraction events.

4.3.1. Node 9 to Node 8 Transition

The 15-day transition from node 9 to 8, analyzed from 5 days prior to the start of the transition (Day-5) to the last day of the transition (Day 15) is illustrated in Figure 4.4. On Day -5, a jet retraction is clearly evident, with negative zonal wind anomalies in the climatological jet exit region and positive anomalies poleward and equatorward (Fig. 4.4a). Stream function anomalies at 200 hPa show an upper-level low east of the dateline and south of the negative zonal wind anomalies, whereas an upper-level high stretches over the Aleutian Islands. By Day 0, the retraction intensifies in both magnitude and latitudinal extent. Positive zonal wind anomalies to the north and south also intensify, with the mid-latitude (subtropical) zonal wind anomaly

stretching across the northern (southern) periphery of a strengthened upper-level high (low) (Fig. 4.4b). Between Day 0 and 5, a rapid decay of upper-level zonal wind and stream function anomalies occurs (Fig 4.4c). Only a weak anticyclonic anomaly is observed over the climatological jet exit region, whereas the strong cyclonic anomaly on Day 0 splits into two smaller anomalies over the east Pacific and subtropical Pacific by Day 5. On the southern edge of the eastern Pacific cyclonic anomaly, an enhanced region of zonal winds between 4-8 ms^{-1} remains. Five days later, the upper-level cyclonic anomaly over the east Pacific advances north and becomes isotropic, whereas the weak anticyclonic anomaly migrates south and weakens (Fig. 4.4d). Consistent with the northward shift of the upper-level low, the positive zonal wind anomalies shift northeastward by Day 10. By Day 15, the upper-level low retrogresses and expands zonally, and the upper-level high strengthens and shifts eastward, creating a meridional dipole in stream function anomalies (Fig. 4.4e). The dipole in upper-level anomalies supports enhanced westerlies near the jet exit region and thus an extension of the Pacific jet. Additionally, a weak anticyclonic anomaly initially observed over the subtropical eastern Pacific on Day 10 shifts northeast over Canada by Day 15. By the end of the transition, the upper level synoptic-scale wave pattern resembles a positive PNA teleconnection pattern.

At 850 hPa, Day -5 is characterized by a weak positive stream function anomaly centered south of the Aleutian Islands and a weak -4 K temperature anomaly over Alberta (Fig. 4.4f). By Day 0, the stream function anomaly strengthens, with warm air anomalies extending from the center of the 850 hPa high towards Japan (Fig. 4.4g). Smaller areas of cold air anomalies are evident over Russia as well. Five days into the transition, the 850 hPa anomalies dissipate, and by Day 10, a weak negative stream function anomaly develops south of Alaska (Fig. 4.4 h,i). Over the following

5 days, the 850 hPa low marginally strengthens, and weak 2°K warm air anomalies develop over northwestern Canada and eastern Alaska (Fig. 4.4j).

The characteristic OLR anomalies associated with a transition from node 9 to 8 are depicted in Figure 4.4k-o. In the five days prior to the initial transition, negative OLR anomalies are evident over the central subtropical Pacific basin, likely associated with the anomalous low-level trough (Fig. 4.4k,g). An area of positive OLR anomalies is situated in the tropical Pacific near the dateline, whereas more disorganized areas of positive OLR anomalies are scattered over the western subtropical Pacific (Fig. 4.4k). On Day 0, the negative subtropical OLR anomalies expand and strengthen, and an area of positive OLR anomalies develops north of the enhanced convection whereas another area organizes west of the enhanced convection (Fig. 4.4l). Five days later, the area of enhanced convection weakens and shifts northeastward, whereas the two areas of positive OLR anomalies largely dissipate (Fig 4.4m). On Day 10 of the transition, enhanced convection is observed near the dateline, and positive OLR anomalies develop over the southern Indian Ocean (Fig. 4.4n). By Day 15, larger regions of suppressed convection are evident over the Indian Ocean and in the subtropical eastern Pacific (Fig. 4.4o).

The role of OLR anomalies in the transition from a retraction to extension is not immediately apparent. While areas of enhanced and suppressed convection are evident in the days prior to the transition, the location and evolution of the anomalies do not suggest a clear forcing for the transition, but may represent a manifestation of the shifted storm track associated with retraction events (e.g. Jaffe et al. 2011; Otkin and Martin 2004b). Composites of stream function, however, demonstrate that the transition is associated with a reversal in upper- and lower-level anomalies and the onset of a weak positive PNA-like pattern with weak to negligible low-level temperature anomalies.

4.4 Summary and Discussion

Composite analysis comparing preferred transitions between various SOM identified jet regimes at 10- and 15-day timescales demonstrates that there are distinct differences in the synoptic scale circulation and impacts associated with the transitions. Even with subtle transitions of the jet, there are widespread and sometimes strong 850 hPa temperature and low-level stream function anomalies that develop over 5 to 20 days. Consistent with prior research on leading modes of wintertime Pacific jet variability (e.g. Jaffe et al. 2011; Griffin et al. 2017, Breeden and Martin 2018), the composite structure characterizing transitions from or into retractions (extensions) exhibit a strong anticyclonic (cyclonic) anomaly over the north Pacific basin. The downstream temperature anomalies resemble the composite TEEOF/EOF 1 analyses in Griffin et al. (2017) and Winters et al. (2019a), with cold anomalies over the western/northwestern part of North America and warm anomalies over the Pacific basin on Day 0 of the transition from node 10 to 9. However, Day 0 is characterized by node 10, and throughout the transition to a jet structure characterized by a stronger retraction (node 9), the circulation over the Pacific and North America shifts, subsequently shifting the magnitude and extent of low-level temperature anomalies. Thus, the shifting of the jet retraction has consequences on the downstream impacts.

Similarly, the transitions between nodes 11 and 12 and nodes 12 and 7 exhibit synoptic scale anomalies that are consistent with prior composite analyses on at least one day of the transition, but a meridional or latitudinal shift in the jet exit region is associated with changes in the synoptic scale circulation, downstream impacts, and tropical convection. For example, the transition from node 11 to node 12 is associated with cooler 850 hPa temperatures over Canada and enhanced convection over the Maritime continent on Day 0, whereas Day 10 is characterized by only a small area of cool temperatures over eastern Canada and a larger region of suppressed convection over

the subtropical Pacific. Depiction of nodes 11 and 12 in the two-dimensional EOF-phase space from Chapter 2 (Fig. 2.6), however, suggest that the nodes are fairly similar, with days in both nodes clustering in the bottom right quadrant of the phase space. The composite evolution of synoptic-scale features and downstream impacts highlight the importance of more carefully distinguishing between jet regimes, as these features likely have their origin in characteristic tropical and extratropical interactions.

Subtleties of the SOM nodes and transitions between them may also help to advance understanding of the impact of Pacific jet variability on medium range forecasts skill through an application of the SOM-based analysis presented in this study to the examination recently undertaken by Winters et al. (2019b). In comparing the best to the worst GEFS medium-range forecasts initialized during the four EOF/PC-identified North Pacific jet regimes, Winters et al. (2019b) revealed that there were key differences in the synoptic-scale structure within each regime. For example, for forecasts initialized during an extended regime, the worst forecasts emerged from a synoptic-scale environment characterized by higher geopotential height anomalies over the eastern north Pacific and North America (Winters et al. 2019b, their Fig. 12b), which resembles the synoptic scale environment of SOM node 8 and a positive PNA-like structure (Ch. 2, Fig. 2.4), whereas the best forecasts emerged from an environment more characteristic of SOM node 12 (Winters et al. 2019b, their Fig. 12a). Comparison of nodes 8 and 12 in the global significance theoretical predictability (Ch. 3, Figs 3.3 and 3.6) reveals that beyond lag 5, node 12 is theoretically more predictable than node 8 until lag 11, wherein it falls below the global significance line. This suggests that subtle 5-10° latitudinal displacements of the Pacific jet extension are likely tied not only to specific teleconnections like the PNA and MJO but also to downstream, medium-range forecast skill.

Additionally, although forecasts initialized during retractions had the highest forecast errors in comparison to the other three jet regimes, the subset of retractions that led to the best forecasts were characterized by zonal wind and geopotential height anomalies characteristic of SOM node 1 (Winters et al. 2019b, their Fig. 12c), which subsequently evolved towards a poleward extension (Winters et al. 2019b, their Fig. 14c). This is consistent with the node 1 preferring to transition into other poleward deflected states of 2 and 3 for transition timescales under 10-days. The subset of retractions that lead to the worst forecasts, however, were characterized by more negative geopotential heights in the subtropical Pacific and a positive zonal wind anomaly in the subtropics (Winters et al. 2019b, their Fig. 12d)- an environment more characteristic of SOM node 9. The reduced forecast skill of retraction environments resembling node 9, however, is not consistent with the comparison between node 1 and 9 theoretical predictability (Ch. 3, Figs 3.3 and 3.3).

The differences in forecast skill between extended and retracted regimes highlighted in Winters et al. (2019b) taken with the differences in preferred transitions and synoptic scale environments that characterize SOM node regimes suggest that previous analysis of jet variability blends important jet structures with varying underlying processes and teleconnections. Further separation of jet variability into the 12 SOM nodes provides a more detailed representation of the wintertime Pacific jet that can be utilized to characterize preferred transitions and their relationship to teleconnection patterns like the PNA, MJO, and ENSO (e.g. Madden and Julian 1971, 1972; Wallace and Gutzler 1981; Barnston and Livezey 1987; Franzke and Feldstein 2005; Athanasiadis et al. 2010; Wettstein and Wallace 2010; Franzke et al. 2011). Assessment of such teleconnections, in addition to discerning the roles of tropical versus extratropical processes in driving preferred transitions of the Pacific jet can add considerable value to both medium-range forecasts and sub-seasonal to seasonal forecasts. The following chapter employs a linear inverse model (LIM) to

further assess the predictability of SOM-identified jet patterns and transitions between them. Comparison of transitions in the LIM to observed preferred transitions lends insight into the physical processes governing specific transitions as well as their predictability.

10-Day Transition from Node 11 to 12
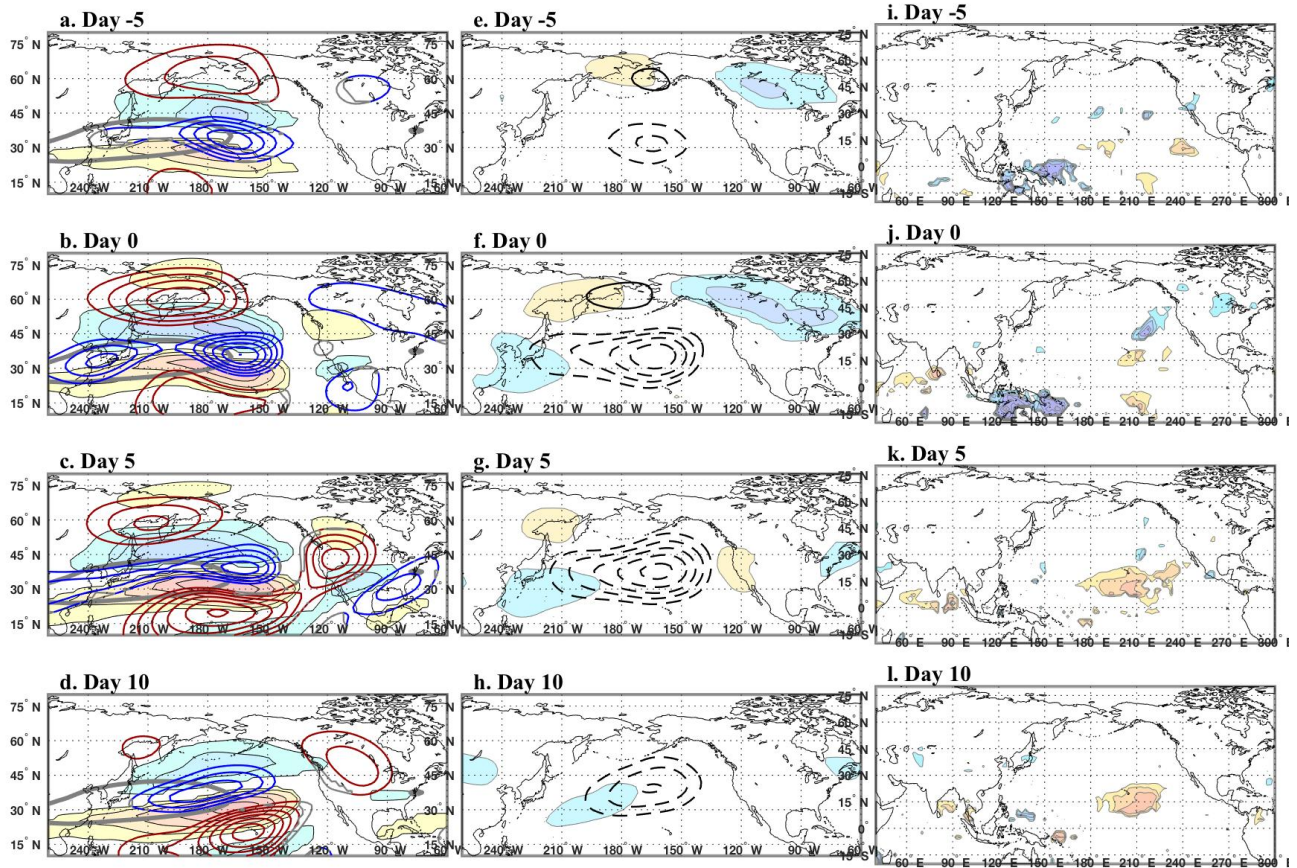
Figure 4.1: Composite large-scale features of SOM node 11 to node 12 10-day transition events (23 composited days) at lags -5, 0, 5, and 10 in which lag 0 is the start of the transition from node 11 and lag 10 is the end of the transition, characterized by node 12. **LEFT:** positive (negative) 200 hPa stream function ($x10^6 m^2 s^{-1}$) anomalies in red (blue) contoured every $2x10^6 m^2 s^{-1}$ starting at 4 (-4) and 250 hPa zonal wind anomalies (ms^{-1}) in red/yellow (blue/purple) contoured every 4 ms^{-1} starting at 4 ms^{-1} (-4 ms^{-1}), significant at the 95% significance level. Thick gray contour is the 40 ms^{-1}NDJFM mean isotach. **MIDDLE:** positive (negative) 850 hPa stream function anomalies ($x10^6 m^2 s^{-1}$) in solid (dashed) black lines contoured every 4 $x10^6 m^2 s^{-1}$ starting at 4 (-4) and 850 hPa temperature anomalies (°K) in red/yellow (blue/purple) contoured every 2 K starting at 2 K (-2 K), significant at the 95% significance level. Gray solid/dashed contours denote structures outside of the 95% significance level. **RIGHT:** positive (negative) OLR anomalies (Wm^2) in pink/yellow (blue/purple) contoured every 5 (-5) starting at 10 (-10), significant at the 95% significance level.

10-Day Transition from Node 12 to 7
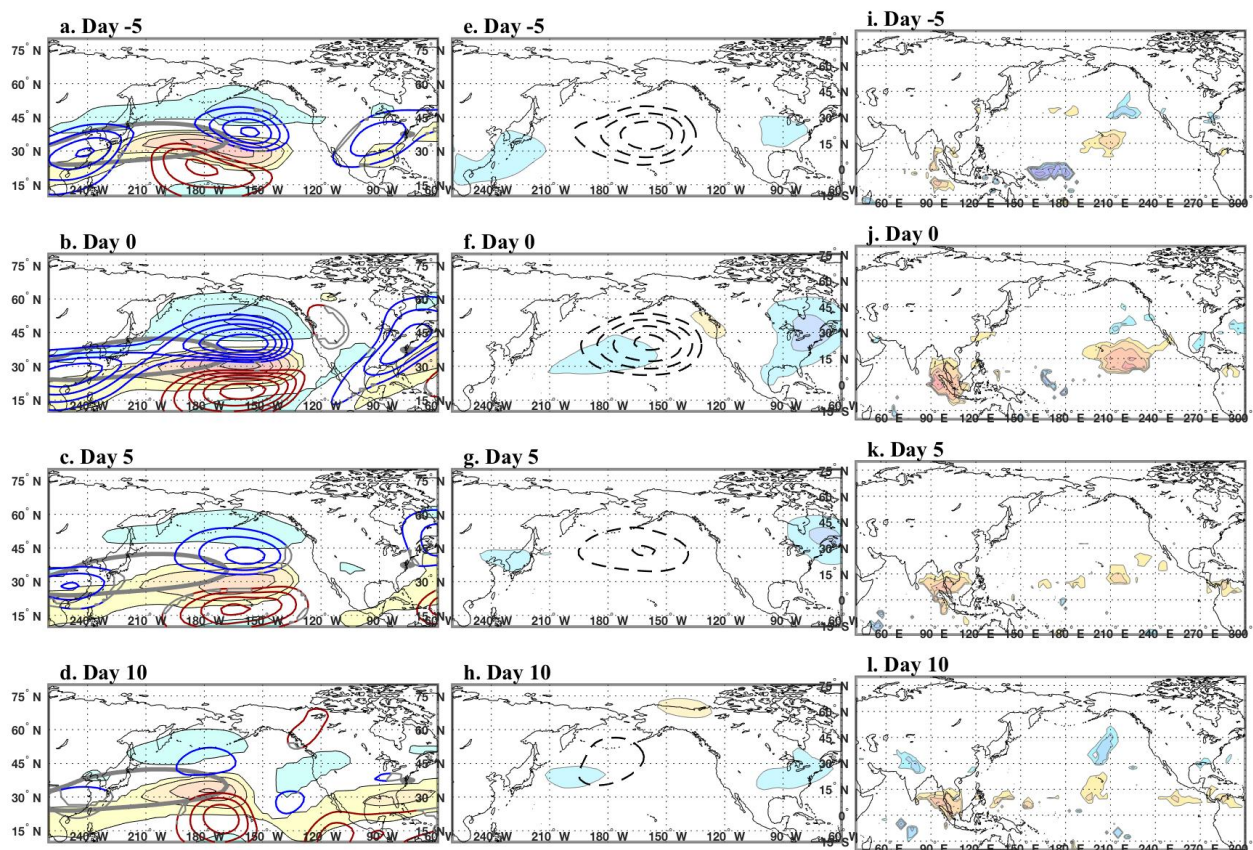
Figure 4.2: As in Figure 4.1 but for the 10-day transition from node 12 to node 7 (30 composited days

10-Day Transition from Node 10 to 9
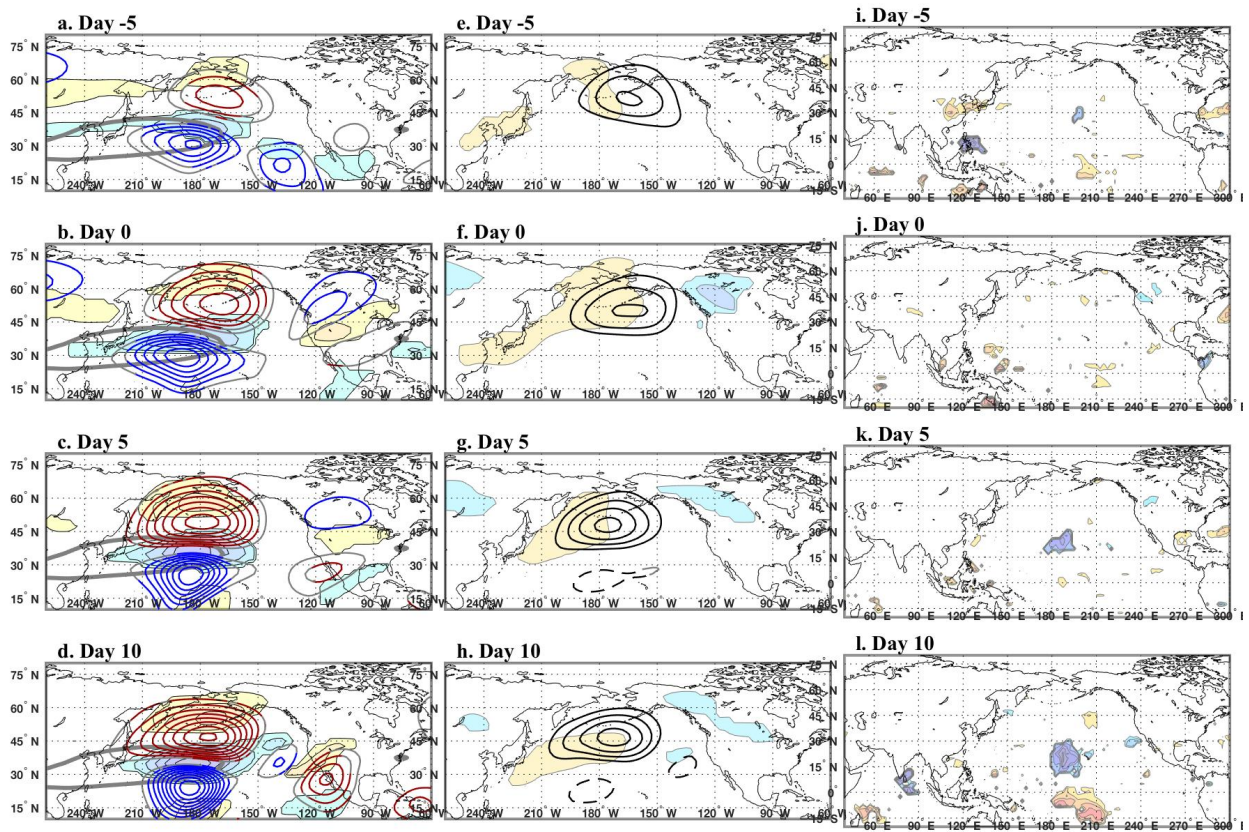
Figure 4.3: As in Figure 4.1 but for the 10-day transition from node 10 to node 9 (15 composited days).

15-Day Transition from Node 9 to 8
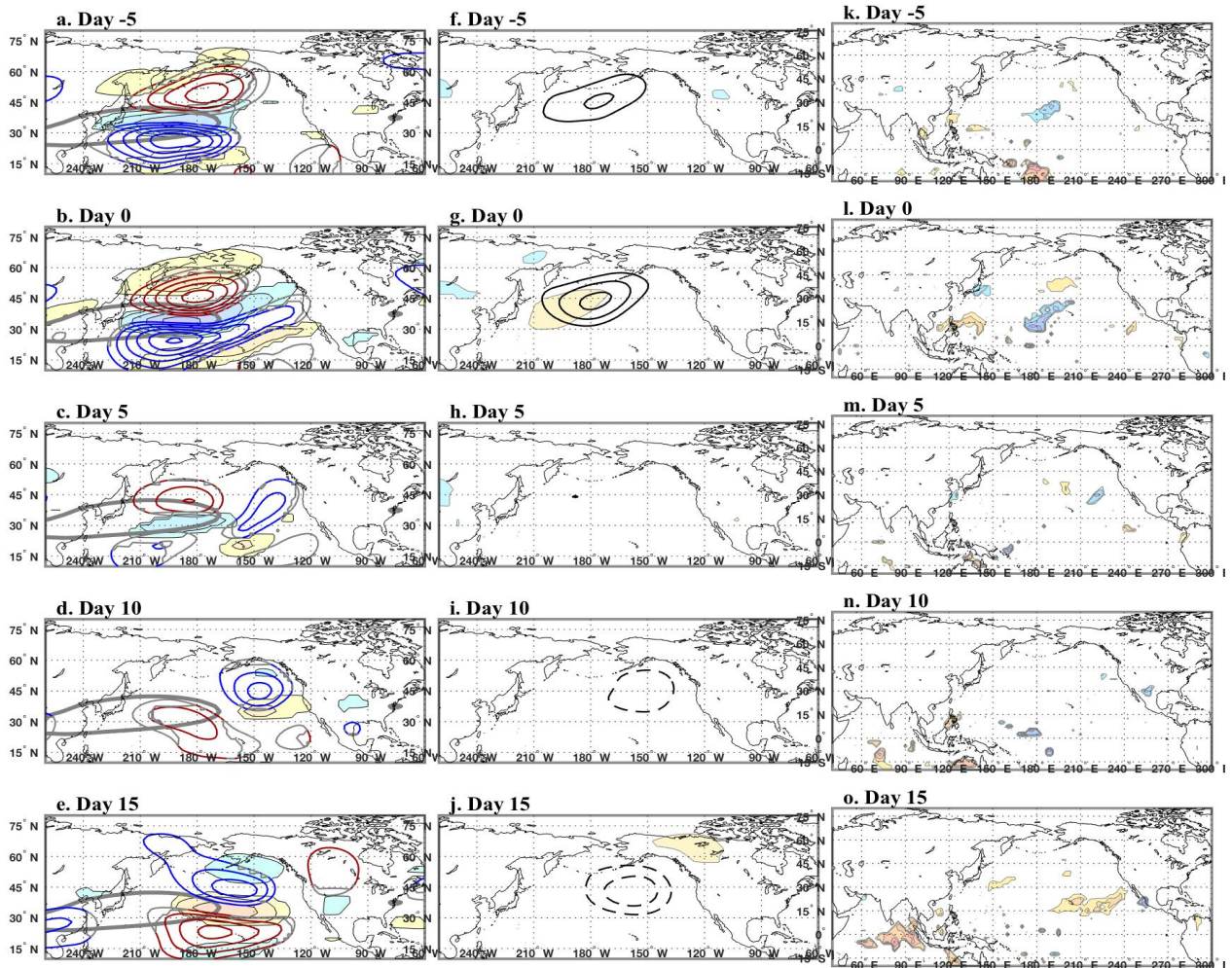
Figure 4.4.: As in Figure 4.1 but for the 15-day transition from node 9 to node 8 (24 composited days).

CHAPTER 5: INVESTIGATION OF NORTH PACIFIC JET TRANSTIONS IN A LINEAR INVERSE MODEL

In Chapters 2-4, intraseasonal transitions of the north Pacific jet were characterized through application of SOM analysis, transition probability tables, and composite analysis. Computed transition probabilities through a 12-node SOM grid at varying timescales from 5 days to 20 demonstrate that there are preferred pathways in which the jet transitions from one node into another. Additionally, it was observed that although transitions featuring extreme zonal wind changes (i.e. transitions between nodes on opposite ends of the SOM grid) were unlikely or insignificant at 10 days and under, the transition from retracted node 9 to extended node 8 became a preferred transition at 15 days for DJF and 20 days for NDJFM. No such preferred transitions were observed for extended states into retracted states, however, indicating an asymmetry in the preferred transitions.

To further characterize the nature of intraseasonal Pacific jet transitions and extratropical and tropical processes associated with them, a Linear Inverse Model (LIM; e.g. Penland and Sardeshmukh 1995) is employed. The LIM is an empirical model wherein the system dynamics are inferred from lagged covariance statistics. In a LIM, the 'coarse-grained' dynamics are estimated as the sum of slowly evolving linear dynamics and rapidly evolving stochastic white noise. In this Chapter, a forward integration LIM is constructed to investigate whether the preferred and unlikely transitions observed in the reanalysis can be replicated in a LIM framework. Next, the LIM is used to optimize growth towards an extended SOM node 12 jet configuration, as node 12 is most accurately modeled in the forward integration LIM. The analysis reveals optimal tropical and extratropical conditions that lead to the node 12 extension.

5.1 Background and Methodology

Recently, linear inverse modelling has been successfully used to quantify the optimal precursors to large-scale circulation patterns in the north Pacific and North American region (e.g. Penland and Sardeshmukh 1995; Alexander et al. 2008; Vimont et al. 2014; Newman et al. 2016; Breeden et al. 2020; Henderson et al. 2020) and as a forecast tool (e.g. Winkler et al. 2001; Albers and Newman 2019) with comparable intraseasonal forecast skill to operational models. For example, Albers and Newman (2019) utilized a LIM to make boreal wintertime forecasts and identify "forecasts of opportunity" at sub seasonal (3-6 weeks) timescales, in which skill was comparable to the European Centre for Medium-Range Weather Forecasts (ECMWF) and National Centers for Environmental Prediction (NCEP) operational models. Similarly, Winkler et al. (2001) used a LIM constructed of only tropical heating and stream function to forecast wintertime mid-latitude variability on timescales beyond a week. Their results indicated that the week 2 LIM skill was comparable to the global nonlinear medium-range forecast (MRF) model from NCEP, and that the competitive skill was not confined to strong ENSO events.

The LIM has also recently been applied as a diagnostic tool to identify optimal initial tropical and extratropical structures that grow towards blocking events in the north Pacific (Breeden et al. 2020). Results from the study revealed that the LIM was able to reproduce the blocking evolution observed in composite analyses, and that both tropical and extratropical processes contributed to the growth of the block. Henderson et al. (2020) developed an internal atmospheric space LIM to separately examine the roles of the MJO and ENSO in the variability of the PNA teleconnection pattern, finding that PNA growth is largely impacted by interference of the MJO and ENSO. Overall, implementation of the LIM in previous work has demonstrated that it is both versatile in its application and computationally inexpensive, making it an ideal tool with which to investigate Pacific jet transitions.

The LIM uses lag covariance statistics to approximate dynamical properties and the evolution for atmospheric variables contained within an anomaly state vector, $\mathbf{x}$. This system, $\mathbf{x}$, is characterized by the following linear stochastic equation:

$$\frac{d\mathbf{x}}{dt} = \mathbf{Lx} + \boldsymbol{\xi}, \tag{5.1}$$

where $\mathbf{L}$ is the dynamical system operator containing both the predictable, slowly evolving linearized dynamics and a linear approximation to nonlinear dynamics, and $\boldsymbol{\xi}$ is the unpredictable white noise forcing (e.g. Winkler et al. 2001). The homogeneous system in (5.1) can be solved with the propagator $\mathbf{G}_\tau$ to obtain the deterministic evolution of $\mathbf{x}$ from an initial time $t = 0$ to lag t $= \tau$:

$$\mathbf{x}(\tau) = \mathbf{G}_\tau \mathbf{x}(0) = \exp(\mathbf{L}\tau)\mathbf{x}(0), \tag{5.2}$$

wherein $\mathbf{G}_{\tau 0}$ at a chosen training lag τ_0 is determined from the covariance of $\mathbf{x}$ at $t= 0$ ($\mathbf{C}_0$) and τ_0 ($\mathbf{C}_\tau$) :

$$\mathbf{G}_{\tau 0} = \mathbf{C}_\tau \mathbf{C}_0^{-1}, \tag{5.3}$$

and from (5.2), the system operator,

$$\mathbf{L} = \ln(\mathbf{G}_\tau) / \tau_0. \tag{5.4}$$

Once $\mathbf{L}$ is obtained, forecasts of $\mathbf{x}$ can be determined for any lag by recalculating $\mathbf{G}$,

$$\hat{\mathbf{x}}(t + \tau) = \exp(\mathbf{L}\tau)\,\mathbf{x}(t) = \mathbf{G}(\tau)\mathbf{x}(t). \tag{5.5}$$

The white noise forcing, $\boldsymbol{\xi}$, can be approximated using the fluctuation-dissipation relation (e.g. Penland 1989, Penland and Matrosova 1994) from $\mathbf{L}$ and $\mathbf{C}_0$:

$$\mathbf{LC}_0 + \mathbf{C}_0 \mathbf{L}^T + \mathbf{Q} = 0, \tag{5.6}$$

where $\mathbf{Q}$ is dt multiplied by the covariance matrix of the stochastic white noise forcing, $\boldsymbol{\xi}$. The eigenfunctions of $\mathbf{Q}$ with the largest eigenvalues serve as the dominant patterns of forcing, also known as noise EOFs. Using equations 5.1-5.6, forecasts for any dynamical system can be

computed; however, if the dynamical system follows the form (5.1), it should be verified that the statistics of the system are Gaussian and that the dynamical system operator, **L**, is independent of the training lag. Additionally, it should be tested that **Q,** calculated from the fluctuation-dissipation relation, is positive definite, and that forecasts are good wherein LIM forecast errors grow consistent with theory (Penland and Sardeshmukh 1995). The subsequent sections describe the data used to create the LIM state vector, **x**, and the tests completed to ensure numerical stability of the LIM.

5.2 Constructing the LIM

For this work, the LIM is derived utilizing the November 1-March 31 (NDJFM) ERA-Interim reanalysis dataset (Dee et al. 2011). The data, available at 6 hourly intervals and a resolution of 1.5°x1.5°, is averaged daily between 1979-2016 for a total of 37 NDJFM boreal cold seasons. The LIM state vector, **x**, is composed of EOF-truncated 250 hPa zonal winds, 850 hPa and 200 hPa extratropical stream function, and apparent heat source (Q1, Yanai et al., 1973). Prior to calculating EOFs, the seasonal cycle and long-term trend are removed, and a 5-day running mean is applied to the anomalous quantities. EOFs of the 250 hPa zonal wind are calculated over a domain between 10°N-80°N and 100°E -240°E. The first 8 EOFs are kept and explain 80% of the variance. Stream function at 850 hPa and 200 hPa is calculated utilizing daily zonal and meridional winds, and EOFs are computed over the domain 10°N-80°N and 0°E -360°E, in which 70% of the variance is explained by the leading 11 EOFs and 13 EOFs, respectively. Lastly, Q1 is calculated following Yanai et al. (1973), and is comprised of radiational heating, latent heat release from condensation, and vertical convergence of sensible heat by vertical eddy transport. Q1 is computed over the domain of 20°S-15°N and 0°E -360°E, in which the state vector contains the leading 15 EOFs to explain 35.6% of the variability. The truncations for each field were selected

to retain a numerically stable LIM, in which the state vector, **x**, is comprised of 47 total EOF components. The training lag used to calculate **L** is $\tau_0 = 5$ days.

5.2.1. Tests for LIM Stability and Robustness

Prior to investigating Pacific jet SOM nodes and transitions in the LIM, the LIM is subjected to tests assessing the validity of the assumed linear dynamics of the system. For a system governed by linear dynamics driven by Gaussian white noise of the form (5.1), the evolution of the system, **L**, is independent of the chosen training lag, τ_0. A useful test for the assumption of linearity for the system **L** in this study is the τ-test, developed in Penland and Sardeshmukh (1995). The τ-test is constructed by computing the submatrices of **L** as a function of training lag $,\tau_0$. Rearranging equation 5.2, 20 estimates of **L** are computed using a τ_0 between 1-20 days,

$$\mathbf{L} = \tau_0^{-1} \ln\{\mathbf{C}(\tau_0)\mathbf{C}(0)^{-1}\}, \tag{5.7}$$

which results in a 47x47 EOF matrix and 47 corresponding curves in Figure 5.1. Each curve in Figure 5.1 is the norm of the submatrices $\mathbf{L}_n$ of decreasing rank, such that $\mathbf{L}_1 \equiv L_{11}$ and $\mathbf{L}_{47} \equiv \mathbf{L}$. Figure 5.1 illustrates that for a τ_0 between 1-5 days, the norms remain relatively flat, suggesting that the dynamics of **L** are insensitive to τ_0 between 1 and 5 days. Therefore, the assumption of linearity is valid with the training lag $\tau_0 = 5$ used to construct the LIM in this study.

Another assumption made in the construction of the LIM is that the state vector, **x**, has stationary statistics. This implies that the operator, **L**, is stable wherein its eigenvalues have negative real parts denoting decay. As described by the fluctuation-dissipation relation (5.4), the decay in variance over time from the dynamics of **L** must be balanced by an increase in variance over time from the stochastic white noise forcing, **Q**. As such, **Q** must have real and *positive* eigenvalues, which is a necessary test to assess the stability of the LIM (Penland and Sardeshmukh 1995). Eigen analysis of **Q** reveals that there is 1 negative eigenvalue; however, to determine

whether the effects of the negative eigenvalue on the system are minor, $\mathbf{C}_0$ is recalculated after removal of the negative eigenvalue. A Lyapunov Equation is utilized to recompute $\mathbf{C}_0$, and eigenvalues of $\mathbf{C}_0$, as well as the variance explained by each EOF, are illustrated in Figure 5.2. The difference in variance, as well as the amplitude of the eigenvalue, are almost indistinguishable between the original $\mathbf{Q}$ and modified $\mathbf{Q}$. Thus, it can be concluded that the negative eigenvalue does not have a first-order influence on the dynamics of the system, and the assumption of stationary statistics remains valid.

Another test involves comparison of the forecast error growth of the LIM to theory. The forecast error growth is calculated from the trace of the error covariance matrix:

$$< e(\tau)e(\tau)^T > = \mathbf{C}(0) - \mathbf{G}(\tau)\mathbf{C}(0)\mathbf{G}^T(\tau), \tag{5.8}$$

in which $< e(\tau)e(\tau)^T >$ is the domain-integrated forecast error variance, $\delta(\tau)$. Figure 5.3 illustrates the error growth derived from the LIM, theory, a persistence forecast, and a first-order auto-regressive (AR-1) forecast. Over a lead-time of 1-30 days, the LIM performs substantially better than both persistence and an AR-1 forecast. Compared to theory, the LIM error is only marginally higher. Therefore, it can be assumed that forecasts made from (5.2) are 'good' (i.e., consistent with theory).

5.3 Forward Noise Integration LIM

Transitions of the Pacific jet are examined in a foreword integration LIM. The system matrix, $\mathbf{L}$, calculated from (5.4) is utilized to generate a simulation of Pacific jet transitions in a time-dependent empirical dynamical model. Following Penland and Matrosova (1994), equation (5.1) is integrated in a two-step process using a finite time step, Δt:

$$\mathbf{y}(t + \Delta t) = (\mathbf{I} + \mathbf{L}\Delta t)\mathbf{y}(t) + \Delta t^{\frac{1}{2}}\mathbf{Sr}(t), \tag{5.9}$$

and

$$\mathbf{x}(t + \Delta t/2) = \frac{\{y(t+\Delta t)+ y(t)\}}{2},\qquad(5.10)$$

where **I** is an identity matrix, **r** is a Gaussian noise vector, and **S** is a matrix characterized by the eigenvectors of **Q** multiplied by the square root of the corresponding eigenvalues.

The forward noise integration model is run for 10,000 days with a time step of 3 hours, and model output is subjected to consistency checks between the simulation timeseries and the observed data timeseries. The 250 hPa zonal wind state space EOFs are then projected onto the model simulation data and multiplied by their norm. In order to classify each of the simulated 10,000 daily zonal wind patterns as one of the 12 SOM nodes, the 12 Pacific jet SOM patterns (Chapter 2, Fig. 2.3) are prescribed as a norm (**N**). The 12 SOM patterns, based on composite 250 hPa zonal wind anomalies, are projected onto the 250 hPa zonal wind state space EOFs and divided by their norm. Any areas outside of the zonal wind anomalies depicted in the original SOM nodes are set to zero, as well as 200 hPa and 850 hPa stream function and Q1, such that the norm vector, $r_{SOM\ node} = [\,0\ 0 \ldots r_{u_{250}} \ldots 0\ 0\,]$. Each of the 12 norm vectors, $r_{SOM\ node}$, are normalized, and 12 final norms, **N**, are computed by,

$$\mathbf{N} = r_{SOM\ node}\, r_{SOM\ node}^{T} + \epsilon\mathbf{I},\qquad(5.11)$$

in which the identity matrix **I** is multiplied by a non-zero scalar $\epsilon=1\mathrm{x}10^{-6}$ for numerical stability (Vimont et al. 2014; Henderson et al. 2020; Breeden et al. 2020). The 12 norms derived from the SOM nodes are projected onto the LIM 250 hPa zonal wind EOFs to reconstruct the two-dimensional patterns observed in the original SOM grid (Fig. 5.4). Comparison between the original SOM nodes and the reconstructed LIM norms reveals good agreement; however, the zonal wind anomalies illustrated in nodes 6 and 7 are of much larger magnitude than the anomalies depicted in the original SOM grid. In the original SOM, nodes 6 and 7 were characterized by anomalies between 8-16ms^{-1} weaker than the neighboring nodes.

With the 12 LIM-derived SOM nodes, LIM "SOM" norm membership is determined through minimizing a root mean square error (RMSE) between each of the 10,000 days of model output and each of the 12 "SOM" norms, **N.** Model output is projected onto the 250 hPa zonal wind state space EOFs prior to computing an RMSE. A new 1x10,000 vector is generated containing the "SOM" norm number with the smallest RMSE error. As a consistency test between the LIM-prescribed "SOM" norms and the original SOM nodes, each day within the observed ERA-Interim 1979-2016 NDJFM timeseries in **x** is prescribed a "SOM" norm number from the method described above. The correlation between the original 1979-2016 reanalysis SOM node timeseries and the LIM-derived "SOM" timeseries is 0.82. The high correlation reveals that the LIM-derived "SOM" norms are a reasonable representation of the SOM patterns, and that SOM membership can be determined from a minimization of RMSE error between the norm, **N**, and model output.

5.3.1. Forward Integration "SOM" Nodes

The composite patterns for the days characterized by the LIM-derived "SOM" nodes 1-12 are computed by projecting the forward model output onto the 250 hPa zonal wind state space EOFs multiplied by their norm. Using the associated 1x10,000 vector containing the SOM norm membership, a zonal wind anomaly average for days characterized by each of the 1-12 norms is computed and depicted in Figure 5.5. The associated frequency of occurrence (FOC) is calculated by summing the number of days characterized by a "SOM" norm and dividing by the total number of model output days (10,000).

The composite structure of the 12 LIM-derived "SOM" nodes is illustrated in Figure 5.5. In general, the composite structure resembles the NCEP/NCAR reanalysis SOM grid (Chapter 2, Fig. 2.3). However, as in the figure depicting LIM norms (Fig. 5.4), node 6 is characterized by much

larger zonal wind anomalies than in the original SOM grid and has a lower FOC (6.9%) than the original SOM node 6 (10%), which is expected due to the enhanced anomalies. The positive zonal wind anomaly characterized by LIM-derived node 7 is also marginally stronger than SOM node 7, and correspondingly, has a lower FOC (8.9% compared to 11%). The FOC of all other nodes ranges between 6.5 % ("SOM" 3) to 11% ("SOM 4"). The LIM norm for SOM 12 has one of the largest increases in FOC, with a 10% FOC in the LIM compared to a 6.6% in the observed SOM grid, whereas the norm for SOM 11 has the same FOC in both (6.8%). The norms for SOMs 2 and 8 are also very similar to the original SOM grid, with only a .2% and .3% difference, respectively. In general, the foreword integration LIM reproduces most of the SOM nodes with very similar magnitude, structure, and FOC. The next section analyzes the likely and unlikely transitions in the LIM space with the LIM-derived "SOM" nodes to examine whether similar preferred transitions identified in Chapter 3 occur in a linear framework.

5.3.2. Forward Integration "SOM" Transitions

Transitions probability tables for lags 5, 10, 15, and 20 are computed by the same method used in Chapter 3, which is modeled off a first order Markov chain,

$$P_{ij}(n) = P\{X_{t+n} = j \mid X_t = i\}, \tag{5.12}$$

in which the probability of transitioning into node j at lag n only depends on the initial node i. Statistical significance of the transition probabilities is determined through a Monte Carlo sampling method in which unconditional probabilities are produced by sampling 100 random days from the dataset and calculating the FOC of each LIM-derived SOM node within the sample. This is repeated 100,000 times to yield a distribution of FOC for every LIM "SOM" node. A two-tailed t test is applied to identify the transition probabilities above the 95% significance level.

Comparison between the probability tables from the LIM simulated timeseries (Fig. 5.6) to the observed SOM timeseries (Fig. 5.7) show a handful of consistent preferred transitions and unlikely transitions at lags 5 and 10, but by lags 15 and 20, there is little consistency. A persistence signature, denoted by increased likelihoods along the diagonals of the tables, is relatively consistent between the observed and LIM probability tables at both 5 and 10-days (Figs. 5.6 and 5.7 a-b). At lag 5, nodes with the same statistically significant likely transitions as the observed timeseries are nodes 4, 7, 9, and 10. Node 4, depicted by a jet extension and slight poleward deflection, has preferred transitions into node 8 (15%) as well as persistence (29%). Unlikely transitions into nodes 11 and 12 are consistent with Fig. 5.7 as well; however, in the LIM, it is also unlikely that node 4 will transition into nodes 6, 7, and 10 at 5 days. The jet enhancement depicted by node 7 also has the same likely transitions of persistence and into an extension (node 8) as the reanalysis 5-day transition table. However, there are also differences in the unlikely transitions, with the unlikely transitions into retracted nodes 5 being consistent, and additional unlikely transitions into nodes 1 and 2. Node 9, another node with consistent preferred transitions, is most likely to persist (30%), transition into node 5 (12%), or transition into node 10 (17%). The unlikely transitions for node 9 are largely the same as those in the reanalysis SOM grid, with an additional unlikely transition into node 11. The last node with identical preferred transitions, node 10, is likely to persist (30%) or transition into node 11 (17%), whereas it is unlikely to transition into nodes 1-4, as well as nodes 5 and 8. Although there are only 4 nodes with equivalent preferred transitions, most other nodes differ from the reanalysis 5-day probability table (Fig. 5.7a) by only one or two statistically significant nodes. The largest probabilities are observed for persistence, with other preferred transitions occurring into neighboring nodes.

By lag 10, the number of consistent statistically significant transitions drops to almost a fourth of that in lag 5, with higher consistency between preferred transitions than unlikely transitions (Figs. 5.6 b and 5.7 b). Overall, the LIM 10-day probability table has more statistically significant probabilities, with preferred persistence in every node except for node 3, whereas in the reanalysis probability tables, persistence is no longer likely for nodes 5, 6, and 7 as well. The only transitions outside of persistence that are consistent between the LIM and reanalysis are from retracted node 9 to node 10, and equatorward deflected node 11 to a more extended node 12. Unlikely transitions that are consistent are from node 2 to 12, node 4 to 10, node 5 to 12, node 6 to 12, node 11 to 5, and node 12 to 1 and 5.

By lag 15, there are only 2 statistically significant transitions that show up in both the SOM and LIM probability tables (Figs. 5.6c and 5.6c). Extended and equatorward deflected node 12 has a higher likelihood of persistence or reoccurrence, and equatorward deflected node 11 is unlikely to transition into node 1 in both sets of probability tables. Outside of the persistence of node 12, there are no consistent preferred transitions at lag 15. Lastly, by lag 20, the LIM probability table (Figure 5.6d) illustrates that there are only three statistically significant transition likelihoods; a preferred persistence or reoccurrence for nodes 11 and 12, and a preferred transition from node 6 to node 7. Of these three probabilities, only the persistence or reoccurrence of node 12 is observed as a statistically significant transition in the reanalysis lag 20 probability table (Figure 5.7d).

Overall, the probability tables generated from the LIM forward integration model capture more of the likely and unlikely transitions at early to mid-range timescales, but by week 2 and beyond, there is little consistency. Differences between the LIM and observations could be due to an insufficient number of variables in the state vector **x** and/or insufficient vertical resolution to accurately model nonlinear interactions and feedbacks driving Pacific jet transitions. However, out

of all of the LIM-derived SOM nodes, the behavior of node 12 was best modeled by the LIM, with consistent preferred transitions from node 11 into 12 out to two weeks, as well as an enhanced persistent likelihood for node 12 out to 20 days. Additionally, at lags 5 and 10, many of the consistent unlikely transitions involved node 12. This suggests that some of the transitions involving an extended SOM node 12 are driven by linear, stable and stochastically forced dynamics that can be reproduced in the LIM.

5.3.3. Forward Integration Transition Composite: Node 11 to Node 12

In the NCEP/NCAR reanalysis dataset, equatorward deflected node 11 had a consistent tendency to transition into node 12, which was evident in both DJF and NDJFM probability tables. Composites of 10-day transitions from 11 to 12 in Chapter 4 illustrated that the transition was preceded by a semi-persistent negative OLR anomaly on Day -5 and Day 0 that coincided with a strengthened anticyclonic anomaly on Day 5 and 10. Although the LIM-derived transition probability tables largely differ from the observed transition probability tables at timescales beyond a week, the foreword integration LIM was able to recreate the likely transition from node 11 to 12 at lags 5 and 10, and the likely persistence of node 12 through the entire 5- to 20-day period. As this work is motivated by a desire to better understand transitions of the north Pacific jet, the transition from "SOM" node 11 to 12 is further examined through a composite analysis of the LIM transition. Comparison between the composite structure in the reanalysis to the LIM composite structure lends insight into how well this preferred transition can be modeled in the LIM.

The 10-day LIM transition of equatorward deflected "SOM" norm 11 into norm 12 is shown in Figure 5.8. The composite evolution of 250 hPa zonal wind anomalies, 200 hPa stream function, and 850 hPa stream function largely resembles the observed 10-day transition from SOM node 11

to 12 (Chapter 4, Fig. 4.1). Five days prior to the start of the transition, the jet is characterized by positive zonal wind anomalies south of the climatological jet stream as well as an anomalous upper-level low centered over the climatological jet exit region (Fig. 5.8a). The weaker anomalous upper-level high stretching between eastern Russia and Alaska (Fig. 4.1a) is not observed in the LIM Day -5 transition, however. By Day 0, both positive and negative zonal wind anomalies marginally enhance, and the negative 200 hPa stream function anomaly correspondingly strengthens on the cyclonic shear side of the jet (Fig. 5.8b). Two small anticyclonic anomalies are observed on Day 0 as well- one over far northeastern Russia, and another south of the Pacific jet, consistent with the reanalysis composite scale structure. Five days into the transitions, there is a rapid enhancement of the upper-level ridge equatorward of the jet stream extending into the US west coast (Fig. 5.8c). The strengthening of the ridge supports a strengthening and slight extension/poleward deflection of the jet exit region. A weaker negative stream function anomaly is situated over eastern North America, consistent with the observed composite structure on Day 5; however, the reanalysis composite also features a positive stream function anomaly over the Pacific Northwest, more strongly resembling a positive PNA teleconnection pattern. This positive anomaly is not reproduced in the LIM. By Day 10, the ridge equatorward of the jet stream further intensifies, and the jet exit region deflects a few degrees north and strengthens into a node 12-like pattern.

The composite 850 hPa stream function evolution also largely resembles the observed composite transition, with a weak negative anomaly over the central Pacific on Day -5 (Fig. 5.8e) that strengthens over the following 10 days (Fig. 5.8 f-g). Unlike the observed composite evolution, however, the negative 850 hPa stream function anomaly in the LIM composite does not weaken between Day 5 and Day 10 (Fig. 5.8 g-h); rather, it remains nearly static.

The tropical heating (Q1) anomalies associated with the LIM transition exhibit less consistency with the observed transition than the extratropical variables. On Day -5, the LIM composite illustrates a strong positive Q1 anomaly near the equator and east of the dateline, indicative of enhanced convection and El Niño-like conditions (Fig. 5.8i). A region of suppressed convection is observed in the East Indian Ocean into the western Pacific, and another area of enhanced convection is evident over the southern Indian Ocean. In the observed composites, the region of enhanced convection is located further west on Day -5, near the Maritime Continent and tropical west Pacific basin (Fig. 4.1i). The location of enhanced convection in the reanalysis composite resembles the OLR anomalies leading to positive PNA events in Franzke et al. (2011, their Fig. 11). This could explain why the reanalysis stream function composite more strongly resembles a PNA-teleconnection pattern than the LIM composite structure. In the LIM composite, the transition seems to be preceded by El Niño-like conditions over the Pacific with little change between Day -5 to Day 5. By Day 10, the negative Q1 anomalies expand over the Maritime Continent, and a weaker area of positive Q1 anomalies forms over Indian Ocean (5.8l). In the observed composites, a large positive OLR anomaly is evident over the central subtropical Pacific, and smaller areas of OLR anomalies are scattered over the Indian Ocean and far tropical west Pacific (Fig. 4.1l). In general, the LIM extratropical composite transition evolves in a similar manner to the reanalysis composite transition, with a strengthening of the subtropical ridge driving an extension and poleward deflection of the jet exit region. The following section applies a diagnostic LIM to identify optimal precursors to a SOM 12 jet extension and discern the relative importance of tropical versus extratropical processes in driving the growth towards an extended SOM 12 jet state.

5.4 Optimal Initial Conditions for Node 12

The consistency between the LIM-derived "SOM" node 12 probability table and composite evolution towards an extended "SOM" 12 norm to observed node 12 behavior suggests that transitions involving the jet extension are more predictable than transitions involving other SOM-identified jet states. As a next step towards understanding the relative importance of extratropical and tropical processes in growing towards a strong extension, this section uses the LIM to optimize growth towards a SOM 12-like Pacific jet pattern. The following analysis first investigates the net optimal tropical and extratropical conditions that grows towards a "SOM" 12 norm. Then, as in Breeden et al. (2020) and Henderson et al. (2020), interactions between tropical heating and extratropical stream function are isolated to discern the contributions from the tropics and extratropics on a node 12 jet extension.

Growth towards a specified anomaly pattern in the LIM occurs when **L** is composed of nonorthogonal eigenvectors, wherein modal constructive or destructive interference leads to the growth or decay over a specified lag, τ (Penland and Sardeshmukh 1995). For the dynamical system used in this work, an example of modal interference is asymmetry in the shear and zonal flow. This growth, $\mu(\tau)$, towards a defined norm (**N**) is defined as:

$$\mu(\tau) = \frac{x(\tau)^T N x(\tau)}{x(0)^T F x(0)} = \frac{x(0)G(\tau)^T NG(\tau)x(0)}{x(0)^T F x(0)}, \tag{5.13}$$

in which **F** is the final norm kernel and **N** represents the initial norm kernel. In focusing on the growth towards a jet extension denoted by node 12, a final jet norm **N** is used to solve the generalized eigenvalue problem:

$$\mathbf{G}_\tau^T \mathbf{N} \mathbf{G}_\tau \mathbf{p} - \mu(\tau)\mathbf{p} = 0, \tag{5.14}$$

in which **p** denotes the eigenvectors that grow towards **N**. The optimal initial structure is the **p** that maximizes growth ($\mathbf{p}_1$). As in the previous sections, the **N** is defined from the composite 250 hPa zonal winds from days characterized by SOM node 12. Any features outside of the SOM 12 pattern

are set to zero so that the LIM grows only towards the jet extension. The SOM 12 pattern is then projected onto the 250 hPa zonal wind state space EOFs and divided by their norm. The lag (τ) used to find the optimal initial structures that grow towards a jet extension is 10 days.

The optimal initial and evolved final patterns derived by the LIM under a "SOM" 12 jet extension norm are illustrated in Figures 5.9-5.11. The optimal initial conditions that lead to a jet extension depict a weak positive zonal wind anomaly in the climatological jet axis (Figure 5.9). The pattern resembles SOM node 7 (jet enhancement), which is consistent with the LIM-derived 10-day probability table indicating a preferred transition from node 7 to node 12. Upper-level stream function anomalies illustrate a preexisting ridge over the subtropical western Pacific basin and a dipole structure over the east Pacific with a weak cyclonic anomaly over the Gulf of Alaska and a weak anticyclonic anomaly to its south (Fig. 5.10a). The composite structure in the transition from node 12 to node 7 (Fig. 4.2d) also features a meridional dipole of upper-level stream function anomalies; however, the anomalies are further west than in the LIM composite. Another ridge is observed over Eurasia, and weak troughs are located over southern North America, the Atlantic basin, and the southern Arabian Peninsula. The final evolved upper-level stream function depicts a strong dipole over the Pacific basin, with a zonally expansive anticyclonic anomaly south of the Pacific jet, and a cyclonic anomaly south of the Aleutian Islands (Fig. 5.10b). Additionally, a large-scale trough sits over most of Eurasia, stretching from 30°E to 130°E.

At 850 hPa, the optimal initial conditions depict a weak meridional dipole in stream function anomalies of opposite sign and further to the west than the upper-level stream function dipole (Fig. 5.10c). The vertical structure of the 850 hPa and 200 hPa stream function anomalies suggests that the node 12 initial structure is baroclinic. Downstream of the Pacific 850 hPa dipole, another negative stream function anomaly stretches over the Atlantic basin, south of a more

isotropic positive stream. function anomaly. The evolved final 850 hPa stream function structure depicts a sprawling cyclone over the Pacific basin that resides under the upper-level 200 hPa trough, and another weaker cyclone sits over eastern North America (Fig. 5.10d). Comparison between the initial and final structures suggest that the growth of extended node 12 is associated with a transition from a baroclinic to an equivalent barotropic structure.

Turning attention to tropical heating, the optimal initial structure of Q1 depicts an area of enhanced convection centered near the dateline and suppressed convection over the Indian Ocean and over the far western tropical Pacific, just north of the equator. These initial Q1 conditions slightly resemble an El Niño and MJO, indicating that "SOM" node 12 optimally forms from both tropical processes. This is consistent with analysis from Chapter 2, wherein node 12 anomalous FOC exceeded 200% during strong MJO events and an El Niño. By the final condition 10 days later, the Q1 anomaly marginally weakened over the central tropical Pacific, and negative anomalies characterize a larger area of the Maritime Continent and East Indian Ocean. Additionally, a small area of enhanced convection develops over the Indian Ocean.

Although a 10-day optimization period is used to examine growth towards a jet extension characterized by node 12 in this analysis, growth towards "SOM" node 12 occurs at lags out to 20 days (Fig. 5.12). Two peaks in growth are noted in Figure 5.12- one around 5 days and another near 13 days. Therefore, the 10-day optimization period used in this analysis coincides with peak growth towards node 12. Additionally, the optimal structures identified in the LIM are not indicative of *actual* growth towards a jet extension in reanalysis. To test whether the observed dynamics behave in a linear fashion illustrated in Figs. 5.9-5.11, the projection of the optimal initial jet structure onto the LIM state vector versus the projection of the "SOM" 12 norm onto the state vector 10 days later is plotted in Figure 5.13. The positive slope reveals that, in general, the

optimal initial structures illustrated in Figs. 5.9-5.11 *do* lead to a jet extension in the observations, lending significance to the LIM skill in diagnosing optimal SOM node 12 conditions.

5.4.1. Tropical versus Extratropical Impacts on SOM Node 12 Development

The optimal initial and final conditions that grow towards a jet extension illustrated in Figures 5.9-5.11 illustrate changes in both the extratropical and tropical circulation. To discern the relative influence of extratropical and tropical variability in growing towards the extended node 12 pattern, the LIM is initialized first with only the extratropical variables in the optimal initial conditions (with tropical Q1 set to zero in the optimal initial conditions, **p**) and then with only tropical variables (with ψ_{200}, ψ_{850}, and u_{250} set to zero). Then, using (5.5), evolved conditions for the 10-day growth towards a jet extension are computed and compared to Figures 5.9-5.11.

The final conditions for a Q1- initialized LIM are illustrated in Fig. 5.14. The optimal Q1 structure is able to produce a jet extension (Fig. 5.14a), but the maximum positive zonal wind anomaly is located a few degrees further east and is of weaker magnitude. Additionally, the anomaly is less zonal, starting near 45°N and dipping southeast. At 200 hPa, there is still a meridional dipole in stream function anomalies, but the ridge to the south is weaker and less zonally expansive as in the full LIM, and the trough to the north is of weaker magnitude as well (Figure 5.14b). At 850 hPa (Figure 5.14c), the sprawling negative stream function anomaly over the Pacific basin observed in the full LIM is still evident in the Q1 initialized LIM, though it is weaker. Q1 anomalies across the tropical Pacific look largely similar to the Q1 in the full LIM, with regions of suppressed convection stretching from the Indian Ocean to the tropical west Pacific, and a larger area of enhanced convection near the dateline stretching east over the Pacific basin (Fig. 5.14d).

The final evolved conditions for a LIM initialized with only extratropical variables yields a jet structure almost identical, though weaker, to the full LIM (Fig. 5.15a); however, the stream function anomaly pattern at 200 hPa and 850 hPa, as well as the Q1, vary more substantially. At 200 hPa, the dipole over the Pacific is slightly weaker than in the full LIM, and the subtropical ridge is located ~10° to the west (Fig. 5.15b). Similarly, near the surface, the 850 hPa stream function anomaly is weaker and sits ~10° west of the full LIM 850 hPa cyclone (Fig. 5.13c). The final Q1 conditions indicate suppressed convection over the subtropical central Pacific, Maritime Continent, and Indian Ocean, whereas enhanced convection is observed south of the areas of suppressed convection (Fig. 5.15d). Although the Q1 pattern differs substantially from the full LIM and Q1 initialized LIM, it is possible that the heating that develops from interaction with the extratropical circulation contributes to the jet extension in Fig 5.15a. As in Henderson et al. (2020), the effect of Q1 on the extension is tested by setting the off-diagonal tropical elements of **L** to zero and calculating final evolved conditions with (5.5). The final extratropical circulation pattern from the modified **L** is depicted in Figure 5.16, in which it is evident that the magnitude and location of the zonal wind anomaly is unchanged. Therefore, the growth towards the final zonal wind pattern in Fig. 5.15a can be largely attributed to the extratropical circulation. However, in comparing the evolved jet pattern between the full LIM, the tropical Q1 initialized LIM, and the extratropical initialized LIM, it is apparent that both tropical and extratropical processes contribute to the growth of a strong extension. The strength of the extension in each of the modified LIM final conditions is almost half of that in the full LIM, so while the extratropical circulation, alone, can grow towards a jet extension like that of node 12, the El Niño and MJO-like tropical conditions are important in the transition to a strong SOM 12 extension. This is also consistent with earlier findings in Chapter

2, wherein SOM node 12 exhibited the highest correlation to ENSO (0.58) and large FOC changes during ENSO and the MJO.

5.5 Summary

In this chapter, a LIM is developed to determine whether observed preferred and unlikely transitions described in Chapter 3 can be recreated in a linear framework. The LIM, constructed of 200 hPa and 850 hPa stream function, tropical Q1, and 250 hPa zonal winds, is trained with a $\tau_0 = 5$ days and tested to ensure that it obeys linear and stable dynamics. A foreword integration model is run for 10,000 days, and the SOM grid is used to construct 12 norms and a timeseries of days characterized by 1 of the 12 nodes. SOM membership is determined through a minimization of RMSE error between the forward integration model output and the 12 norm patterns. Probability tables constructed from the LIM "SOM" node timeseries reveals that at 5 days, many of the preferred and unlikely transitions between observation and the LIM are consistent (Figs. 5.6a and 5.7a). By 10 days, however, only a handful of transitions remain consistent. The persistence likelihood in the LIM correctly identifies the preferred 10-day persistence for nodes 1, 2, 4, 8, 9, 10, 11, and 12, with node 12 exhibiting the highest persistence likelihood in both observation and in the LIM (Figs. 5.6b and 5.7b). The only consistent preferred transitions into other nodes are from a retracted node 9 to node 10, and equatorward deflected node 11 to an extended node 12. Beyond two weeks, however, only the likely persistence of node 12 is captured in the LIM probability tables (Fig. 5.6c-d). The lack of consistency between the LIM-derived SOM transitions and reanalysis at timescales beyond 10 days could indicate that either the observed preferred transitions are driven by nonlinear processes that cannot be modeled by stochastic white noise, or that the state vector used to construct the LIM has an insufficient number of variables and/or vertical resolution to model the transitions. Still, at 10 days and under, the LIM is able to reproduce

preferred persistence and unlikely transitions for many of the nodes, with transitions involving node 12 exhibiting the most consistency with reanalysis.

The composite evolution of the 10-day LIM transition from node 11 to 12 (Fig. 5.8) is largely similar to the 10-day composite transition in the reanalysis (Fig. 4.1), with a growing ridge on the anticyclonic shear side of the jet that extends and deflects the jet exit region poleward by ~5°-10° to the north. In the OLR reanalysis composite, the transition is preceded by a semi-persistent negative OLR anomaly near the Maritime Continent on Day -5 and Day 0, whereas in the LIM, the Q1 structure indicates suppressed convection over the region, with El Niño-like conditions in the Pacific. This suggests that the transition from node 11 to 12 in the LIM is more strongly tied to ENSO conditions, whereas in the reanalysis, the transition might be tied to enhanced convection over the Indian Ocean, exciting a Rossby wave train and subsequent PNA pattern.

A LIM is also utilized to optimize growth towards a SOM 12-like Pacific jet pattern to further characterize the behavior and predictability of node 12. The optimal extratropical conditions that grow towards a "SOM" 12 illustrate a node 7-like pattern and a baroclinic structure in the stream function anomalies. The final extratropical conditions resemble an equivalent barotropic structure over the Pacific basin. The Q1 anomalies characterizing the tropical initial conditions resemble both El Niño and MJO conditions, with enhanced convection centered near the dateline stretching east. Modification of the LIM optimal initial conditions lends insight into the relative roles of tropical versus extratropical processes in growing towards a jet extension. In initializing the LIM with only extratropical variables or tropical variables, the SOM 12 jet extension is characterized by weaker anomalies, and the tropical Q1-initialized LIM grew towards an extension further east. The separation of the contributions reveals that both tropical and

extratropical processes are important in growing towards a strong extension. Moreover, the LIMs ability to most accurately recreate transitions involving SOM node 12 is likely tied to the tropical ENSO and MJO-like conditions that influence node 12. Overall, analysis from the LIM constructed in this Chapter suggests that while the persistence of many of the SOM nodes can be reproduced in a linear framework, many of the preferred transitions observed between 10 and 20 days cannot, either due to the importance of nonlinear processes in driving the transitions or inadequate system dynamics comprising the LIM state vector.
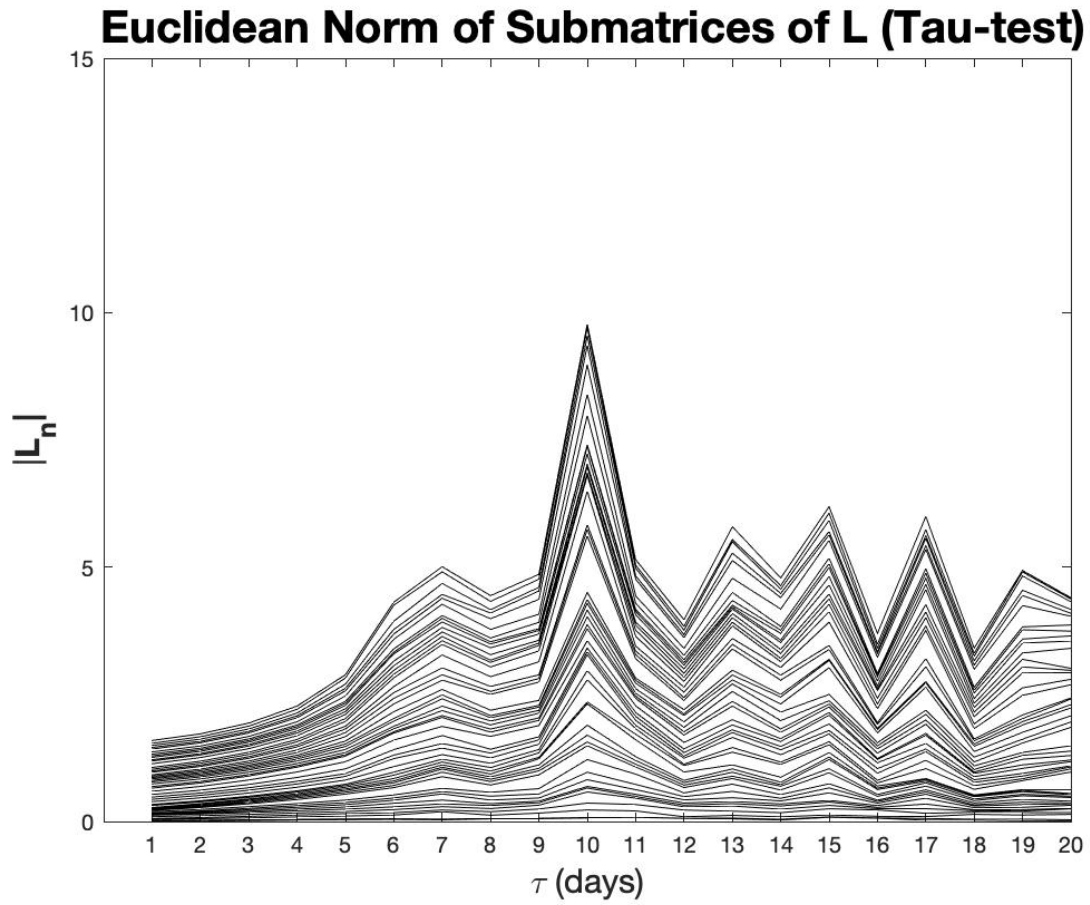
Figure 5.1 Tau-test, developed in Penland and Sardshmukh (1995), for the linear inverse model. The Euclidean norm of the submatrices of **L** are plotted as a function of lag, τ, between 1 and 20 days.
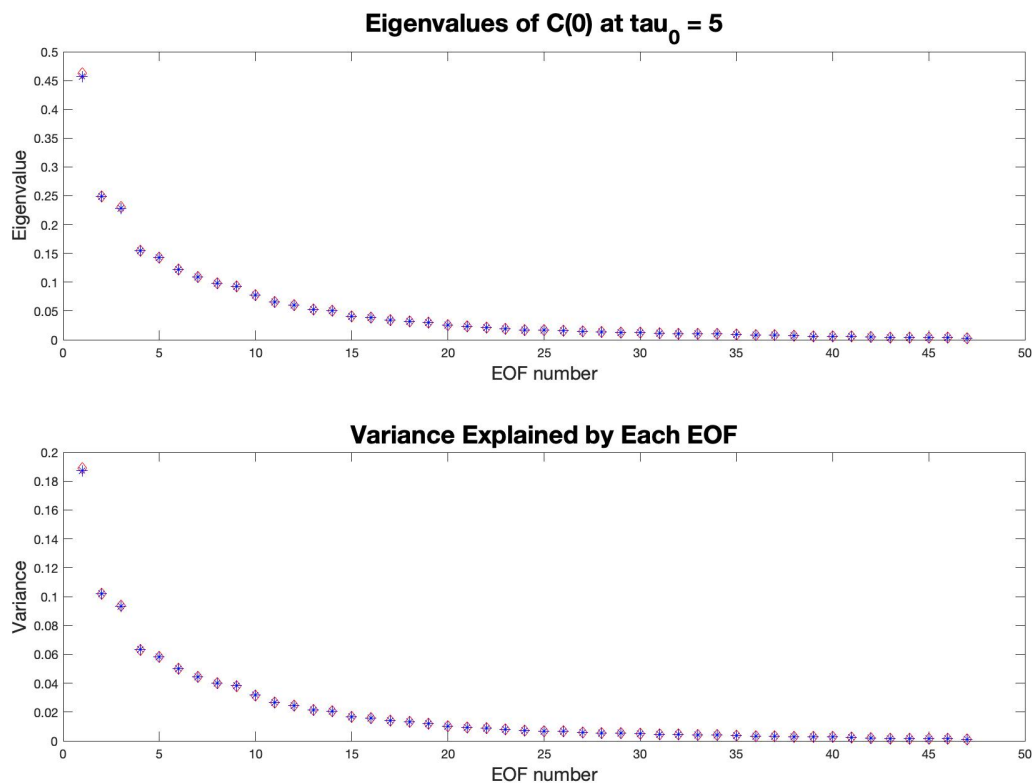
Figure 5.2 TOP: Eigenvalues of the instantaneous covariance matrix, $\mathbf{C}(0)$, computed with a $\tau = 5$ days. Red triangles denote eigenvalues computed from the noise covariance matrix, $\mathbf{Q}$. Blue stars denote eigenvalues computed with the modified $\mathbf{Q}$ from the removal of one negative eigenvalue. **BOTTOM:** Fraction of the variance explained by the EOF of $\mathbf{C}(0)$ in the top for (red triangles) the original $\mathbf{Q}$ and (blue stars) the modified $\mathbf{Q}$.
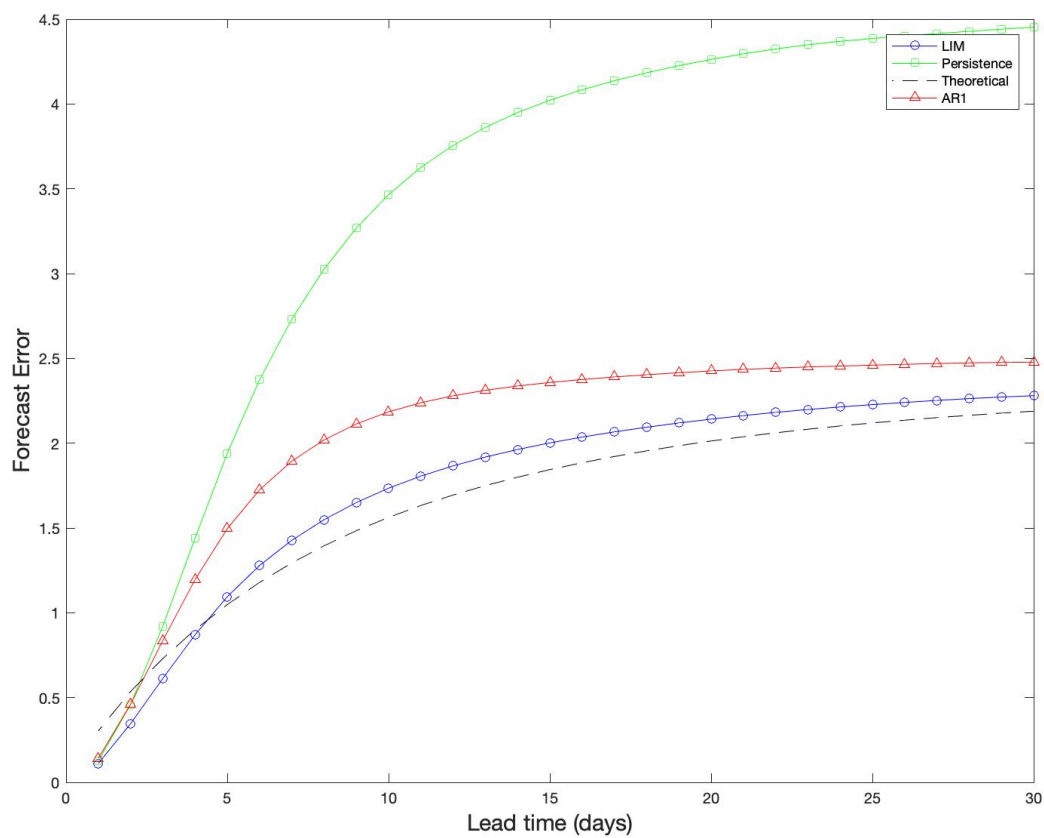
Figure 5.3 Forecast error, calculated as an error variance, produced by the LIM (blue circles), a first order autoregressive (AR1) process (red triangles), persistence (green circles), and theory (black dash).

LIM Norms from SOM Nodes
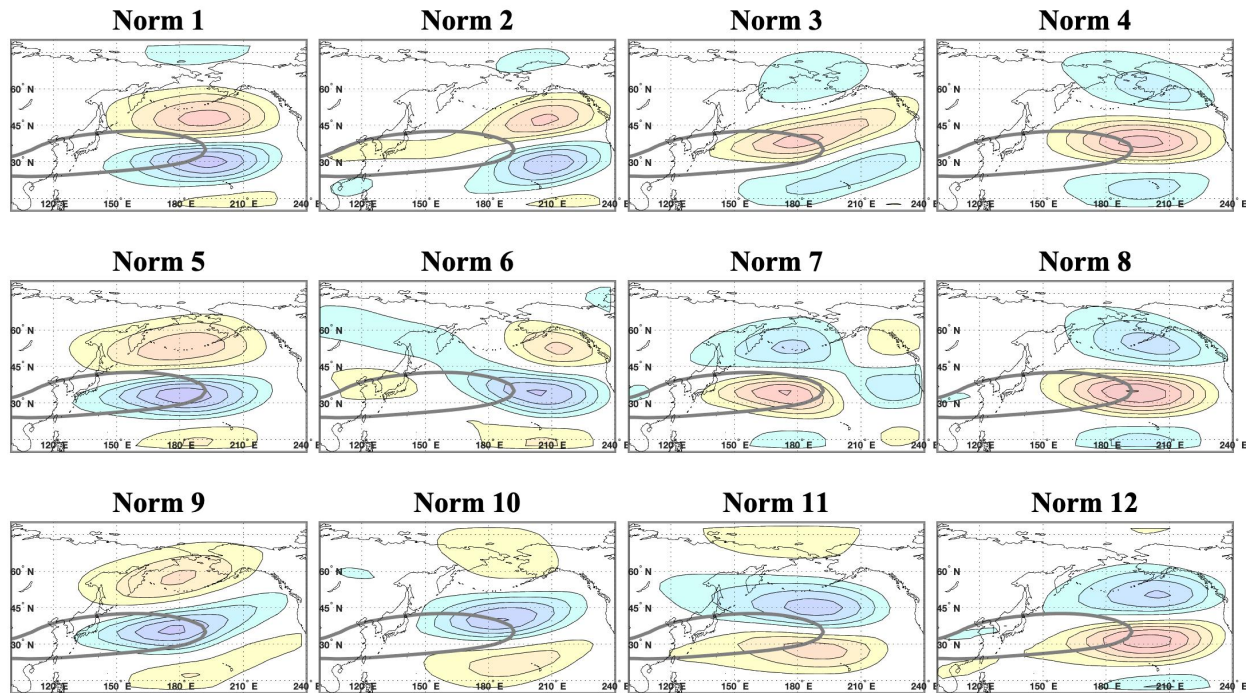
Figure 5.4. (a) Grid of the 12 norms from the SOM nodes projected onto the state space 250 hPa zonal wind EOFs. Anomalies of the 250 hPa isotachs (ms^{-1}) are shaded in warm (cool) colors every 4 starting at 4 (-4). The climatological cold season 40 ms^{-1} isotach is in gray.
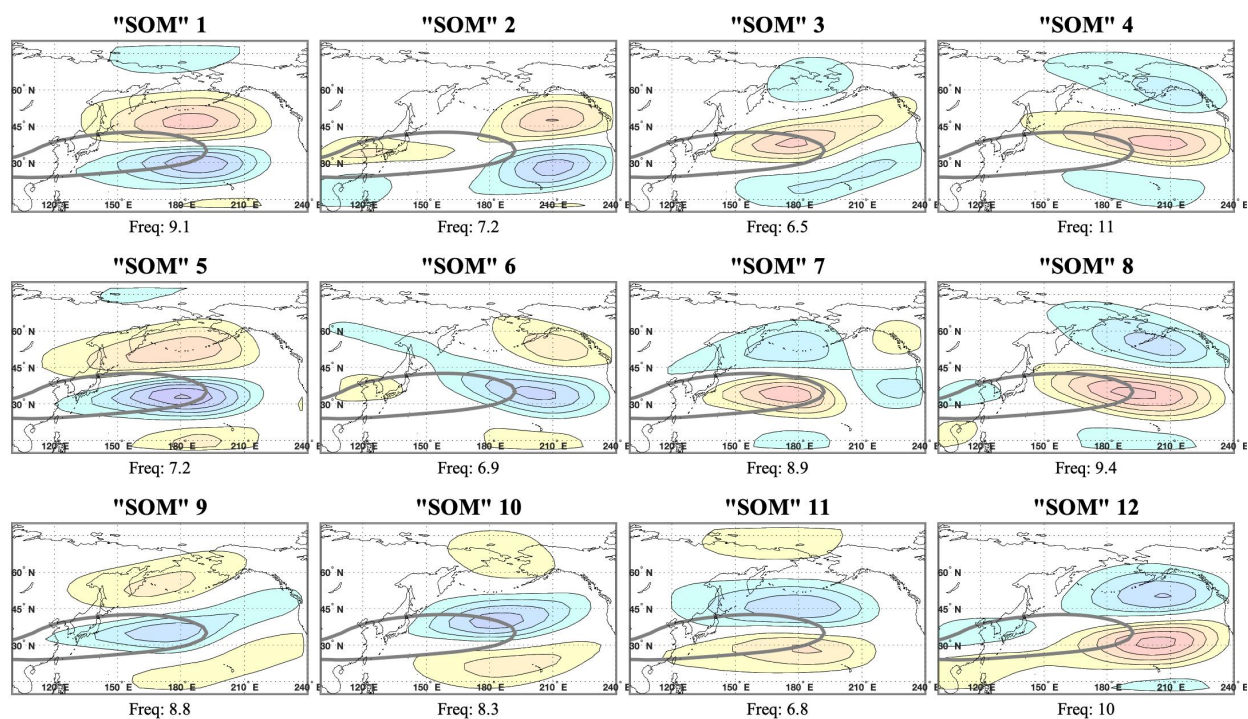
Figure 5.5. Grid of the 12 derived "SOM" nodes from the forward integrated LIM. Anomalies of the 250 hPa isotachs (ms^{-1}) are shaded in warm (cool) colors every 4 starting at 4 (-4). The climatological cold season 40 ms^{-1} isotach is in gray. Below each node is the associated frequency of occurrence (in %) relative to all other nodes.

LIM Transition Probability Tables

(a) Lag 5 — *Final Node*

Original Node	1	2	3	4	5	6	7	8	9	10	11	12
1	34	12	7	11	14	4	3	3	7	2	0	1
2	14	29	15	7	5	12	9	1	2	2	3	1
3	8	10	21	16	4	3	11	9	7	2	3	5
4	12	8	10	29	8	3	3	15	5	2	1	5
5	21	5	2	6	34	8	2	0	14	5	2	1
6	8	14	3	4	6	23	12	2	10	10	6	1
7	1	3	6	8	1	5	29	15	5	5	9	12
8	1	1	5	18	2	2	9	32	5	2	2	19
9	6	3	2	6	12	9	4	4	30	17	3	4
10	2	3	3	4	2	10	5	3	10	30	17	9
11	0	2	3	3	0	7	15	6	3	16	27	18
12	1	1	3	10	1	2	8	12	5	8	13	37

(b) Lag 10 — *Final Node*

Original Node	1	2	3	4	5	6	7	8	9	10	11	12
1	19	10	7	12	13	6	5	8	11	4	2	3
2	12	18	11	8	5	8	14	5	7	6	3	3
3	12	8	9	15	6	8	11	8	6	5	5	7
4	14	9	9	18	9	4	5	13	7	4	2	6
5	17	8	4	12	17	8	6	4	11	7	3	3
6	8	12	6	8	7	14	10	5	7	12	7	5
7	4	4	7	9	4	6	18	11	7	7	9	16
8	5	3	7	15	6	5	10	19	5	6	3	15
9	8	5	5	7	10	8	7	5	18	13	8	7
10	4	6	5	8	4	8	5	8	9	17	14	12
11	3	4	4	5	3	7	13	10	6	11	17	18
12	3	2	4	10	3	4	8	12	9	9	11	23

(c) Lag 15 — *Final Node*

Original Node	1	2	3	4	5	6	7	8	9	10	11	12
1	13	12	7	12	9	8	5	9	11	6	4	5
2	7	11	9	10	6	6	13	8	8	9	6	7
3	11	8	7	12	8	8	9	10	9	5	5	9
4	12	5	8	18	9	6	7	11	8	6	3	8
5	14	9	7	13	11	6	8	9	9	6	3	6
6	11	10	8	8	6	10	9	7	6	10	9	6
7	7	6	7	11	7	6	13	9	7	8	7	13
8	9	5	7	12	7	7	7	15	6	7	6	13
9	8	6	5	9	9	7	8	6	15	9	7	9
10	6	7	4	9	5	9	9	9	8	11	11	12
11	5	5	6	8	4	5	13	10	8	11	12	13
12	7	4	4	9	5	6	8	9	9	12	9	17

(d) Lag 20 — *Final Node*

Original Node	1	2	3	4	5	6	7	8	9	10	11	12
1	11	11	8	12	6	8	5	9	10	7	6	7
2	6	9	7	14	5	9	12	9	9	9	5	6
3	10	8	7	10	9	6	8	9	9	7	5	10
4	10	7	7	13	8	6	6	13	8	6	6	9
5	13	7	7	11	8	5	9	12	9	6	5	8
6	10	11	6	9	5	8	14	8	6	8	8	7
7	10	7	8	9	7	7	11	7	8	7	8	9
8	7	6	7	13	9	7	7	10	8	8	7	13
9	9	5	5	12	9	6	11	9	10	9	5	10
10	8	7	6	10	5	7	9	10	10	9	9	13
11	6	7	5	9	6	8	10	8	8	11	12	10
12	8	4	4	9	7	6	9	9	9	11	7	15

Figure 5.6. 5-20-day anomalous transition probabilities for LIM Norms constructed from SOM nodes 1-12 observed in the LIM foreword integration model data. Within each subplot, columns 1-12 correspond to the SOM Node into which the transition is observed and rows 1-12 correspond to the node at the start of the transition. Red (blue) squares indicate enhanced (reduced) transition frequency at the 95% significance level.

SOM Transition Probability Tables

(a) Lag 5 — *Final Node*

| Original Node	1	2	3	4	5	6	7	8	9	10	11	12
1	23	16	11	11	12	11	7	3	4	2	0	1
2	13	24	15	9	7	10	10	5	2	3	1	0
3	9	10	15	16	5	10	13	14	2	1	3	2
4	7	9	12	23	6	9	9	16	2	4	2	2
5	11	5	9	6	24	10	5	4	15	9	2	0
6	9	11	11	4	9	17	15	4	5	9	6	1
7	6	7	6	7	3	13	18	14	2	8	8	8
8	3	4	7	15	3	4	17	24	2	3	3	14
9	7	3	3	3	20	9	4	2	28	15	5	1
10	4	4	2	1	8	14	8	2	9	29	14	4
11	2	4	3	3	2	8	17	6	3	11	24	18
12	0	2	2	6	4	8	12	14	2	5	12	32

(b) Lag 10 — *Final Node*

Original Node	1	2	3	4	5	6	7	8	9	10	11	12
1	17	9	8	8	11	12	8	7	7	6	3	3
2	12	16	11	12	10	8	10	9	2	4	3	2
3	10	10	11	13	7	9	16	9	3	4	4	4
4	8	12	12	16	6	8	10	12	3	3	5	3
5	11	5	8	5	14	10	8	9	14	10	4	2
6	7	10	8	8	11	13	9	10	8	9	6	2
7	6	6	6	6	9	11	16	10	4	10	9	9
8	4	5	10	12	5	7	12	17	5	6	6	10
9	8	4	7	8	13	9	7	4	13	15	8	4
10	7	6	3	3	9	13	9	7	16	15	7	6
11	4	4	7	8	3	4	10	8	5	10	17	20
12	3	6	5	9	4	10	16	9	3	3	10	20

(c) Lag 15 — *Final Node*

Original Node	1	2	3	4	5	6	7	8	9	10	11	12
1	11	9	6	9	11	11	10	8	6	8	7	4
2	14	11	13	6	10	8	12	10	5	4	3	3
3	10	11	11	8	11	9	13	8	6	4	5	5
4	10	13	10	14	4	8	8	11	4	4	7	7
5	9	9	4	8	10	13	8	8	10	8	8	5
6	8	7	7	10	9	12	11	9	8	9	7	4
7	7	5	5	11	9	10	14	8	7	7	8	8
8	7	8	9	12	6	8	14	11	6	5	6	9
9	8	4	10	14	12	8	8	12	4	9	7	2
10	5	3	4	8	14	13	13	4	14	10	7	5
11	3	4	5	10	7	13	11	7	6	10	10	13
12	5	6	7	7	7	8	9	10	8	6	8	21

(d) Lag 20 — *Final Node*

| Original Node	1	2	3	4	5	6	7	8	9	10	11	12
1	8	9	10	12	9	10	6	9	9	8	4	5
2	10	12	13	9	12	11	8	6	6	5	3	5
3	12	9	10	7	8	12	11	6	7	9	6	4
4	9	8	14	12	5	8	11	9	5	3	9	7
5	11	7	7	8	11	10	6	8	6	9	10	7
6	7	7	10	8	10	10	11	7	7	10	7	5
7	8	7	6	7	8	10	14	10	9	6	5	9
8	8	10	6	12	6	7	13	9	11	6	9	5
9	3	5	11	13	6	11	10	16	6	6	6	7
10	9	6	7	7	13	13	8	9	8	10	7	3
11	3	8	5	7	6	10	14	12	8	7	9	12
12	4	6	6	4	11	7	14	12	8	8	7	13

Figure 5.7. As in Fig. 5.6 but for SOM nodes in the NCEP/NCAR reanalysis dataset. Same as Fig. 3.1 in Chapter 3.

# LIM 10-Day Composite Transition from Node 11 to 12
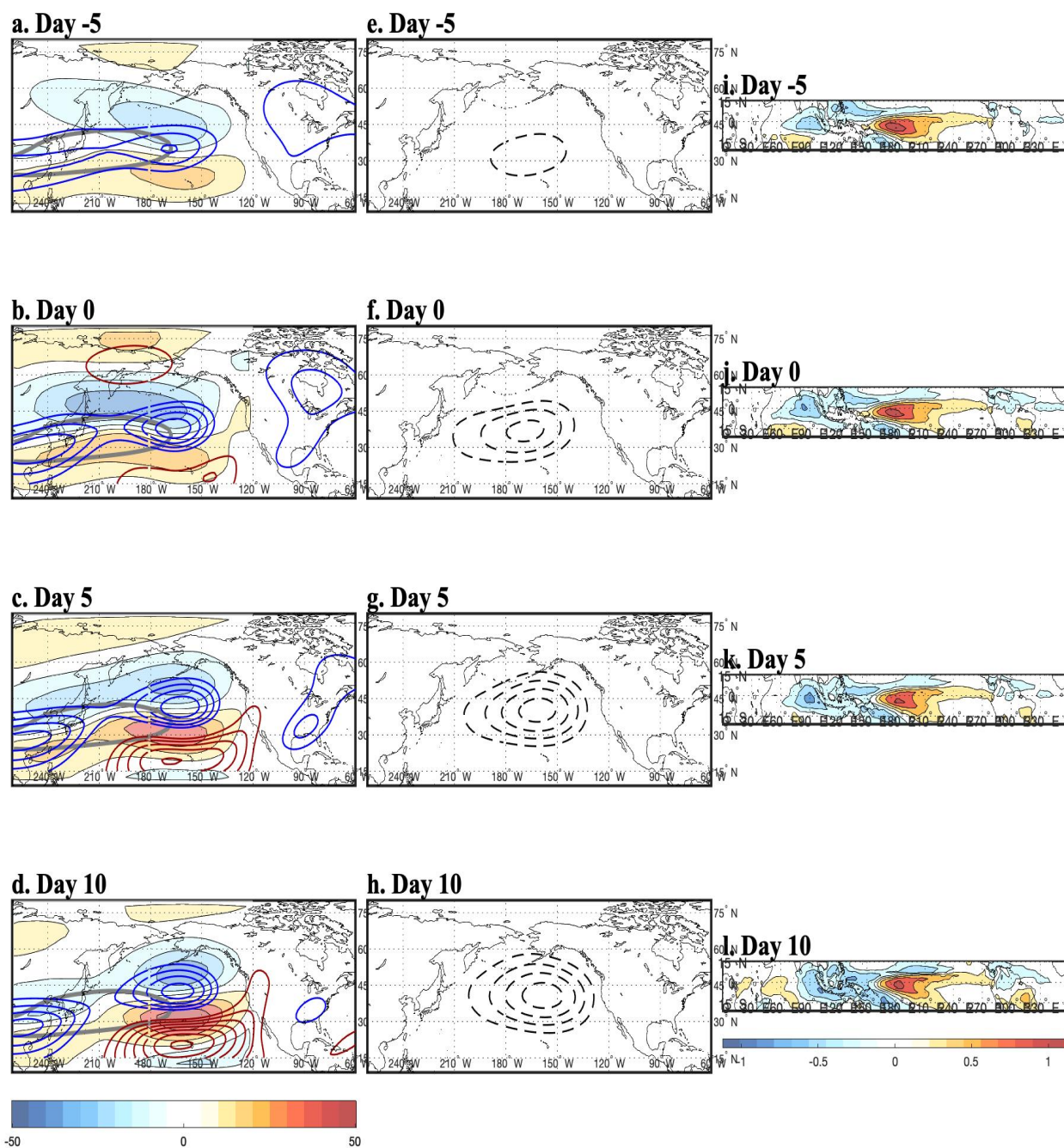
Figure 5.8: LIM composite large-scale features of SOM node 11 to node 12 10-day transition events (61 composited days) at lags -5, 0, 5, and 10 in which lag 0 is the start of the transition from node 11 and lag 10 is the end of the transition, characterized by node 12. **LEFT:** positive (negative) 200 hPa stream function ($x10^6 m^2 s^{-1}$) anomalies in red (blue) contoured every $2x10^6 m^2 s^{-1}$ starting at 4 (-4) and 250 hPa zonal wind anomalies (ms^{-1}) in red/yellow (blue/purple). Thick gray contour is the 40 ms^{-1}NDJFM mean isotach. **MIDDLE:** positive (negative) 850 hPa stream function anomalies ($x10^6 m^2 s^{-1}$) in solid (dashed) black lines contoured every $4\ x10^6 m^2 s^{-1}$ starting at 4 (-4). **RIGHT:** positive (negative) vertically integrated Q1 anomalies (K/day) in shaded contours.
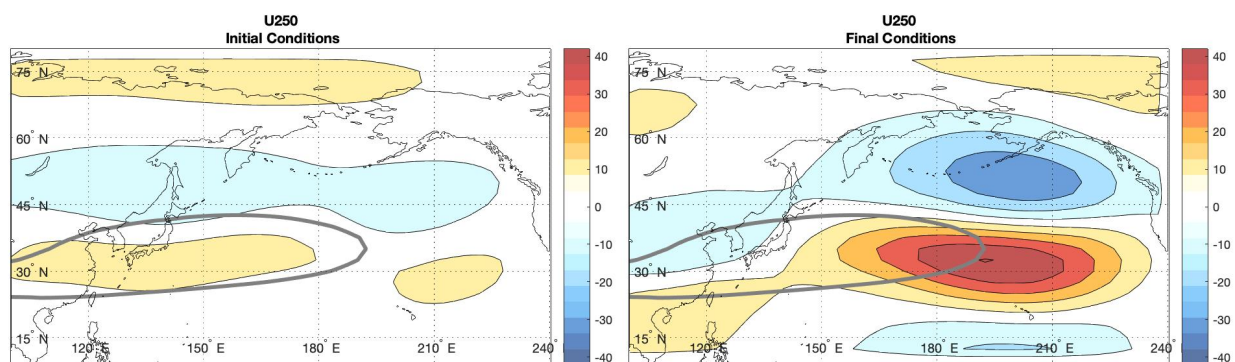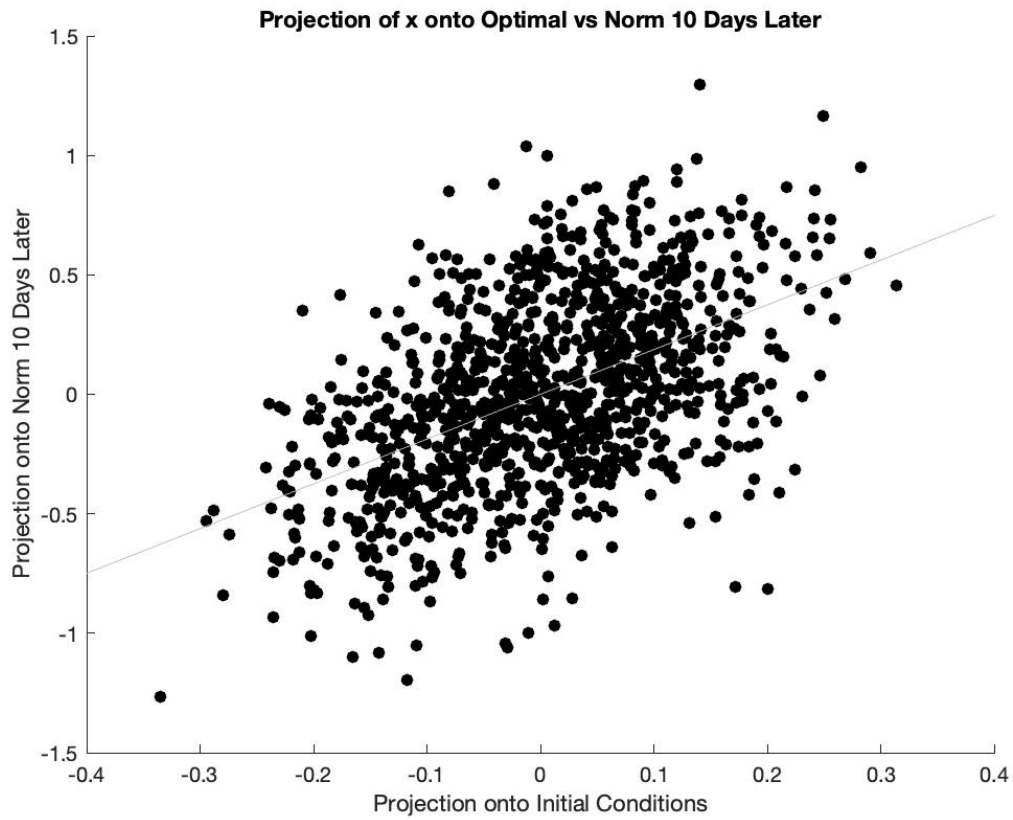
Figure 5.9: LEFT: optimal initial structure for growth towards a node 12 jet extension and **RIGHT:** final growth structure into which the optimal initial structure grows towards over 10 days for 250 hPa zonal wind anomalies in shaded contours every 10 ms^{-1}.
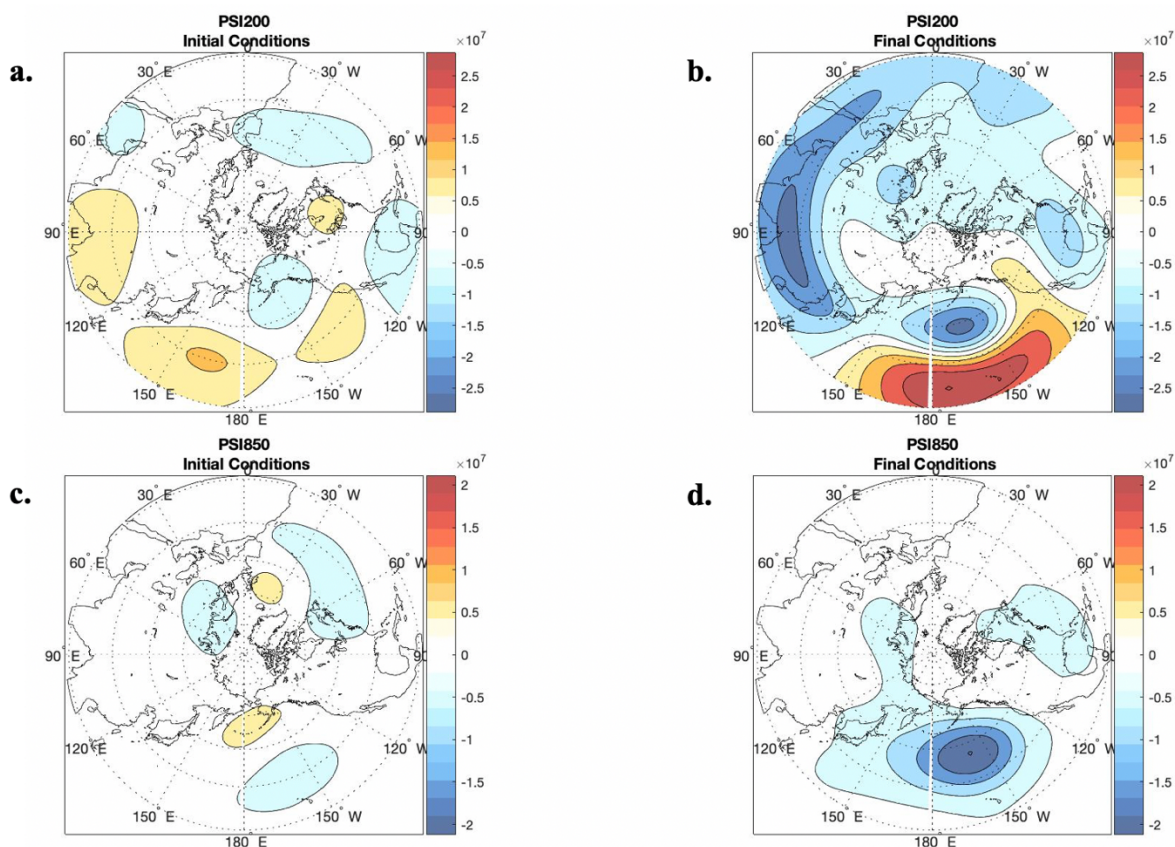
Figure 5.10: LEFT: optimal initial structure for growth towards a node 12 jet extension and **RIGHT:** final growth structure into which the optimal initial structure grows towards over 10 days for (top) 200 hPa streamfunction ($m^2 s^{-1}$) and (bottom) 850 hPa streamfunction ($m^2 s^{-1}$).
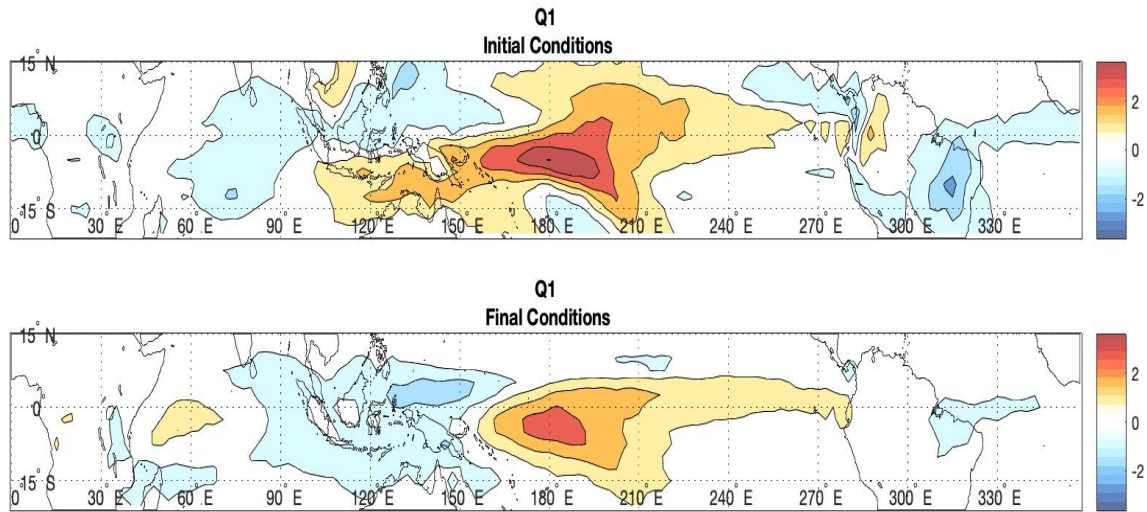
Figure 5.11: TOP: optimal initial structure for growth towards a node 12 jet extension and **BOTTOM:** final growth structure into which the optimal initial structure grows towards over 10 days for vertically integrated Q1 (K/day).
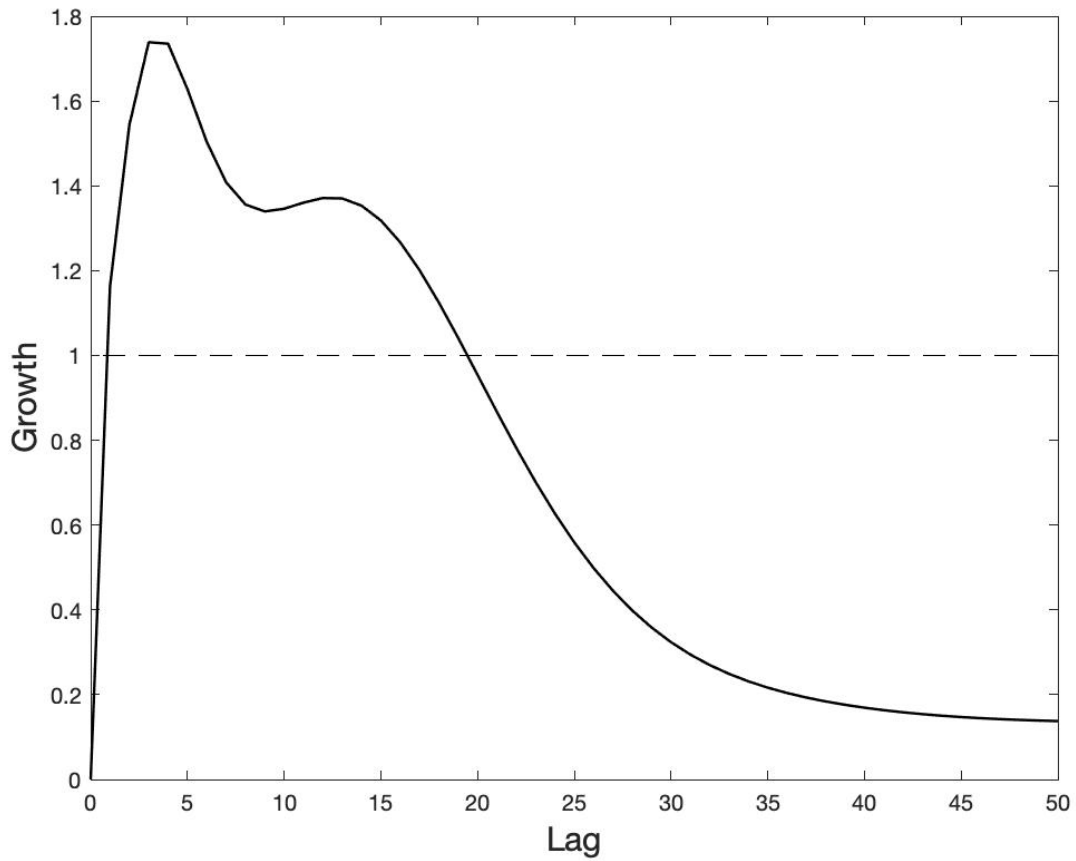
Figure 5.12: Growth of the system for the leading eigenvector, $\mathbf{p}_1$, under a SOM 12 norm as a function of lag in days. The black dashed denotes the expected decay of the SOM 12 pattern.

Figure 5.13: Projection of LIM state vector onto optimal initial conditions for growth towards a "SOM" node 12 vs the projection of the LIM state vector onto the "SOM" 12 norm 10 days later. The gray line is a least squares regression line with a slope of 0.51.
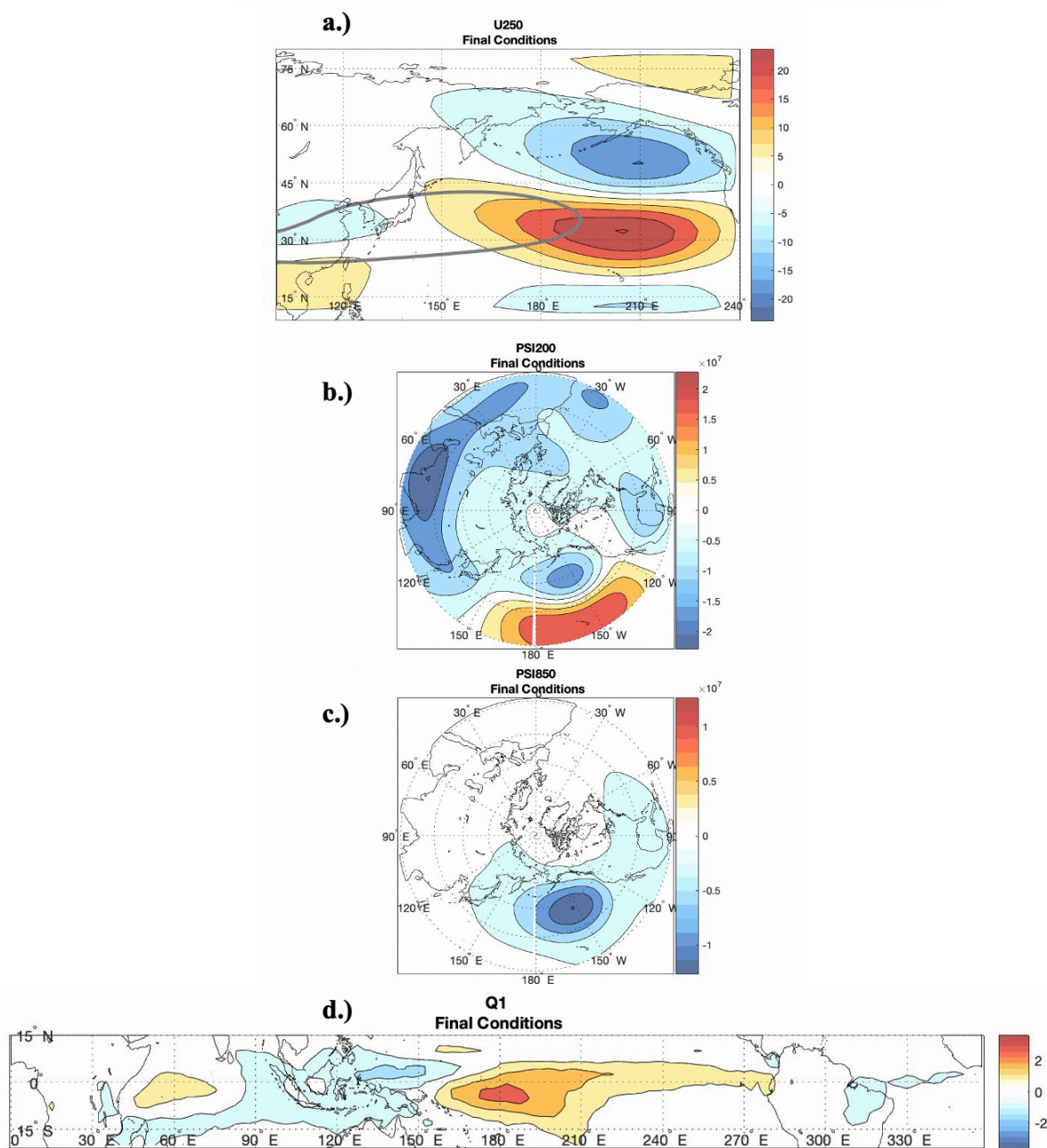
Figure 5.14: Final growth structure into which the optimal initial structure grows towards over 10 days by initializing with only the tropical OLR component of the optimal initial structure for (a) 250 hPa zonal wind in ms^{-1} (b) 200 hPa streamfunction in $m^2 s^{-1}$ (c) 850 hPa streamfunction in $m^2 s^{-1}$ and (d) Q1 in K/day.

Final Evolved Conditions: Initialized with ψ_{200}, ψ_{850}, & u_{250}
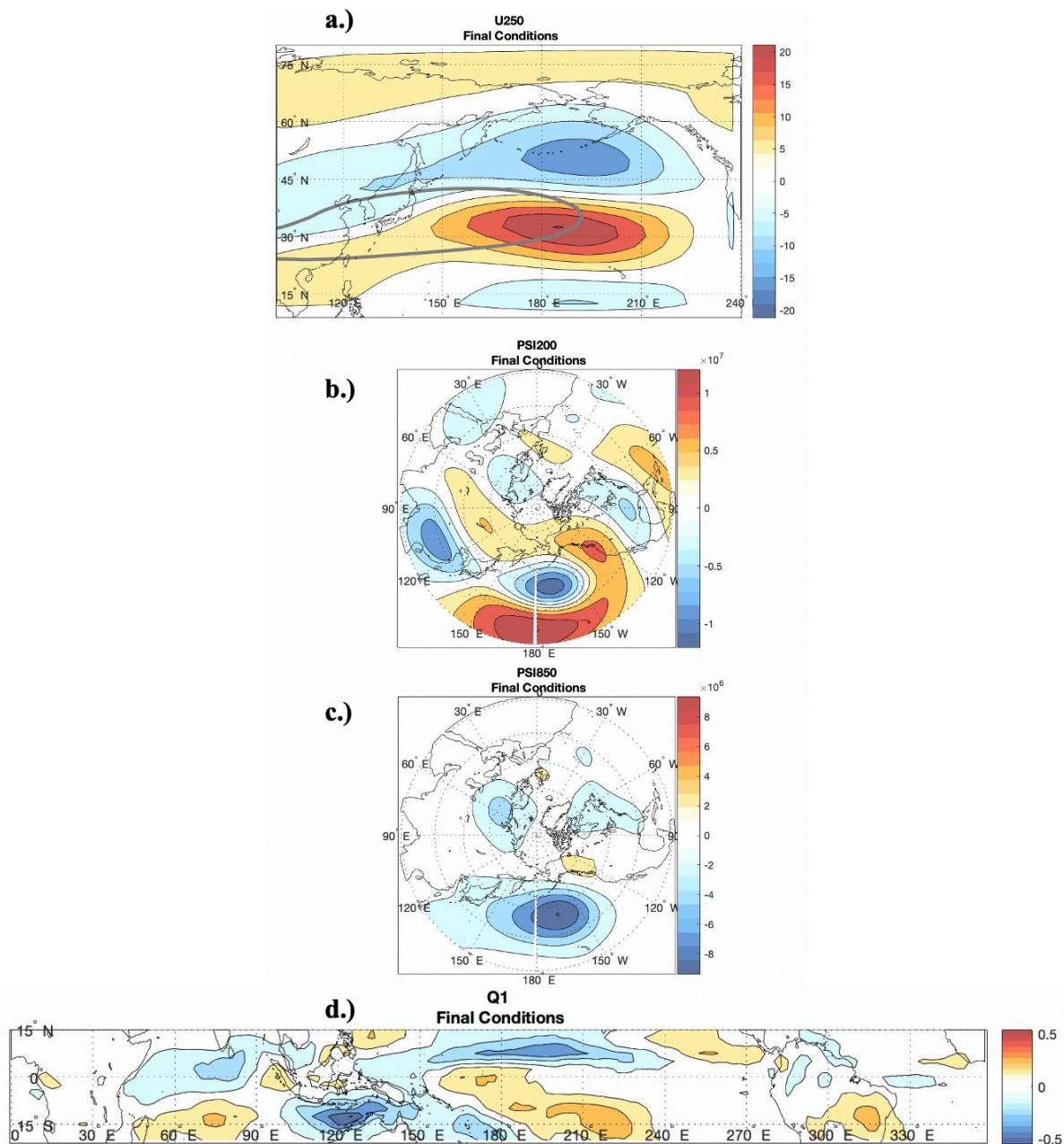
Figure 5.15: As in Fig. 5.12 but by initializing with only the 200 hPa and 850 hPa streamfunction and 250 hPa zonal wind component of the optimal initial structure.

Final Evolved Conditions: Initialized with Modified **L**
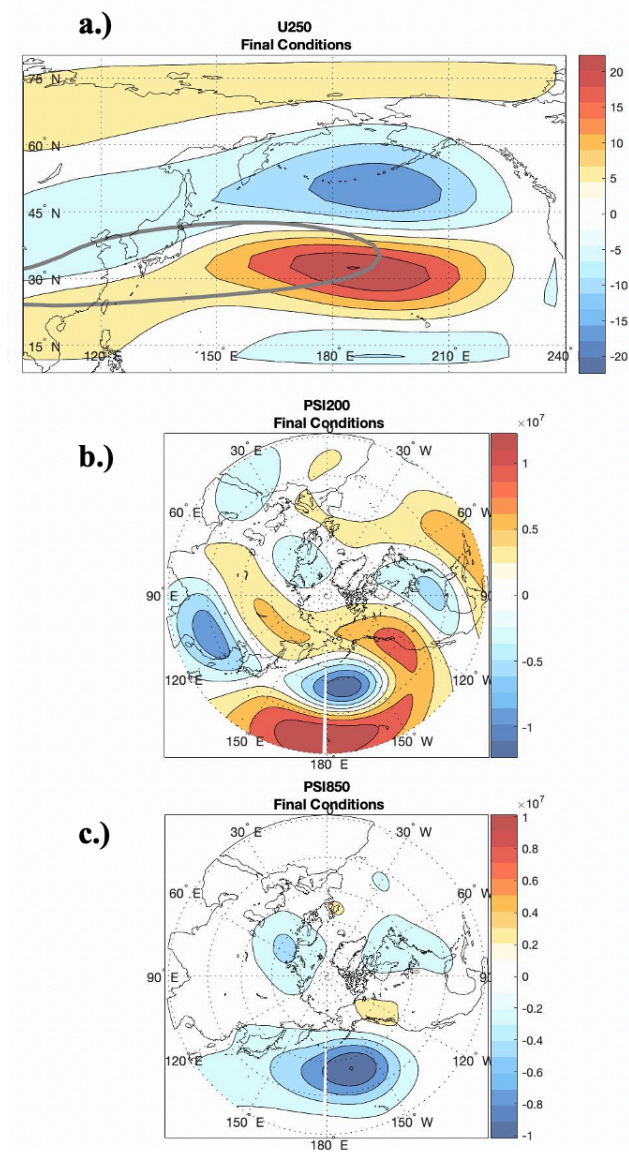
Figure 5.16: As in Fig. 5.15 but by setting the Q1 off-diagonal elements of **L** to zero.

CHAPTER 6: CONCLUSIONS

The deficiency in predictability at subseasonal-to-seasonal timescales relative to that at conventional weather prediction timescales is significant. Intraseasonal variability of the tropopause-level jet streams evolves within such time scales and often leads to extreme weather events with substantial societal impact. As these jets are an important feature at the interface of the large-scale general circulation and the life cycle of individual weather systems, there is strong incentive to more comprehensively understand their variability. Over the last decade, much of the understanding of wintertime Pacific jet variability has proceeded from EOF analysis. EOF analysis identifies two leading modes of variability: a zonal extension or retraction and a meridional deflection of the jet exit region (e.g. Athanasiadis et al. 2010; Jaffe et al. 2011; Griffin and Martin 2017; Breeden and Martin 2018; Winters et al. 2019a, 2019b). These leading modes, as well as transitions between them, have been shown to influence the synoptic scale circulation, downstream temperature extremes, and medium range forecast skill. Despite this, transitions within the north Pacific jet are still poorly understood. Therefore, the work in this thesis was motivated by three broad research questions:

- ***RQ1)*** *Are there preferred transitions within the wintertime Pacific jet? If so, what are they?*

- ***RQ2)*** *What are the characteristic evolution, synoptic-scale structure, and downstream impacts associated with the preferred transitions?*

- ***RQ3)*** *How predictable are these transitions? What is the role and relative importance of tropical heating and the extratropical circulation on these transitions? What is the role of the MJO in these evolutions?*

Investigation of ***RQ1*** proceeded from application of a novel self-organizing maps (SOM) analysis to characterize wintertime Pacific jet variability. Utilizing 250-hPa zonal winds from

NCEP/NCAR reanalysis over 71 extended cold seasons (NDJFM), 12 archetypical jet states were identified with SOM analysis. Although previous research on jet variability has relied heavily on EOF analysis, the leading EOFs explain only ~30% of the total variance, and each mode is linearly independent from the other. The use of SOMs provides a more physical, feature-based assessment of the nature of jet stream variability and offers a remedy for the lack of variance explained by EOF analysis alone.

The 12 SOM jet states described in Chapter 2 are characterized by anomaly patterns resembling the known EOF leading modes of Pacific jet variability, combinations between the leading modes, as well as newly identified anomaly patterns. Retractions of the jet are characterized by nodes 1, 5, and 9, whereas various latitudinal extensions are characterized by nodes 4, 8, and 12. Furthermore, poleward deflections of the jet exit region are evident in nodes along the top edge of the SOM grid (nodes 1-4), whereas equatorward deflections characterize nodes along the bottom edge (nodes 9-12). Although more than one SOM node illustrates retractions/extensions and equatorward deflections/poleward deflections, seemingly subtle differences in these anomalies are tied to distinct differences in the large-scale circulation and downstream low-level temperature anomalies (Ch. 2, Figures 2.4 & 2.5).

Examination of intraseasonal and interannual variability of the 12 SOM nodes described in Chapter 2 revealed that there is minimal intraseasonal variability in frequency of occurrence (FOC) of the 12 SOM nodes between November-March; however, more substantial variability in FOC exists at *interannual* timescales. This variability is evidenced to be, in part, tied to teleconnections like the PNA, AO, ENSO, and the MJO. These teleconnection patterns are more strongly tied to some nodes than others, further demonstrating the importance of expanding the existing 4-pattern (EOF 1 $^{\pm}$, EOF 2 $^{\pm}$) representation of wintertime Pacific jet variability that has, thus far, been the

standard. For example, extended node 12, with positive anomalies further equatorward than extensions depicted by nodes 4 and 8, exhibits a higher correlation to ENSO and larger FOC changes following strong MJO events. Node 8, on the other hand, exhibits the most dramatic changes in FOC during PNA events, while its FOC was less impacted by ENSO events. Addressing **RQ3** (the role of the MJO in Pacific jet evolutions), anomalous SOM node FOC following strong MJO events were analyzed. The FOC for node 4, which features an extension further poleward than nodes 8 and 12, exhibited the smallest changes in FOC following strong MJO events in addition to ENSO events. Moreover, results from Chapter 2 demonstrated that SOM node variability during strong MJO events is strongly influenced by ENSO phase. For example, during strong MJO events characterized by La Niña conditions, SOM node 1 exhibited significant changes in FOC. However, during El Niño or ENSO neutral conditions, early phases of the MJO coincided or preceded FOC increases in retracted node 9. While node 5 also features a retraction, it was not as strongly influenced by the MJO as the retraction denoted by node 9. Overall, the impact of the MJO on the Pacific jet evolution (**RQ3)** can be summarized in the following three categories:

- Strong MJO events during ENSO *neutral* conditions (Fig. 2.11)
    - Early phases of the MJO lead to higher likelihoods for a retracted jet characterized by nodes 9 and 5, and lower likelihoods of extended nodes 8 and 12. The middle phases of the MJO lead to an increase in FOC of equatorward deflected node 11 and a decrease in FOC of retracted nodes 5 and 9. MJO phase 5 is a precursor to node 12 jet extensions, for which a doubling of FOC characterizes MJO phases 5-7.
- Strong MJO events during ENSO *positive* conditions (Fig. 2.12)

- MJO phase 1 is a precursor to retracted node 9. However, from phases 2-3, the MJO is not as discriminative for SOM node regimes. By MJO phase 4, with enhanced convection migrating into the west Pacific, retracted nodes 1, 5 and 9 become less likely, while nodes 8 and 12 are more likely to occur 7-16 days later. Between MJO phases 5 and 8, constructive interference between the MJO and ENSO leads to a 200-300% increase in node 12 FOC. Nodes 1, 2, 5, and 9 are less likely to occur during the later phases of the MJO.

- Strong MJO events during ENSO *negative* conditions (Fig. 2.12)

  - Retracted and poleward deflected node 1 is much more likely to occur during early MJO phases with La Niña conditions, while nodes 7, 8, 10 and 11 are much less likely to occur. MJO phases 3 and 4, however, are precursors to poleward deflected node 2, with anomalous frequencies exceeding 200% during MJO phases 3-5. Extended node 12 and equatorward deflected node 11 exhibit strong FOC reductions during middle MJO phases, whereas retracted and/or equatorward deflected nodes 9 and 10 exhibit substantial reduced frequencies during MJO phases 5-8. Later MJO phases during La Niña are not dominated by any particular SOM node.

The changes in FOC following MJO events highlight the importance of not only stratifying by ENSO phase, but also of utilizing a more detailed analysis of the subtle differences in jet stream archetypes when characterizing responses to teleconnection patterns. The merit in a more refined representation of wintertime north Pacific jet archetypes is further established in Chapter 3, wherein transition probabilities between the 12 SOM nodes are quantified through probability tables at 5, 10, 15, and 20 days. On shorter 5-day timescales, all of the nodes were found to have

high likelihoods of persistence, with many nodes exhibiting preferred transitions into nodes of similar anomaly patterns (Fig. 3.1a). By 10-days, persistence is still likely for every node except weaker anomaly states 6 and 7, as well as nodes 3 and 5. Preferred transitions are evident between equatorward deflected states 9-11, in which a counterclockwise tendency through the SOM space illustrates transitions from a retracted jet with an equatorward anomaly to a more canonical equatorward deflection. By longer 15-day and 20-day timescales, only extended node 12 is likely to persist, and very few preferred transitions exist. Of the preferred transitions, node 11 is likely to transition into 12, and poleward deflected nodes 1-3 develop preferred transitions into other poleward deflected nodes. By 20-days, however, there is a preferred transition from a retraction characterized by node 9 into an extension characterized by node 8. No such preferred transitions are evident from extended states, which implies an asymmetry in transitions between extensions and retractions.

The same transition probability tables computed over a shorter DJF cold season reveal similar preferred and unlikely transitions, especially on short to medium range timescales. The transition from a retraction to extension, however, becomes a statistically significant likely transition at 15 days instead of 20 days, and the asymmetry in transitions between a retracted and an extended node, observed in NDJFM probability tables, is still apparent in DJF probability tables. Overall, analyses motivated by *RQ1* reveals that the likely transitions at medium range timescales occur from an equatorward deflected node 11 into a more extended node 12 (20% during NDJFM, 19% during DJF), from node 12 into a slight jet enhanced node 7 (16% during NDJFM and DJF), and from node 10 into a stronger retraction characterized by node 9 (16% during NDJFM, 19% during DJF). At timescales beyond two weeks, an extension (node 8) from a retracted jet (node 9) becomes likely. This transition between nearly opposite anomaly patterns

occurs on shorter 15-day timescales over DJF compared to the 20-day timescales over the extended NDJFM cold season.

In Chapter 4, **_RQ2_** is resolved through composite analyses of the synoptic-scale environments associated with the preferred 10-day and 15-day Pacific jet transitions. The 10-day transition from an equatorward deflected node 11 into extended node 12 was preceded by an upper-level cyclonic anomaly on the cyclonic shear side of the jet and a weak anticyclonic anomaly further poleward (Fig. 4.1 a). Over the transition period, an upper-level anticyclonic anomaly strengthens south of the jet and progresses northeastward, subsequently extending and deflecting the jet exit region ~5° poleward (Fig. 4.1). Composite OLR anomalies depict a region of negative anomalies over the tropical west Pacific on Day -5 and Day 0, indicative of enhanced convection. This area of enhanced convection resembles the OLR anomalies leading to positive PNA events in Franzke et al. (2011), in which enhanced convection over the west Pacific excited a positive PNA teleconnection pattern. Moreover, the the preferred transition from node 11 to node 12 is likely influenced by this enhanced convection over tropical west Pacific and depicts the onset of a positive PNA teleconnection pattern.

The composite structure depicting the 10-day transition from node 12 to node 7 (Fig. 4.2) depicts an eastward progression of OLR anomalies from Day -5 to Day 10 that resembles OLR anomalies associated with a propagating MJO event (Madden and Julian 1972; Zhang 2005). Towards the beginning of the transition, when the jet is extended (node 12, Day -5 & Day 0), enhanced convection is observed over the tropical west Pacific with suppressed convection over the eastern Indian Ocean, consistent with later MJO phases. However, by the end of the transition into node 7, a small area of enhanced convection is observed over the Indian Ocean, and areas of suppressed convection characterize the tropical Pacific basin, indicative of early MJO phases. The

composite 10-day evolution of the preferred transition from node 10 to a retracted node 9 depicts a retrogression and strengthening of an upper-level anticyclonic anomaly over the north Pacific and strengthening of a cyclonic anomaly to the south (Fig. 4.3). OLR anomalies on Day 10 resemble composite Day 10 jet retraction OLR anomalies from Jaffe et al. (2011), with enhanced convection over the subtropical central Pacific and suppressed convection further south.

A composite analysis was also performed for the 15-day preferred DJF transition from retracted node 9 into an extended node 8 (Figure 4.4). The transition from a retraction to an extension is associated with a retrogression of an upper-level anticyclonic anomaly and an eastward progression and weakening of a cyclonic anomaly to the south. Over the 15 days, the anticyclonic anomaly progresses southward through the jet such that by Day 15, it is located on the anticyclonic shear side of the jet stream. The cyclonic anomaly retrogresses from over the east Pacific on Day 5 to north of the jet exit region on Day 15. Near the surface, a seesawing occurs in 850 hPa stream function anomalies, with a cyclonic anomaly on Day 0 with warm 850 temperature anomalies on its eastern flank to an anticyclonic anomaly on Day 15 with weak warm temperature anomalies over northwest Canada. The composite structure of OLR illustrates unorganized convection from Day -5 to Day 10, with areas of suppressed convection over the eastern Pacific and Indian Ocean by Day 15.

To characterize the predictability of the preferred transitions identified in Chapter 3 and resolve *RQ3*, a linear inverse model (LIM) is constructed with 200 hPa and 850 hPa stream function, tropical Q1, and 250 hPa zonal winds. In a LIM, the low-frequency flow is modeled as a linear system driven by stochastic white noise (e.g. Pendland and Sardeshmukh 1993; Winkler et al. 2001). The assumptions of stable, linear dynamics are testable, in which the assumptions for the LIM constructed in Chapter 5 were deemed valid after testing. Integrating the LIM forward in

a two-step process to preserve the covariance and noise statistics of the dynamical system, a sample trajectory of 10,000 Pacific jet patterns was generated. These patterns were assigned a corresponding SOM node through a minimization of RMSE error between the forward integration model output and the 12 SOM patterns. Transition probability tables calculated from the LIM demonstrated that at 5 days, the preferred and unlikely transitions identified in the reanalysis 5-day probability tables are well reproduced by the LIM (Fig. 5.6a). However, by 10-days, most of the overlap between the reanalysis table and the LIM occurs for the likely persistence of nodes 1, 2, 4, 8, 9, 10, 11, and 12 (Fig. 5.6b). The preferred transitions from node 9 to 10 and from node 11 to 12 were evident in the LIM, with consistent unlikely transitions into node 12 from nodes 2, 5, and 6 as well as from node 12 to 1 and 5. Beyond two weeks, the preferred persistence of extended node 12 remained the only consistent statistically significant probability between the reanalysis and the LIM. Additionally, the preferred transition from retracted node 9 to extended node 8 at longer 2-3 week timescales was not identified as a significant transition in the LIM.

In general, the likely persistence of the north Pacific jet can be reproduced in a linear framework driven by stochastic white noise; however, preferred transitions observed between 10 and 20-days in reanalysis are not well captured by the LIM. This could indicate that either unparameterizable nonlinear processes play a larger role in driving the transitions at longer 2-3-week timescales, or that additional variables (or levels) are needed in the construction of the LIM. For example, the inclusion of stream function at 10 hPa and a surface variable like mean-sea level pressure to represent surface and vertically deep stratospheric variability (as used in the LIM constructed in Albers and Newman, 2019) might provide necessary detail in the prediction of Pacific jet transitions. Nevertheless, likely and unlikely transitions involving node 12 exhibited the most consistency with reanalysis at medium to extended timescales, and composite analysis of

transition from node 11 to 12 in the LIM (Fig. 5.8) depicts a similar evolution to the 10-day composite transition in reanalysis data (Fig. 4.1). The transition in the LIM, however, seemed to be associated with El Niño-like conditions in the Pacific, whereas the transition in reanalysis was evidenced to be tied to enhanced convection over the Indian Ocean exciting a Rossby wave train and subsequent PNA pattern.

The LIM was also utilized to identify optimal extratropical and tropical structures that grow towards a prescribed jet-stream pattern. As the persistence and transition behavior of node 12 was best reproduced by the forward integration LIM, growth is optimized towards node 12 to further diagnose precursors at medium range timescales and the relative roles of tropical versus extratropical processes in transitioning into an extended jet (**RQ3**). Optimal conditions that grow towards an extended node 12 over 10 days are characterized by a node 7-like jet pattern with positive anomalies along the jet core and a dipole in stream function anomalies over the east Pacific with a diffuse upper-level ridge over the western Pacific (Fig. 5.9 & 5.10). In the tropics, enhanced convection stretches across the tropical Pacific, with a maximum centered near the dateline. The optimal initial and final Q1 anomalies resemble combined MJO and El Niño conditions. Modification of the LIM to isolate tropical versus extratropical contributions to the growth revealed that both were necessary to grow towards a strong extension, with the extension being only half as strong when the LIM was initialized with only extratropical or only tropical initial conditions.

In this thesis, a new method is applied to characterize wintertime north Pacific jet variability that expands on the previous EOF-identified leading modes of variability. The differences in synoptic-scale environments, associated teleconnections, and preferred and unlikely transitions between the 12 SOM nodes suggests that important jet structures with distinct

underlying processes and teleconnections have been unknowingly merged in obfuscation in previous analyses. As discussed in Chapter 4, evidence for the blending of important structures can be found in considering analyses from Winters et al. (2019b), wherein key differences in the synoptic-scale structure were observed between best and worst medium-range forecasts within each EOF-identified regime. Furthermore, the different structures associated with the best and worst forecasts within each regime bore resemblance to the SOM nodes in this analysis. Future work applying the SOM-based analysis presented in this thesis to assessing medium range forecast skill may add considerable value to medium range forecasts.

Additional future work includes a case study analysis on the influence of the MJO on transitions within the Pacific jet. Following Michel and Rivière (2011), a SOM node regime index can be utilized to project each day within an MJO event onto the zonal wind anomaly pattern of each SOM node. The projection with a large index value is identified as the prevailing SOM node regime. The index $I_S(t)$, is defined as:

$$I_S(t) = \frac{P_S(t) - \bar{P}_S}{\sqrt{\frac{1}{NT}\Sigma_{t=1}^{NT}[P_S(t) - \bar{P}_S]^2}},$$ (6.1)

where t is a day within the MJO event, NT is the number of cold season days, $\bar{P}_S$ is the climatological mean of the projection, and $P_{SR}(t)$ is the projection of the zonal wind anomaly, u_{250}', onto the zonal wind anomaly of the SOM node, u_{250S}'. The benefit of using this index to measure each day's projection onto the 12 SOM patterns is that it will classify periods of growth towards a particular SOM node, facilitating a clearer depiction of transitions between the SOM nodes throughout the MJO event as well as periods in which none of the 12 SOM node patterns are well established. This type of case study analysis can be extended over any time period to examine various precursors and teleconnections that drive and/or impact Pacific jet transitions.

Overall, the work presented in this thesis, as well as future applications of this work, will further the understanding of Pacific jet variability. The combination of SOM, LIM, composite, and case study analyses provides a more detailed look at the wintertime Pacific jet, the teleconnections that influence transitions within it, and the synoptic-scale circulations and downstream impacts associated with such transitions. Further development based on the insights arising from this work are likely to enhance forecasts in both the medium-range and sub-seasonal to seasonal timescales.

REFERENCES

1. Albers, J. R., and M. Newman, 2019: A Priori Identification of Skillful Extratropical Subseasonal forecasts. *Geophys. Res. Lett*., **46**, 12 527–12 536, https://doi.org/10.1029/2019GL085270.

2. Alexander, M. A., L. Matrosova, C. Penland, J. D. Scott, and P. Chang, 2008: Forecasting Pacific SSTs: Linear inverse model predictions of the PDO. *J. Climate*, **21**, 385–402, https://doi.org/10.1175/2007JCLI1849.1.

3. Anderson, J. R., and R. D. Rosen, 1983: The Latitude-Height Structure of 40–50 Day Variations in Atmospheric Angular Momentum, *Journal of Atmospheric Sciences*, **40**(6), 1584-1591, https://doi.org/10.1175/1520-0469(1983)040<1584:TLHSOD>2.0.CO;2.

4. Athanasiadis, P. J., J. M. Wallace, and J. J. Wettstein, 2010: Patterns of wintertime jet stream variability and their relation to the storm tracks. *Journal of the Atmospheric Sciences*, **67**, 1361–1381, https://doi.org/10.1175/2009JAS3270.1.

5. Barnston, A. G., and R. E. Livezey, 1987: Classification, seasonality, and persistence of low-frequency atmospheric circulation patterns. *Monthly Weather Review*, **115**, 1083–1126, https://doi.org/10.1175/1520-0493(1987)115<1083:CSAPOL>2.0.CO;2.

6. Breeden, M. and J. E. Martin, 2018: Analysis of the initiation of an extreme North Pacific jet retraction using piecewise tendency diagnosis. *Quarterly Journal of the Royal Meteorological Society*, **144(715)**, 1895–1913, https://doi.org/10.1002/qj.3388.

7. Breeden, M., and J. E. Martin, 2019: Evidence for nonlinear processes in fostering a North Pacific jet retraction. *Quarterly Journal of the Royal Meteorological Society*, **145**, 1559–1570, https://doi.org/10.1002/qj.3512.

8. Breeden, M.L., B.T. Hoover, M. Newman, and D.J. Vimont, 2020: Optimal North Pacific Blocking Precursors and Their Deterministic Subseasonal Evolution during Boreal Winter. *Mon. Wea. Rev.,* **148**, 739 - 761, https://doi.org/10.1175/MWR-D-19-0273.1.

9. Cassano, E. N., A. H. Lynch, J. J. Cassano, and M. R. Koslow, 2006: Classification of synoptic patterns in the western Arctic associated with extreme events at Barrow, Alaska, USA. *Climate Research*, **30**, 83–97, https://doi.org/10.3354/cr030083.

10. Cassou, C, 2008: Intraseasonal interaction between the Madden–Julian oscillation and the North Atlantic oscillation. *Nature,* **455**(7212):523–527, https://doi.org/10.1038/nature07286.

11. Chu, P. A. J. Nash, and F. Porter, 1993: Diagnostic studies of two contrasting rainfall episodes in Hawaii: Dry 1981 and wet 1982. *Journal of Climate*, **6**, 1457–1462, https://doi.org/10.1175/1520-0442(1993)006<1457:DSOTCR>2.0.CO;2.

12. Cohen, S. J., 1983: Classification of 500 mb height anomalies using obliquely rotated principal components. *Journal of Applied Meteorology*, **22(12)**, 1975-1988, https://doi.org/10.1175/1520-0450(1983)022<1975:COMHAU>2.0.CO;2.

13. Dee, D. P., and Coauthors, 2011: The ERA-Interim reanalysis: Configuration and performance of the data assimilation system. *Quarterly Journal of the Royal Meteorological Society.*, **137**, 553-597, https://doi.org/10.1002/qj.828.

14. Delcambre, S., D. Lorenz, , D. Vimont, , and J. Martin, 2013: Diagnosing Northern Hemisphere jet portrayal in 17 CMIP3 global climate models: Twentieth-century intermodel variability. *Journal of Climate*, **26**, 4910–4929, https://doi.org/10.1175/JCLI-D-12-00337.1.

15. Franzke, C., and S. B. Feldstein, 2005: The continuum and dynamics of Northern Hemisphere teleconnection patterns. *Journal of the Atmospheric Sciences*, **62**, 3250–3267, https://doi.org/10.1175/JAS3536.1.

16. Franzke, C., T. Woollings, and O. Martius, 2011: Persistent circulation regimes and preferred regime transitions in the North Atlantic. *Journal of the Atmospheric Sciences*, **68**, 2809 – 2825, https://doi.org/10.1175/JAS-D-11-046.1.

17. Gervais, M., E. Atallah, J. R. Gyakum, and L. Bruno Tremblay, 2016: Arctic air masses in a warming world. *Journal of Climate*, **29 (7)**, 2359–2373, https://doi.org/10.1175/JCLI-D-15-0499.1.

18. Gill, A. E., 1980: Some simple solutions for heat-induced tropical circulation. *Quart. J. Roy. Meteor. Soc.*, **106**, 447–462, https://doi.org/10.1002/qj.49710644905.

19. Griffin, K. S., and J. E. Martin, 2017: Synoptic features associated with temporally coherent modes of variability of the North Pacific jet stream. *Journal of Climate*, **30**, 39–54, https://doi.org/10.1175/JCLI-D-15-0833.1.

20. Gu, Q., and M. Gervais, 2021: Exploring North Atlantic and North Pacific Decadal climate prediction using self-organizing maps. *Journal of Climate*, **34(1)**, 123–141. https://doi.org/10.1175/JCLI-D-20-0017.1.

21. Hannachi, A., 2004: A primer for EOF analysis of climate data. University of Reading, 33 pp.

22. Henderson, S. A., Vimont, D. J., & Newman, M., 2020: The Critical Role of Non-Normality in Partitioning Tropical and Extratropical Contributions to PNA Growth, *Journal of Climate*, *33*(14), 6273-6295, https://journals.ametsoc.org/view/journals/clim/33/14/JCLI-D-19-0555.1.xml.

23. Hewitson, B. C., and R. G. Crane, 2002: Self-organizing maps: Applications to synoptic climatology. *Climate Research*, **22 (1)**, 13–26, https://doi.org/10.3354/cr022013.

24. Hope, P. K., W. Drosdowsky, and N. Nicholls, 2006: Shifts in synoptic systems influencing south west Western Australia. *Climate Dynamics*, **26**, 751–764, https://doi.org/10.1007/s00382-006-0115-y.

25. Hoskins, B. J., & Karoly, D. J., 1981: The Steady Linear Response of a Spherical Atmosphere to Thermal and Orographic Forcing, *Journal of Atmospheric Sciences*, *38*(6), 1179-1196, https://journals.ametsoc.org/view/journals/atsc/38/6/1520-0469_1981_038_1179_tslroa_2_0_co_2.xml.

26. Jaffe, S. C., J. E. Martin, D. J. Vimont, and D. J. Lorenz, 2011: A synoptic climatology of episodic, subseasonal retractions of the Pacific jet. *Journal of Climate*, **24**, 2846–2860, https://doi.org/10.1175/2010JCLI3995.1.

27. Jayawardena, I.M., Y. L. Chen, A.J. Nash, and K. Kodama, 2012: A comparison of three prolonged periods of heavy rainfall over the Hawaiian islands. *Journal of Applied Meteorology*, **51**, 722–744, https://doi.org/10.1175/JAMC-D-11-0133.1.

28. Johnson, N. C. and S. B. Feldstein, 2010: The continuum of North Pacific sea level pressure patterns: Intraseasonal, interannual, and interdecadal variability. *Journal of Climate*, **23**, 851-867, https://doi.org/10.1175/2009JCLI3099.1.

29. Kalnay, E., and Coauthors, 1996: The NCEP/NCAR 40-Year Reanalysis Project. *Bull. Amer. Meteor. Soc.*, **77**, 437–471, https://doi.org/10.1175/1520-0477(1996)077<0437:TNYRP>2.0.CO;2.

30. Kohonen, T., 1982: Self-organized formation of topologically correct feature maps. *Biological Cybernetics*, **43 (1)**, 59–69, https://doi.org/10.1007/BF00337288.

31. Kohonen, T., 1998: The self-organizing map. *Neurocomputing: An International Journal, 21*(1-3)*, 1–6, https://doi.org/10.1016/S0925-2312(98)00030-7.

32. Kohonen, T., M. R. Schroeder, and T. S. Huang, Eds., 2001: *Self-Organizing Maps*. 3rd ed., Springer-Verlag, Berlin, Heidelberg.

33. Kutzbach, J. E., 1967: Empirical eigenvectors of sea-level pressure, surface temperature and precipitation complexes over North America. *Journal of Applied Meteorology and Climatology*, **6(5)**, 791-802, https://doi.org/10.1175/1520-0450(1967)006<0791:EEOSLP>2.0.CO;2.

34. Lee, J.C.K., Lee, R.W., Woolnough, S.J. and L. J. Boxall*, 2020: The links between the Madden-Julian Oscillation and European weather regimes. *Theor Appl Climatol, *141,* 567–586, https://doi.org/10.1007/s00704-020-03223-2.

35. Liebmann, B., and C. A. Smith, 1996: Description of a complete (interpolated) outgoing longwave radiation dataset. *Bull. Amer. Meteor. Soc.,***77,** 1275–1277.

36. Liu, Y.,R. H. Weisberg, and C. N. Mooers, 2006: Performance evaluation of the self-organizing map for feature extraction. *Journal of Geophysical Research: Oceans*, **111 (C5)**, https://doi.org/10.1029/2005JC003117.

37. Livezey, R. E., and W. Y. Chen, 1983: Statistical field significance and its determination by Monte Carlo techniques. *Mon. Wea. Rev.*, **111**, 46–59, https://doi.org/10.1175/1520-0493(1983)111<0046:SFSAID>2.0.CO;2.

38. Lorenz, E. N., 1956: Empirical orthogonal functions and statistical weather prediction. Statistical Forecasting Project Report 1, Dept. of Meteor., MIT. 49pp.

39. Lynch A., O. Uotila, and J. J. Cassano, 2006: Changes in synoptic weather patterns in the polar regions in the 20th and 21st centuries, part 2: Antarctic, *International Journal of Climatology*, **26**(9), 1181–1199, https://doi.org/10.1002/joc.1305.

40. Madden, R. A., and P. R. Julian, 1971: Detection of a 40–50 day oscillation in the zonal wind in the tropical Pacific. *Journal of the Atmospheric Sciences*, **28**, 702–708, https://doi.org/10.1175/1520-0469(1971)028<0702:DOADOI>2.0.CO;2.

41. Madden, R. A., and P. R. Julian, 1972: Description of global-scale circulation cells in the tropics with a 40–50 day period. *Journal of the Atmospheric Sciences*, **29**, 1109–1123, https://doi.org/10.1175/1520-0469(1972)029<1109:DOGSCC>2.0.CO;2.

42. Matsuno, T., 1966: Quasi-geostrophic motion in the equatorial area. J. Meteor. Soc. Japan, **44**, 25–43.

43. Moore, R. W., Martius, O., and T. Spengler, 2010: The Modulation of the Subtropical and Extratropical Atmosphere in the Pacific Basin in Response to the Madden–Julian Oscillation, *Monthly Weather Review*, **138**(7), 2761-2779. https://doi.org/10.1175/2010MWR3194.1.

44. Newman, M., and et al., 2016: The Pacific decadal oscillation, revisited. *J. Climate*, **29**, 4399–4427, https://doi.org/10.1175/JCLI-D-15-0508.1.

45. Newman, M., and P. D. Sardeshmukh, 1998: The impact of the annual cycle on the North Pacific/North American response to remote low-frequency forcing. *Journal of the Atmospheric Sciences*, **55**, 1336– 1353, https://doi.org/10.1175/1520-0469(1998)055<1336:TIOTAC>2.0.CO;2.

46. Otkin, J. A., and J. E. Martin, 2004: The large-scale modulation of subtropical cyclogenesis in the central and eastern Pacific Ocean. *Monthly Weather Review*, **132**, 1813–1828, https://doi.org/10.1175/1520-0493(2004)132<1813:TLMOSC>2.0.CO;2.

47. Penland, C., 1989: Random forcing and forecasting using principal oscillation pattern analysis. *Mon. Wea. Rev.*, **117**, 2165–2185, https://doi.org/10.1175/1520-0493(1989)117<2165:RFAFUP>2.0.CO;2.

48. Penland, C., and L. Matrosova, 1994: A balance condition for stochastic numerical models with application to the El Niño–Southern Oscillation. *J. Climate*, **7**, 1352– 1372, https://doi.org/10.1175/1520-0442(1994)007<1352:ABCFSN>2.0.CO;2.

49. Penland, C., and P. D. Sardeshmukh, 1995: The optimal growth of tropical sea surface temperature anomalies. *J. Climate*, **8**, 1999–2024, https://doi.org/10.1175/1520-0442(1995)008<1999:TOGOTS>2.0.CO;2.

50. Raymond, D. J., 1992: Nonlinear Balance and Potential-Vorticity Thinking At Large Rossby Number. *Q. J. R. Meteorol. Soc.,* **118**, 987-1015, https://doi.org/10.1002/qj.49711850708.

51. Reiter, E., 1963: Jet-stream meteorology. University of Chicago Press.

52. Reiter, E., 1967: Jet streams; how do they affect our weather? Doubleday.

53. Reusch, D. B., R. B. Alley, and B. C. Hewitson, 2007: North Atlantic climate variability from a self-organizing map perspective. *Journal of Geophysical Research Atmospheres*, **112 (D2)**, https://doi.org/10.1029/2006JD007460.

54. Sammon, J. W., 1969: A nonlinear mapping for data structure analysis. *IEEE Transactions on Computers*, **18**, 401–409, https://doi.org/10.1109/T-C.1969.222678.

55. Schubert, S. D., and C.-K. Park, 1991: Low-frequency intraseasonal tropical–extratropical interactions. *Journal of the Atmospheric Sciences*, **48**, 629–650, https://doi.org/10.1175/1520-0469(1991)048<0629:LFITEI>2.0.CO;2.

56. Schuenemann, K., J. Cassano, and J. Finnis, 2009: Forcing of precipitation over Greenland: Synoptic climatology for 1961–99, *Journal of Hydrometeorology*, **10**, 60– 78, https://doi.org/10.1175/2008JHM1014.1.

57. Schuenemann, K. C., and J. J. Cassano, 2009: Changes in synoptic weather patterns and Greenland precipitation in the 20th and 21st centuries: 1. Evaluation of late 20th century simulations from IPCC models. *Journal of Geophysical Research,* **114**, D20113, https://doi.org/10.1029/2009JD011705.

58. Schuenemann, K. C., and J. J. Cassano, 2010: Changes in synoptic weather patterns and Greenland precipitation in the 20th and 21st centuries: 2. Analysis of 21st century atmospheric changes using self-organizing maps. *Journal of Geophysical Research,* **115**, D05108, https://doi.org/10.1029/2009JD011706.

59. Skific, N., J. A. Francis, and J. J. Cassano, 2009a: Attribution of projected changes in atmospheric moisture transport in the Arctic: A self-Organizing map perspective. *Journal of Climate*, **22(15)**, 4135–4153, https://doi.org/10.1175/2009JCLI2645.1.

60. Skific, N., J. A. Francis, and J. J. Cassano, 2009b: Attribution of seasonal and regional changes in Arctic moisture convergence. *Journal of Climate*, **22(19)**, 5115-5134, https://doi.org/10.1175/2009JCLI2829.1.

61. Smith, T. M., R. W. Reynolds, R. E. Livezey, and D. C. Stokes, 1996: Reconstruction of sea surface temperature using empirical orthogonal functions, *Journal of Climate,* **9**, 1403-1420, https://doi.org/10.1175/1520-0442(1996)009<1403:ROHSST>2.0.CO;2.

62. Stoelinga, M. T., 1996: A Potential Vorticity-Based Study of the Role of Diabatic Heating and Friction in a Numerically Simulated Baroclinic Cyclone, *Monthly Weather Review*, **124**(5), 849-874. https://doi.org/10.1175/1520-0493(1996)124<0849:APVBSO>2.0.CO;2.

63. Thorncroft C, Hoskins BJ, McIntyre ME. 1993. Two paradigms of baroclinic wave life cycle behaviour. *Quarterly Journal of the Royal Meteorological Society,* **119**, 17–55, https://doi.org/10.1002/qj.49711950903.

64. Trenberth, K. E., Branstator, G. W., Karoly, D., Kumar, A., Lau, N.-C., and C. Ropelewski, 1998: Progress during TOGA in understanding and modeling global teleconnections associated with tropical sea surface temperatures, *J. Geophys. Res.*, **103**(C7), 14291– 14324, https://doi.org/10.1029/97JC01444.

65. Vesanto, J., J. Himberg, E. Alhoniemi, and J. Parhankangas, 2000: SOM toolbox for Matlab 5. Helsinki University of Technology Tech. Rep. A57, 60 pp.

66. Vimont, D. J., M. A. Alexander, and M. Newman, 2014: Optimal growth of central and East Pacific ENSO events. *Geophys. Res. Lett.*, **41**, 4027–4034, https://doi.org/10.1002/2014GL059997.

67. Wallace, J. M., and D. S. Gutzler, 1981: Teleconnections in the geopotential height field during the Northern Hemisphere winter. *Monthly Weather Review,* **109**, 784–812, https://doi.org/10.1175/1520-0493(1981)109<0784:TITGHF>2.0.CO;2.

68. Wettstein, J. J., and J. M. Wallace, 2010: Observed patterns of month-to-month storm track variability and their relationship to the background flow. *Journal of the Atmospheric Sciences*, **67**, 1420–1437, https://doi.org/10.1175/2009JAS3194.1.

69. Wheeler, M. C., and H. H. Hendon, 2004: An all-season real-time multivariate MJO index: Development of an index for monitoring and prediction. *Mon. Wea. Rev.*, **132**, 1917–1932, https://doi.org/10.1175/1520-0493(2004)132<1917:AARMMI>2.0.CO;2.

70. Wilks, D. S., 2011: *Statistical Methods in the Atmospheric Sciences*, Vol. 100. Academic press, 648 pp.

71. Winkler, C. R., M. Newman, and P. D. Sardeshmukh, 2001: A linear model of wintertime low-frequency variability. Part I: Formulation and forecast skill. *J. Climate*, **14**, 4474–4494, https://doi.org/10.1175/1520-0442(2001)014<4474:ALMOWL>2.0.CO;2.

72. Winters, A. C., L. F. Bosart, and D. Keyser, 2019a: Antecedent North Pacific jet regimes conducive to the development of continental U.S. extreme temperature events during the cool season. *Weather Forecasting*, **34**, 393–414, https://doi.org/10.1175/WAF-D-18-0168.1.

73. Winters, A. C., D. Keyser, and L. F. Bosart, 2019b: The development of the North Pacific jet phase diagram as an objective tool to monitor the state and forecast skill of the upper-tropospheric flow pattern. *Weather Forecasting*, **34**, 199–219, https://doi.org/10.1175/WAF-D-18-0106.1.

74. Yanai, M., Esbensen, S.K., and Chu, J., 1973: Determination of bulk properties of tropical cloud clusters from large-scale heat and moisture budgets. *Journal of the Atmospheric Sciences,* **30,** 611-627, https://doi.org/10.1175/1520-0469(1973)030<0611:DOBPOT>2.0.CO;2.